University of Fort Hare
Together in Excellence

Petrographic and Petrophysical Characterization of Sandstone Reservoir Rocks for CO_2 Geological Storage in the Bredasdorp Basin, offshore South Africa.

A Thesis in Petroleum Geology

By

Siyamtanda Hoza

Submitted in fulfilment of the requirements for the degree of

M.Sc. (Masters) in the Department of Geology,

University of Fort Hare

26 November 2024

Supervised by Dr. Moses Magoba

ABSTRACT

This study aimed to integrate the petrophysical and petrographic analyses to characterize the Lower Cretaceous sandstone reservoirs for CO_2 geological storage in the Bredasdorp Basin offshore South Africa. These reservoirs are excellent for studying the potential CO_2 storage, since they are depleted oil and gas reservoirs with vast exploration data available. Four wells intersecting the Lower Cretaceous sandstone reservoirs were selected for this study, namely E-AQ1, E-G2, F-A10, and F-A13. Dataset use for the study included wireline logs, geological well completion reports, 1393 conventional core analysis, 13 core samples, 16 thin section slides, and micromorphology images for 8 core samples. Interactive Petrophysics software was utilized to evaluate the petrophysical parameters. Gamma ray logs were used to identify and delineate the sandstone reservoirs above 800 m depth to determine the reservoirs' porosity, clay volume, water saturation, and permeability. Data from core samples and well logs were used to estimate the pore throat size and to compute storage and flow capacity. The thin-section petrography combined with the Scanning Electron Microscopy-Energy Dispersive Spectroscopy (SEM-EDS) was employed to assess the influence of clay minerals on reservoir characteristics. The average calculated values for volume of clay, effective porosity, water saturation, and permeability varied between 12.66 - 30.73 %, 9.37 - 13.6 %, 6.17 - 68.88 %, and 6.68 – 502 mD, respectively. E-AQ1 and E-G2 exhibited low porosity of less than 10 %, whereas F-A10 and F-A13 showed good porosity of more than 10 %. F-A13 showed the highest permeability of 502.47 mD, while E-G2 showed the lowest value of 6.68 mD. E-G2 showed the highest clay volume at 30.73 %, while F-A13 showed the lowest value at 12.66 %. Furthermore, F-A10 showed the highest water saturation of 68.88 %, whereas well F-A13 showed the smallest value of 6.17 %. The pore throat radius revealed that F-A10 and F-A13 have a higher heterogeneity in the pore throat size distribution, and E-AQ1 and E-G2 showed the lowest heterogeneity, indicating that E-AQ1 and E-G2 will have a consistent fluid flow when CO_2 is injected. The storage and flow capacities ranged from 5.45 – 666.65 m and 12.43 – 9949.23 mD*m, respectively. Comparing the storage and flow capacities of E-G2, F-A10, and F-A13, E-G2 has the lowest storage capacity, and F-A10 has the highest. F-A13 has the lowest flow capacity, and F-A10 has the highest. The core description results for E-AQ1 showed a fine to medium-grained sandstone with glauconite, which is very calcareous. It has a calcite cement characterized by fracturing and tight cementation. E-G2 showed light grey, fine-grained sandstones, highly glauconitic, and visible bitumens. F-A10 showed medium to fine-grained, glauconitic, calcareous sandstones with better-preserved cross-bedding and heavily burrowed zones, indicating a high-energy depositional environment. F-A13 showed medium grey sandstones with varying grain sizes, visible pore spaces, and bioturbation, transitioning from fine-grained to medium-grained with depth. Thin section and SEM-EDS results show that the porosity for E-AQ1 was affected by quartz overgrowth and calcite cementation. E-G2 had carbonaceous material filling the pore spaces and compaction, thus affecting porosity. Feldspar overgrowth was observed from the intervals chosen for F-A10 and F-A13. Coarse grains were identified in F-A10, and they improved the overall porosity by creating larger spaces between particles. Glauconite was identified in all the wells. The most influential diagenetic processes impacting porosity, permeability, and water saturation included cementation (calcite and hematite), quartz and feldspar overgrowth, compaction, clay mineral authigenesis, and feldspar alteration. E-AQ1 showed poor reservoir quality due to quartz overgrowth reducing porosity and calcite cementation reducing permeability. On the other hand, F-A13 displayed a very porous sandstone reservoir containing smectite with a swelling nature, a needle-like illite, and an angular quartz grain, with calcite cementation and minimal compaction. The presence of clay minerals in the reservoir sands had a great impact on permeability and porosity. Based on the results and the criteria used, F-A10 and F-A13 are the most favourable reservoirs for CO_2 storage due to their high porosity, permeability, storage and flow capacities, low volume of clay and water saturation and favourable mineralogical characteristics that enhance reservoir quality. The results from this study can help guide future CO_2 storage projects by offering a clear understanding of the reservoir quality and how well these sandstone reservoirs can hold and transport CO_2. By knowing more about factors like porosity, permeability, clay volume, and water saturation changes over time, this study can help choose the best areas for CO_2 injection and predict how CO_2 will move through the rocks. This information can also help evaluate other similar reservoirs for CO_2 storage, supporting efforts to safely store carbon in South Africa and contribute to the global climate change mitigation and the transition to a low-carbon future.

Keywords: Geological Storage, Porosity, Reservoir, Permeability, Glauconite.

DECLARATION

I Hoza Siyamtanda student number 201715348 hereby declare that the work presented here is my original work and that it has not been published or submitted elsewhere for a degree program requirement. Any work done by others cited in this research has been acknowledged and listed in the reference section.

Date: 26 November 2024

Signature: S. Hoza

DECLARATION ON PLAGIARISM

I Hoza Siyamtanda student number 201715348 hereby declare that I am fully aware of the University of Fort Hare's policy on plagiarism, and I have taken every precaution to comply with the regulations. This document has been submitted through a similarity detection software and the report was reviewed by my supervisor. I declare there is no plagiarism in this honours research project.

Date: 26 November 2024

Signature: S. Hoza

DECLARATION ON RESEARCH ETHICAL CLEARANCE

I Hoza Siyamtanda student number 201715348 hereby declare that I am fully aware of the University of Fort Hare's policy on research ethics, and I have taken every precaution to comply with the regulations. I have obtained an ethical clearance certificate from the University of Fort Hare's Research Ethics Committee and my reference number is the following MAG051SHOZ01

Date: 26 November 2024

Signature: S. Hoza

ACKNOWLEDGEMENTS

First and foremost, I would like to thank God for giving me the strength, wisdom, and ambition to do this study. I would also like to thank my supervisor, Dr. Moses Magoba, for his support and guidance throughout this journey. A special thanks to the Petroleum Agency of South Africa (PASA) for providing the data used for this study. I also greatly appreciate the master's students who helped me in the Geology Department at the University of Fort Hare. I also express my gratitude to my family for being there for me.

Table of contents

List of Figures

List of Tables

List of Appendices

List of Acronyms

KL – Klinkenberg

Sw – Water Saturation

LLD – Resistivity Log

DT – Sonic Log

RHOB- Bulk Density

GR – Gamma ray log

NPHI – Neutron Porosity Log

VCLGR – Volume of Clay

PHIDEN – Porosity

SwSim – Water saturation

Calculated K - Permeability

Chapter 1

1 Introduction

1.1 Background information

Characterising sandstone reservoir rocks for CO_2 geological storage includes evaluating various properties such as petrography and petrophysics. Petrographic characterisation focuses on mineralogy and texture, while petrophysical characterisation focuses on properties like pore throat size, porosity, water saturation and permeability. These properties are part of the criteria for studying a potential geological formation for CO_2 storage. The motivation behind CO_2 geological storage studies is the effect carbon dioxide emissions have on the climate. During the 2009 Copenhagen climate change negotiations, South Africa vowed to decrease its emissions by 34% below projected levels by 2020 and 42% by 2025 on the condition that wealthy nations provide financial and technological support (Hicks et al., 2014).

Like many other nations, South Africa requires a portfolio of technologies to decrease CO_2 emissions; however, given that its economy is predominantly dependent on coal, carbon capture and storage (CCS) is anticipated to play a significant role in that portfolio (Chabangu et al., 2014). The South African government also founded the South African Centre of Carbon Capture and Storage (SACCCS) with help from international governments and local and international industries (Chabangu et al., 2014).

The 2010 Atlas on Geological Storage of Carbon Dioxide in South Africa states that the country has 150 Gt of potential CO_2 storage capacity, with 98% offshore capacity (Cloete, 2010). The sedimentary basins of Algoa and Zululand have the most significant onshore storage capacity, with some extra storage potential due to increased coal bed methane (Viljoen et al., 2012). Council for Geoscience (2010) indicated that capturing and storing carbon dioxide significantly reduced global climate change. When greenhouse gases such as CO_2 get released into the atmosphere by burning fossil fuels, they start to collect in the atmosphere.

This phenomenon is called the greenhouse effect, leading to global climate change, increasing sea levels, and strange weather patterns (Somma, 2021). CO_2 capture and storage is considered a technique for decreasing carbon emissions that could be essential in the fight against global warming (Sadeghi, 2016). It is a three-step procedure that involves collecting carbon dioxide produced during electricity production or industrial processes such as making steel or cement, transporting it, and burying it deep underground (National Grid, 2022). The three steps are as follows:

• Capturing carbon dioxide — CO_2 is extracted from other gases created during industrial operations like steel, cement, coal and natural gas-fired power plants.

• Transport: After separation, the CO_2 is compressed and moved through trucks, pipelines, or ships to a storage location.

• Storage: CO_2 is injected into underground rock formations for long-term storage.

Depleted oil and gas reservoirs or saline aquifers, usually located a kilometre or more below the surface, may be able to store carbon emissions (National Grid, 2022). The process of capturing and storing carbon is shown in Figure 1.1. Geological CO_2 storage, the final stage of the process, involves injecting the compressed gas into a porous rock formation for long-term removal (Bachu, 2000; Gaus, 2010). Sufficient geological settings for storing CO_2 include saline aquifers, deep coal seams, and depleted hydrocarbon reservoirs. These geological formations are composed of permeable, porous sedimentary rocks that contain a highly saline fluid (brine) in the fissures and dissolution cavities (carbonates) or the spaces between the rock's constituent grains (sandstones). They are typically deeper than freshwater aquifers and have limitations because of their structural location (Mateos-Redondo et al., 2018).

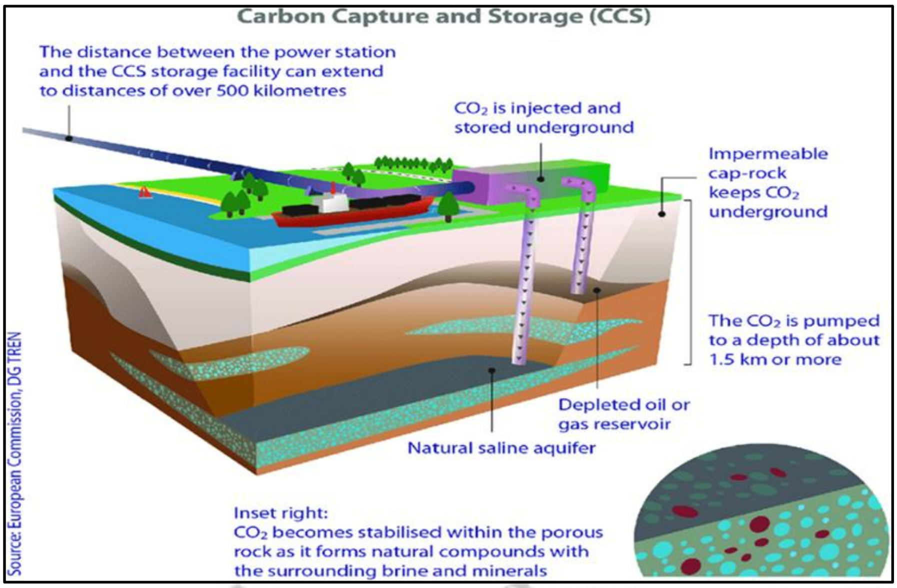

Figure 1.1 An Overview of Underground Carbon Storage. (Rissman et al., 2020)

1.2 Outline of Thesis

This thesis presents a detailed analysis evaluating the petrographic and petrophysical properties of the sandstone reservoirs in wells E-AQ1, E-G2, F-A10, and F-A13 in the Bredasdorp Basin. It consists of six chapters.

Chapter 1

Chapter 1 explains the topic of this study and provides background information about the topic. It also provides the research area’s location, problem statement, research questions, aim, and objectives.

Chapter 2

Chapter 2 explains the geology of the study area.

Chapter 3

Chapter 3 focuses on the theory of the well logs chosen for this study, the literature review, and the review of methods.

Chapter 4

Chapter 4 presents a petrophysical assessment of the chosen reservoirs in the study area, focusing on the results from the sandstone reservoirs studied.

Chapter 5

Chapter 5 looks at the effect of clay minerals on the reservoir quality using thin section slides, core description, and SEM-EDS analysis.

Chapter 6

Chapter 6 presents the conclusion and recommendations.

1.3 Location of the study area

The Bredasdorp Basin is found on the west-southwest of Port Elizabeth and southeast of Cape Town (Wood, 1995). It is the Outeniqua Basin's westernmost sub-basin. (Figure 1.2).

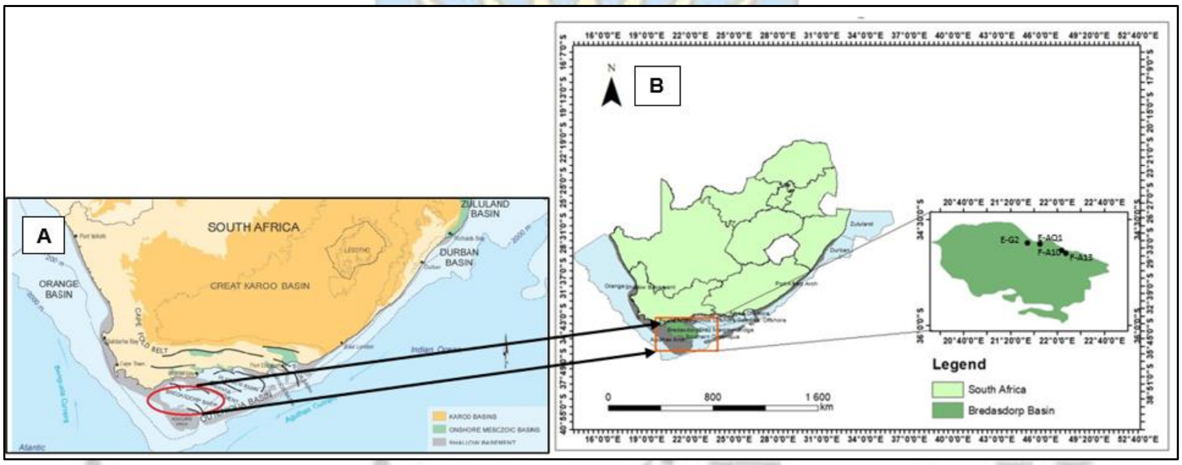

Figure 1.2 (A) Bredasdorp Basin Location Map (PASA, 2008), (B) Well Location Map Generated in ArcGIS.

1.4 Problem statement

A country-scale evaluation was conducted by Cloete (2010) to understand South Africa's CO_2 storage capacity. The study revealed that South Africa has approximately 150 Gt of potential storage. The offshore Mesozoic basins in South Africa have significant geological storage potential, with 98% distributed across the Orange Basin (west coast), Outeniqua Basin (south coast), and the Durban and Zululand Basins (east coast), with the remaining 2 % being onshore (Figure 3.1) (Chabangu et al., 2014). The Bredasdorp Basin, a sub-basin of the Outeniqua Basin, is recognised for its highly porous and permeable Lower Cretaceous sandstones, which have been extensively explored for oil and gas. These sandstone's high porosity and permeability make Bredasdorp Basin an ideal candidate for CO_2 geological storage studies. The success of CO_2 storage relies on understanding the petrographic and petrophysical properties of these reservoir rocks. There is a knowledge gap regarding the mineralogical composition and the impact of clay minerals on the petrophysical properties of Lower Cretaceous sandstone reservoirs in the Bredasdorp Basin, specifically for CO_2 storage studies. Consequently, this research aims to fill a gap by performing a petrographic and petrophysical characterisation of sandstone reservoir rocks in the Bredasdorp Basin, exploring their suitability and potential challenges for geological CO_2 storage.

1.5 Research Questions

- What is the potential sandstone reservoirs' thickness at depths greater than 800 m?
- What is the variation in permeability and porosity of sandstone reservoir rocks within the studied potential reservoirs?
- What is the mineralogical composition of the sandstone reservoirs in the Bredasdorp Basin?
- What impact do clay minerals have on petrophysical properties?
- How does the pore throat size affect CO_2 storage potential?

1.6 Aim and Objectives

The aim of the study was to examine the petrophysical and petrographic characteristics of sandstone reservoirs in the Bredasdorp Basin, South Africa, focusing on their potential for CO_2 storage. The specific objectives were to:

1. Identify sandstone reservoirs at depths greater than 800 metres using gamma-ray logs.
2. Evaluate the clay volume, permeability, water saturation, and porosity of the identified reservoirs through core data and well logs.
3. Calculate the pore throat size (using Winland Equation 1972), storage and flow capacity formulae from Gunter et al., (1997) and;
4. Conduct a petrographic investigation to assess the effect of clay minerals on porosity and permeability.

Chapter 2

2 Geological Overview of the Study Area

2.1 Basin evolution

The continental margin along South Africa's southern coast was formed due to the breakup of Gondwana during the Mesozoic era (Liro & Dawson, 2000). Numerous tectonic processes (rift and drift stages) that took place on the continental margin during this breakup resulted in the creation of the massive Outeniqua Basin and its sub-basins, which include the Gamtoos, Algoa, Pletmos, Bredasdorp, and Southern Outeniqua basins.

This basin was formed due to dextral shearing beside the South African margin, which began during the early to middle Cretaceous period. The Bredasdorp Basin resulted from rift tectonics that occurred during the breakup of Gondwana along South Africa's southern coast (Burden & Davies, 1997) (Figure 2.1). In the Falkland-Agulhas Fracture Zone (AFFZ), the parting of the Mozambique Ridge from the Falkland Plateau, which occurred simultaneously with the breakup of western Gondwana, was the cause of the right-lateral shear, or dextral trans-tensional stress movement, according to Tinker et al., (2008).

The separation led to the creation of graben and half-graben sub-basins, including the Bredasdorp Basin, and the development of average faulting north of the AFFZ (Brown et al., 1995). Normal faults that dip or slant in an identical direction cause adjacent fault blocks to slide or slip lower in relation to the neighbouring fault, resulting in half-graben structures (Schalkwyk, 2005).

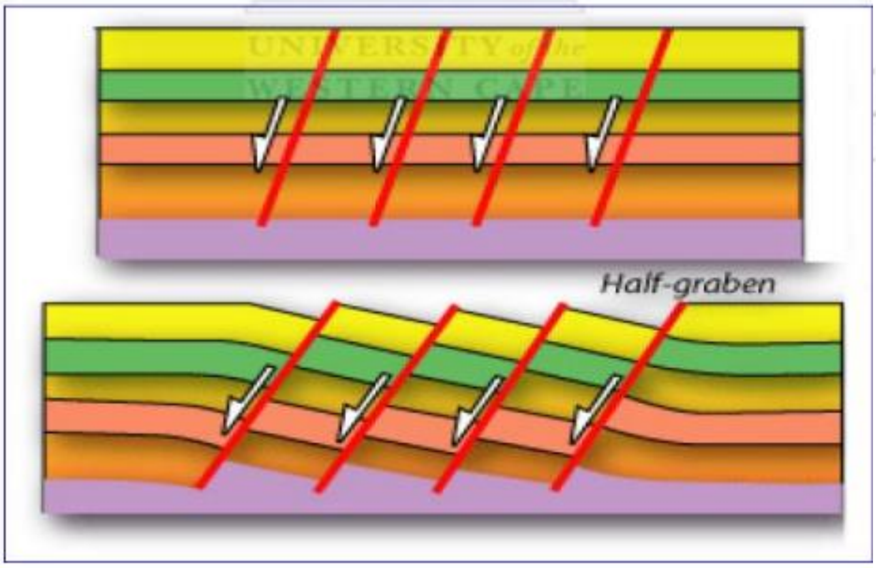

Figure 2.1 Half-Graben Development from Strings of Normal Fault Plunging is Similar (Burden, 1992).

Due to the extensional periods in the early rifting stages, the Bredasdorp Basin formed along the South African continental margin beneath the Indian Ocean between the Late Jurassic and Early Cretaceous. The Columbine-Agulhas Arch forms this basin's western and south-western boundaries, while the Cape Fold Belt and Infanta Arches form the northern boundary. The Diaz Marginal Ridge also forms the southern boundary of the basin (Figure 2.1). Extended basement highs are the granite from the Cape Supergroup and the Precambrian metamorphic rocks that make up the arches, as mentioned earlier. Despite being in Cape Infanta Agulhas, the basin has no onshore counterpart in the centre of two anticlinal-predominated basement highs.

2.2 Deposition setting

In the Bredasdorp Basin, the sediment deposition was greatly influenced by early continental rifting and tectonic evolution. Shallow marine and continental sediments deposited from the late Jurassic to early Cretaceous periods were the main cause of the basin's filling, which serves as a local depocenter (Turner et al., 2000). These syn-rift shallow marine and continental sediments were deposited down within the rift system after most of the faulting stopped about 126 million years ago (PASA, 2005). Accordingly, a drifting phase was followed by a transitional phase that was started by the syn-rift deposition (McMillan, 1997).

Three distinct phases characterise the tectonic history of the Bredasdorp Basin: the rift phase, the post-rift phase, and the early drift phase (Figure 2.3). Syn-rift basin fill, and extension-driven subsidence are features of the rift phase. The late-rift sediments were eroded and deformed by the isostatic uplift on both sides of the half-graben. On the other hand, parts of the syn-rift series were eliminated due to considerable erosion and marginal uplift on the northern side (PASA, 2005). The syn-rift and post-rift sequences are the two parts of the rift period.

Fluvial and shallow marine deposits make up the syn-rift sedimentary succession, whereas deep marine sediments make up the post-rift or drift series (Burden, 1992; De Wit, 1992) (Figure 2.2). The ongoing west-south-westward movements of the African tectonic plate along the southern coast are associated with the early and late events of the post-rift successions. The Outeniqua sub-basins were created because of these movements. Erosion truncation on the southern borders resulted from early drift combined with continuous uplift, and this happened just prior to the beginning of rapid thermal subsidence.

Within the graben, deep-water sediments quickly subsided and were deposited (PASA, 2005). The drift phase is characterised by regional subsidence brought on by thermal cooling and sediment loading. Until the early Tertiary, when an alkaline intrusion damaged the southern side, there was continuous (moderate) subsidence, which resulted in the uplift and erosion (PASA, 2005).

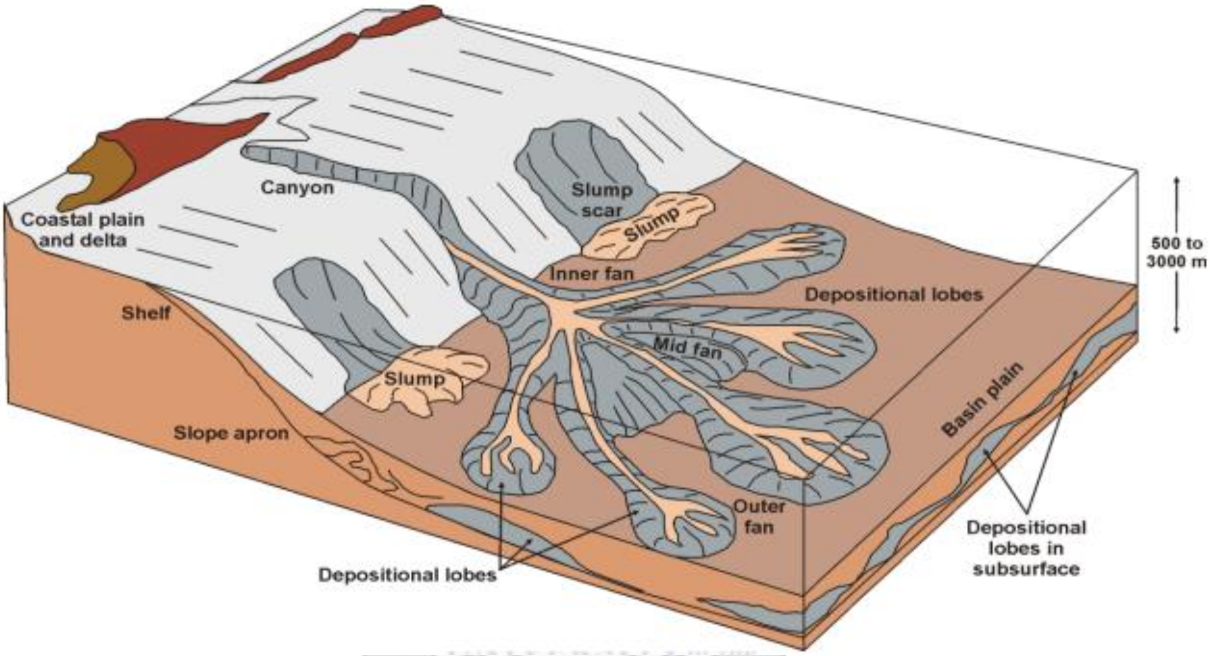

Figure 2.2 Evolution of the Deposits in the Deep Marine Channel (Petroleum Agency SA, 2008)

2.3 Stratigraphy

A stratigraphic column sitting above the Cape Supergroup rocks from the Oxfordian to Recent period is observed in the basin (McMillan, 1997). This column indicates that the first deposits comprised shallow marine sediments from the Albian to the Recent period. These sediments are covered by Late Jurassic fluvial syn-rift and shallow marine deposits from the Early Cretaceous (PASA, 2005). The geological column also reveals a Middle Jurassic to Early Cretaceous syn-rift phase, followed by an Early Cretaceous phase that transitions into the Tertiary post-rift phase (PASA, 2005).

Syn-rifts I and II are the two phases separating the sedimentation periods (PASA, 2005). The Late Valanginian to Hauterivian was when the syn-rift II phase happened. (PASA, 2005) On the other hand, the syn-rift I phase took place between the Middle Jurassic and Late Valanginian (from Basement to 1At1 and from 1At1 to 6At1). The syn-rift I succession ends with the 1At1 regional unconformity. This nonconformity also marks the start of the syn-rift II phase, which included new rifting because of early movements along the AFFZ at the Hauterivian-Valanginian boundary around 121 million years ago (PASA, 2005).

The transitional or early drift phase, which took place during the Hauterivian to Early Aptian periods, followed the syn-rift II phase from 6At1 to 13At1 (Figure 2.3). Tectonic events and changes in global sea levels caused progradation and aggradation periods during this phase, which is when the earliest deep-water deposits formed, mainly because of significant subsidence and increased water depth (PASA, 2005; Broad et al., 2006).

Moreover, the late drift phase followed the Early Aptian marine regression. The 13At1 unconformity, which was caused by this regression episode, is a prominent erosional feature. Under anoxic conditions, mudstone, shale, or claystone rich in organic matter was carried and deposited in the basin by a marine transgression after the erosion era (McMillan, 1997). The trailing edge of the Falkland Plateau cleared the Columbine-Agulhas Arch during the late Albian period (Broad, 2006). The late drift phase is known to begin at the 14At1 mid-Albian unconformity (Figure 2.3), which represents the start of active thermally driven subsidence.

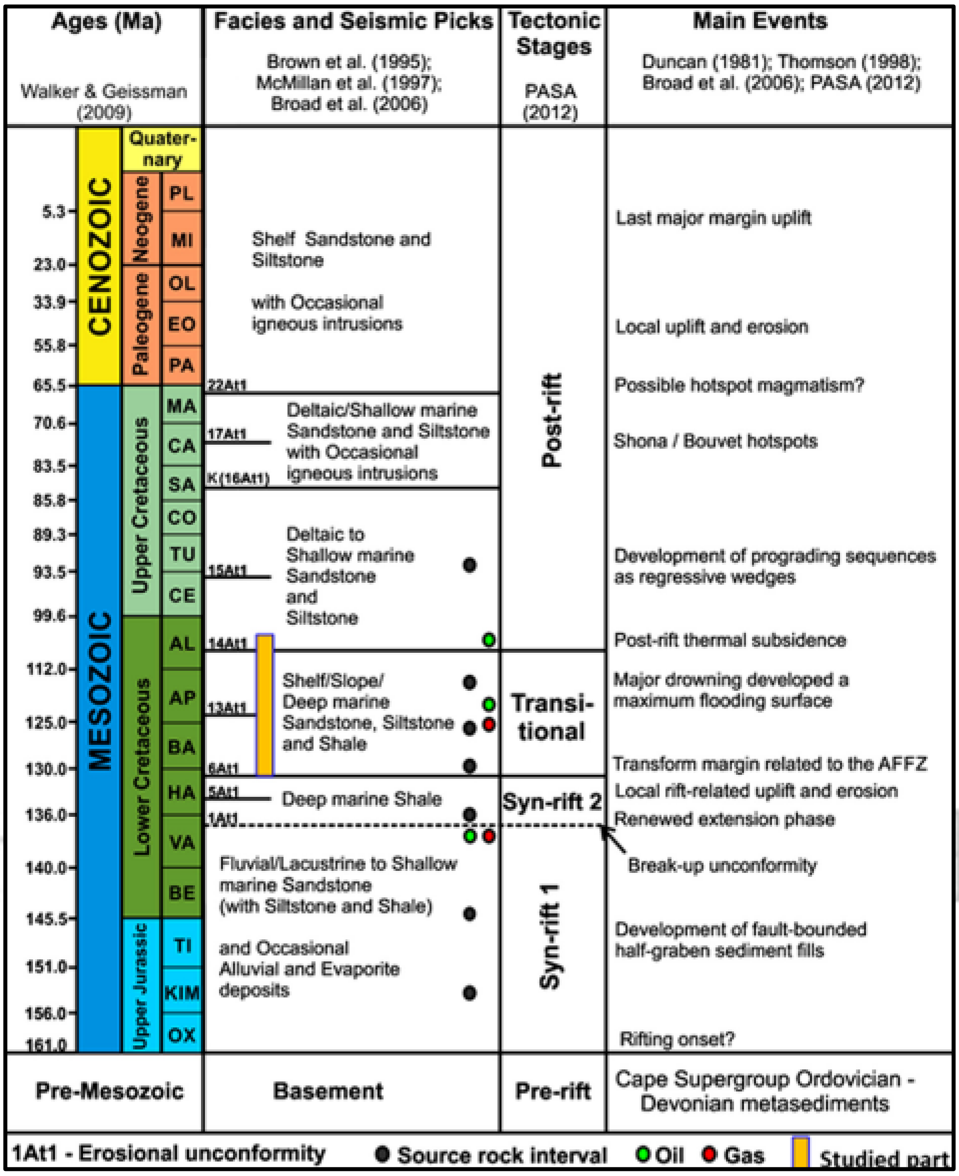

Figure 2.3 The Western Bredasdorp Basin's Chrono-stratigraphic Chart Shows the Main Unconformities and Tectonic Phases Relative to Geodynamic Events (Sonibare, 2015).

2.4 Structural Development of the Bredasdorp Basin

At Cape Infanta Agulhas, in the space between two anticlinal-dominated highs, sits the Bredasdorp Basin. A graben, or wide basement depression with an asymmetric cross-section, is the most appropriate term for the Bredasdorp Basin (Dingle et al., 1983). The southeast of Cape Agulhas is home to the spectacular subsurface feature known as the Agulhas Arch, whose faulting and gently northward tilting flank established the southern boundary of the Bredasdorp Basin.

The upper part of the arch, comprised of post-Palaeozoic rocks, including Bokkeveld shales and quartzite from the Table Mountain Group, covers the granite core, except the western section, which shows a northwest dip, the basin floor is primarily flat. The deepest areas are near the basin's northern margin (Dingle et al., 1983). The basement, which drops sharply along several small boundary faults originating from the Infanta Arch, defines the northern boundary of the basin.

Small, deep grabens break up the northern border's straight pattern by forming embayments into the Infanta Arch. Bound by minor, curving faults that raise them above the general level of the basin floor, three horsts stretch south and southeast into the basin. The western part of the Bredasdorp Basin does not continue onshore; instead, it narrows into a tiny graben that runs northwest-southeast to the coast, where it joins Cape Agulhas and Cape Infanta (Dingle et al., 1983).

The Rift Phase (Mid-Jurassic – Valaginian)

The syn-rift basin fill, and extension-driven subsidence were important features during the rift phase. Isostatic uplift caused the late-rift deposits to be eroded on both sides of the half-graben. Parts of the syn-rift series were destroyed by the considerable marginal uplift and erosion on the northern flank (PASA, 2004/5).

Early Drift Phase (Hauterivian – Early Barremian)

Southern flank erosional truncation occurred due to continuous uplift before the start of rapid thermal subsidence. Rapid subsidence and deposition of the deep-water series took place within the graben (PASA, 2004/5).

Drift Phase (Barremian – Turonian)

Thermal subsidence and sediment loading are the primary causes of regional subsidence, and some small displacement is still occurring on the Arniston Fault. In the early Palaeozoic era, the oil-rich source rock in the half-graben reached its primary stage of hydrocarbon generation. Alkaline processes drove uplift and erosion on the southern flank during the early Tertiary, although minor subsidence continued (PASA, 2004/5).

Chapter 3

3 Literature Review

3.1 A global perspective on the CO_2 storage potential

Understanding the accessible capacity for CO_2 storage is essential to effectively implement CO_2 capture and geological storage (CCGS) technology on a scale that can significantly reduce CO_2 emissions. Research into CO_2 storage capacity can be conducted at various levels, ranging from national to basin, regional to local, and even site-specific studies. This approach helps refine the analysis and increase resolution (Bachu et al., 2007). Three key concepts determine whether a basin has the potential to store CO_2. These include:

- Containment
- Capacity
- Feasibility

These three aspects can be further subdivided into fifteen criteria. Bachu (2003) established a 15-criteria method for basin examination and selection for geological CO_2 storage, which Gibson-Poole et al., refined (2008). The criteria are shown in the table below (Table 3.1).

Table 3.1 The Screening and Ranking Tool for Sedimentary Basins was Adapted from Bachu (2003) & Gibson-Poole et al., (2008).

Containment	Capacity	Feasibility
Tectonic setting	Size	Industry maturity
Depth	Aquifers	On/Offshore
Faulting intensity	Hydrocarbon potential	Climate
Salts	Geothermal regime	Accessibility
	Coals	Infrastructure
		CO_2 Sources

3.2 Overview of South Africa's CO_2 storage potential

South Africa conducted a national study to evaluate the country's CO2 storage capabilities. The findings were compiled and published in the Atlas of Geological Storage of Carbon Dioxide in South Africa (Chabangu et al., 2014). The Mesozoic basins of South Africa were found to have most of the storage potential (Figure 3.1). Of the 150 Gt of potential storage, 98 % is located offshore in the combined capacity of the Orange Basin (west coast), the Outeniqua Basin (south coast), and the Durban and Zululand Basins (east coast), with the remaining 2 % being onshore (Chabangu et al., 2014). According to Chabangu et al., (2014), South Africa's deep "unmineable" coal seams make up around 1 % of the country's onshore storage capacity, with the remaining 1 % being split almost evenly between the Zululand and Algoa Basins.

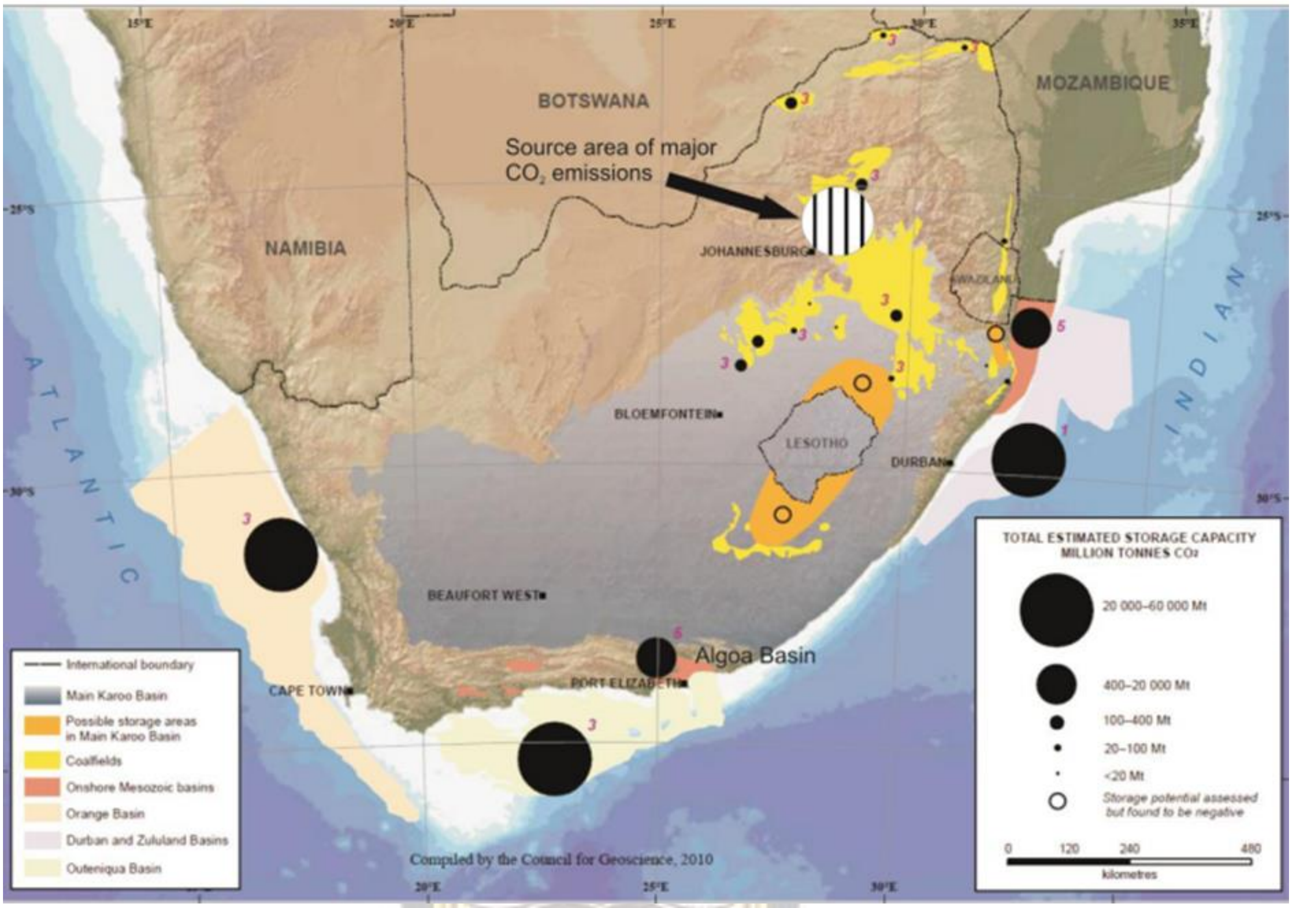

Figure 3.1 Potential Storage Sites in South Africa's Deep Saline Deposits. Purple Numbers in Each Basin Indicate the Data Confidence, Which is Scored Out of Five (updated after Hicks et al., 2012).

Seven potential locations were identified in the onshore Algoa Basin: six in the Sundays River Trough and one in the Uitenhage Trough (Chabangu et al., 2014). However, the Uitenhage Trough was not considered a viable site for CO2 storage because it is classified as a Subterranean Groundwater Control Area (SGCA), known for its very low salinity and relatively shallow groundwater reservoirs (Maclear, 2001). As a result, the Sundays River Trough was determined to be the only area in the onshore Algoa Basin with the potential for CO_2 storage capacity.

The six potential zones in the Sundays River Trough were defined by wells already in place and used as reference points to map potential sandstone packages (Figure 3.2). These include the Addo Trough, the Colchester Trough, and the Nanaga Anticline. The Alexandria, Seaview Structure, and Springmount regions, all of which hold sandstone packages with entirely restricted lateral extent, were also detected.

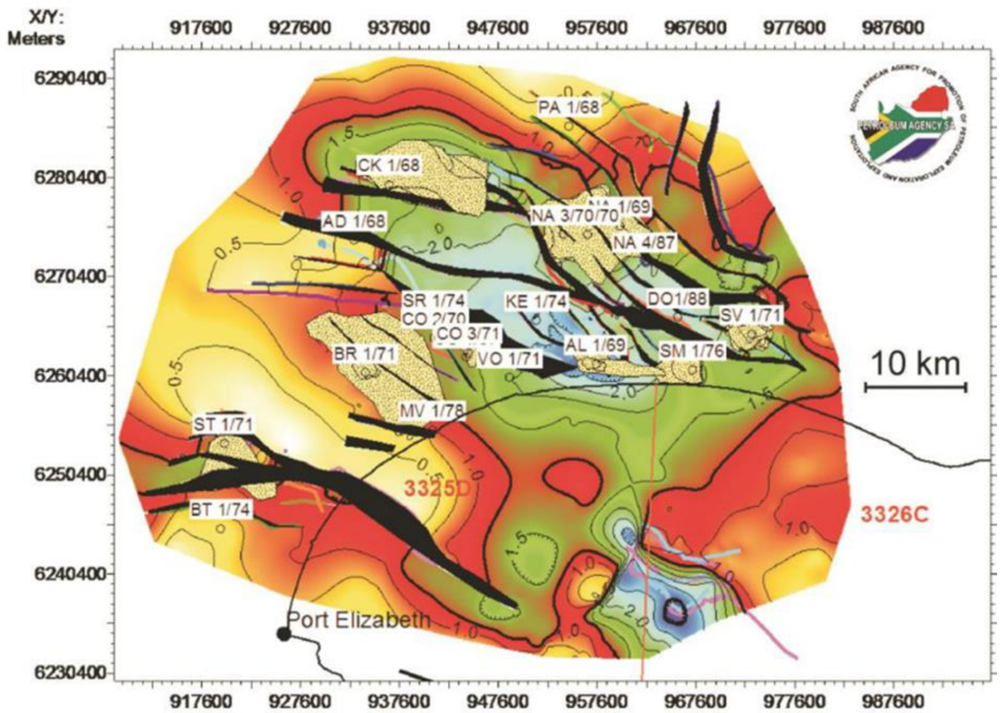

Figure 3.2 Mapped Sandstone Reservoirs in the Algoa basin. The Broad Black Lines, Which Show that Many Reservoirs are Structurally Bound, Define Faulting. A Coloured Contour Map that Shows the Basin's Deepest and Nearest Surface Areas (blue) is used to Define the Depth of the Basin. Two-way Time is Used for Depth Contours (modified after Hicks et al., 2012).

While many sandstone packages were discovered at different depths in each of the six prospects, some were not chosen as CCS prospects because of inconsistencies in the porosity and permeability values. Estimates of storage capacity were created for each prospect. Then, factors such as injectivity, containment, site planning, storage capacity, and the presence of natural underground sources were used to evaluate and rank each prospect's eligibility for PCSP regions (Table 3.2). According to available data, the Seaview Area, Colchester Trough, and Nanaga Structure in the Algoa basin have the best potential CCS prospectivity.

Table 3.2 Ranking of Potential Areas/Sites within the Algoa Basin (Chabangu et al., 2014)

Ranking (based on score)	Areas/Site	Storage potential using 1 % storage coefficient (Mt)	Storage potential using a 4 % storage coefficient (Mt)
1	Nanaga	3.04	12.16
2	Brak River (Colchester Trough)	2.33	9.33
3	Springmount	0.81	3.24
4	Seaview	0.78	3.11
4	Addo Trough	1.11	4.46
6	Colchester Trough	0.07	0.29
6	Alexandria	0.20	0.77

The Zululand Basin was also investigated, and it was found that within the northern Kosi Trough, three layered sandstone packages were discovered, with one package discovered in the southern St Lucia Trough. The only sandstone units deep enough to be used as CO_2 storage sites were the middle and lower ones in the Kosi Trough in the northern Zululand Basin. Due to CCS depth restrictions, only two of the six sandstone packages with different reservoir characteristics were examined (Chabangu et al., 2014).

The lower potential reservoir is the Aptian-aged sandstone found in the Makatini Formation. On the other hand, the sandstone succession in the lower sandstone reservoir of the St. Lucia Formation and the upper sandstone reservoir of the Makatini Formation extends from the upper Cenomanian to the Turonian period. Both reservoir packages are well-developed in the Kosi Trough. The literature on the Zululand basin indicates that the Aptian sandstone is the only reservoir deep enough to provide resourceful CO2 storage.

However, its permeability is limited, measuring less than one millidarcy (mD). Due to data limitations, the western boundary of this unit is still being determined, even though it appears to display a lateral pinch-out to the south and east. Based on current 4 % efficiency factor estimates, possible storage capacities range from 228 to 2599 Mt CO_2. However, because of the absence of permeability, storage capacity based on a 1 % efficiency factor suggests a potential capacity of 57.2 Mt CO_2. Even though the unit is deep enough for CO_2 injection into the supercritical phase, the unit's extremely low permeabilities will likely limit or even prohibit injection.

However, a closer look at the literature on the Durban basin reveals a few gaps and shortcomings. The rock most suitable for CO_2 is a sandstone, of which the Durban Basin has claystone with only minor sandstones (McMillan, 2003). The potential has only been theorised and is yet to be proven because the probable sites in the Durban Basin remain undrilled. There is also a need for more reservoir data, leading to the inaccuracy of the proposed reservoir storage calculations. Hicks et al., (2014) state that the permeability and porosity data were taken from analogue formations within the onshore Zululand Basin in the north.

3.3 Overview of the Bredasdorp Basin CO_2 storage potential

The Southern Oil Exploration Corporation and a few other oil corporations searched the Late Jurassic to Early Cretaceous synrift sandstones of the Bredasdorp Basin about 20 years ago for structural traps (Baiyegunhi et al., 2020). Hydrocarbons are thought to have originated from one or more carbon-rich source rocks situated in the western region of the southern Outeniqua Basin or within its boundaries (Acho, 2015). These hydrocarbons, believed to be remnants of earlier oil deposits, consist of liquid oils, wet gas with condensate, and traces of high molecular weight hydrocarbons (Acho, 2015).

Below horizon 13At1, reservoirs of gas with condensate or oil have been discovered all over the basin. Condensate-rich gases are below 9At1, whereas condensate-poor gases are below 1At1. Oil reserves have been discovered mainly in Albian (14A) sandstones in the basin centre, with a few wells on the north side below horizon 1At1 (Acho, 2015).

Petrophysical parameters and geophysical tools were used to evaluate the reservoirs in the Bredasdorp Basin. The same parameters were also used in the examination of the CO_2 storage capacity in the basin, focusing on permeability and porosity. Since hydrocarbons were extracted in the basin, CO_2 storage can occur. Acho (2015) studied E-BD2, E-BB1, and E-A01 wells. E-BD2 had the highest porosity and permeability out of the three wells studied. With porosity being 19.8 % and permeability being 935.94 mD.

Djebbar & Donaldson (1999) suggested that lithology with porosity ranges from 15 - 35 % is classified as 'reservoir' sandstones, and permeability ranging from 50 – 250 mD are classified as high. When it comes to the permeability and porosity of the study area, these properties differ inside the well, which is caused by the different lithologies found and their depths. For example, Maseko (2016) studied two wells, well D-D1 and well E-AP1. Well D-D1 had a 1.2 % and 2.7 % porosity, resulting from claystone and siltstone at 2859.7 m and 2864.6 m, respectively.

When the volume of pores is good enough, CO_2 storage can occur. Geomechanical characterisation was used to study the potential of the Bredasdorp Basin in CO_2 storage (Saffou et al., 2020). The study was conducted at a depth of 2570 m, separating a prevailing typical faulting system within the caprock and the reservoir, with detailed quantification of principal vertical, minimum, and maximum horizontal stresses (Saffou et al., 2020).

Compartment C3 showed severe normal faulting, which required more attention in the context of CO_2 storage. Saffou et al., (2020) assessed the fault reactivation and fracture stability, which exhibited stability in compartments C1 and C2 post-depletion, while highlighting possible risks in C3, mainly concerning the reactivation of normal faults (FNS8 and FNS9) and critically stressed fractures. The mitigation of geomechanical risks occurred by creating a sustainable maximum fluid pressure of 25 MPa.

Afolayan et al., (2023) investigated the CO_2 storage potential of the Bredasdorp Basin through the development of a 3D static model. The reservoir was characterised as a sandstone formation, with an effective porosity of 13.92 % and permeability ranging from 100 to 560 mD. The petrophysical parameters showed facies control, specifically in the southwestern area, where shale facies and siltstone dominance decreased permeability and porosity. In the volume shale model, the reservoir showed clean sands with water saturation values of 10 % to 90 %, making it a good reservoir for storing CO_2 based on its favourable petrophysical characteristics.

The feasibility of CO_2 storage in an offshore oil reservoir within the Bredasdorp basin, South Africa, was also investigated using dynamic modelling but without employing enhanced oil recovery (EOR) (Afolayan et al., 2023). A closed boundary and an open boundary were studied. The closed boundary, categorised by an objective injection rate of 0.5 Mt/year, experienced a pressure buildup. Because of the reservoir's confinement and the smaller amount of CO_2 that was injected, the CO_2 plume's migration was restricted.

Although gravity dominated the model's behaviour, gravity stability was not attained by the simulation's conclusion (Afolayan et al., 2023). The findings showed that between 2050 and 2150, there was a decrease in the gaseous mobile CO_2 phase and an increase in CO_2 dissolved in water and oil (Afolayan et al., 2023). With 10.4 Mt of CO_2 injected, the intended injection rate of 0.5 Mt/year was successfully achieved because there was no pressure building in the open border.

The studies mentioned previously concentrated on the permeability and porosity of oil reservoirs. This research aims to evaluate the effects of clay minerals on the petrophysical parameters in depleted oil and gas reservoirs. Clay minerals significantly influence petrophysical characteristics, particularly porosity and permeability. Their presence can notably alter the petrophysical properties of rocks, especially in sandstone reservoirs. As a result, the ability of a reservoir to store and transmit fluids can be compromised by the reduced porosity and permeability associated with clay minerals.

3.4 The Theory of Well Logs

A wireline log is one of the most significant data types available to reservoir geoscientists and petrophysicists; it provides a continuous record of borehole measurements that can be used to interpret a reservoir's depositional environment, petrophysical properties, and fluid distribution. In other words, wireline logs assist in determining whether the rocks contain oil and gas and evaluating whether those resources will flow. Geophysical well logs come in different types. The information in a geophysical log can be accurate (for example, utilising specific values to calculate water saturations) or interpretive (for example, correlating stratigraphy using simple pattern recognition or recognising a segment repeated by faulting) (Evenick, 2008). Only a few of them were employed in this investigation.

3.4.1 Gamma Ray Log (GR)

A gamma ray tool is designed to detect natural radioactivity within geological formations by responding to minerals abundant in uranium, potassium, and thorium (Connor, 2016). The tool provides a minimal response when only trace amounts of these minerals are found in quartzose sandstone. Since it has important quantities of uranium-rich minerals produced by the reduction of decomposing organic matter, organic-rich marine shale frequently shows the strongest reaction (Connor, 2016). Unless they include a lot of uranium or detrital clay, carbonates have a poor gamma-ray reaction (Connor, 2016).

The gamma-ray curve distinguishes between shales and reservoir rocks. Consequently, the gamma log can be used to determine lithology. The volume of shale in the formation can be determined using the gamma-ray log, as seen in Figure 3.3. The API (American Petroleum Institute) is the common unit of measurement and for the gamma-ray log it usually ranges from 0 to 200 API units. The existence of radioactive sands, such as potassium-rich feldspathic, glauconitic, or micaceous sandstones, is usually suggested by high gamma rays rather than shaliness (Rider, 2002).

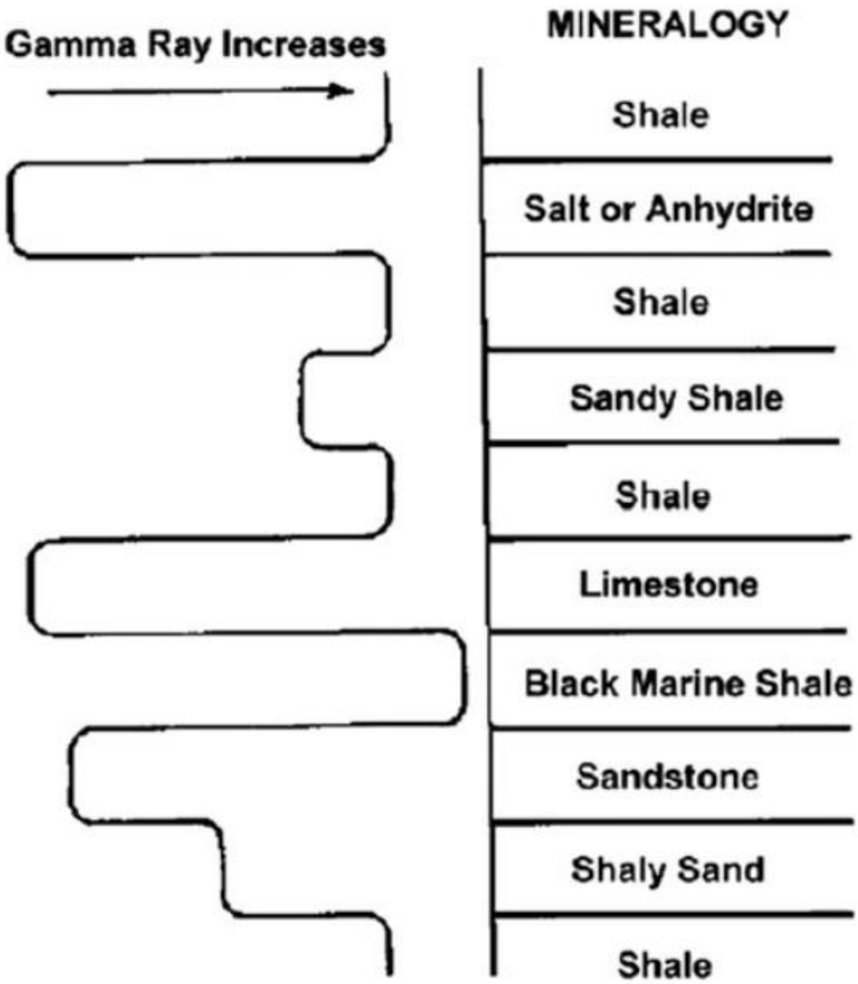

Figure 3.3 Illustration of the Gamma-ray Curve of Sedimentary Rocks (Liu, 2017)

3.4.2 Resistivity Log

Resistivity logs are often used to differentiate between water-bearing and hydrocarbon-bearing intervals in geological formations. They can also locate permeable horizons and assess porosity (Connor, 2016). The rock matrix and hydrocarbons are normally resistant to electrical movement, therefore the only electrically conducting material in a formation is the water trapped by clays or confined in pore spaces. A current is created in the formation by resistivity instruments, which then measures the formation's reaction to the current. This reaction depends on the amount and salinity of the formation water; fresher water responds more strongly than salinised water (Connor, 2016).

Resistivity logs are usually displayed across tracks 2-3 of a normal API display or in track 2 of a sonic log display. The scale, which runs from 0.2 to 200 or 2000 ohm-meters (ohm m), is always logarithmic.

3.4.3 Neutron Logs

The hydrogen index (HI) measured by neutron logs is the concentration of hydrogen in a formation. Water or hydrocarbons are the most frequent sources of hydrogen in a formation. The neutron log measures the liquid-filled porosity in rocks without shale that contain water or oil in their pore spaces. A decreased porosity reading from the instrument results from a reduction in hydrogen concentration when the pores are filled with gas. A 'cross-over' with the density log occurs in a porous and permeable zone when the neutron porosity is less than the bulk density (Connor, 2016).

Assuming a zero porosity condition, neutron data from limestone or sandstone is frequently calibrated to a standard response using porosity units. But in the presence of shale, the neutron log overestimates the porosity of the formation by reacting with the water trapped in the clay particles (Connor, 2016).

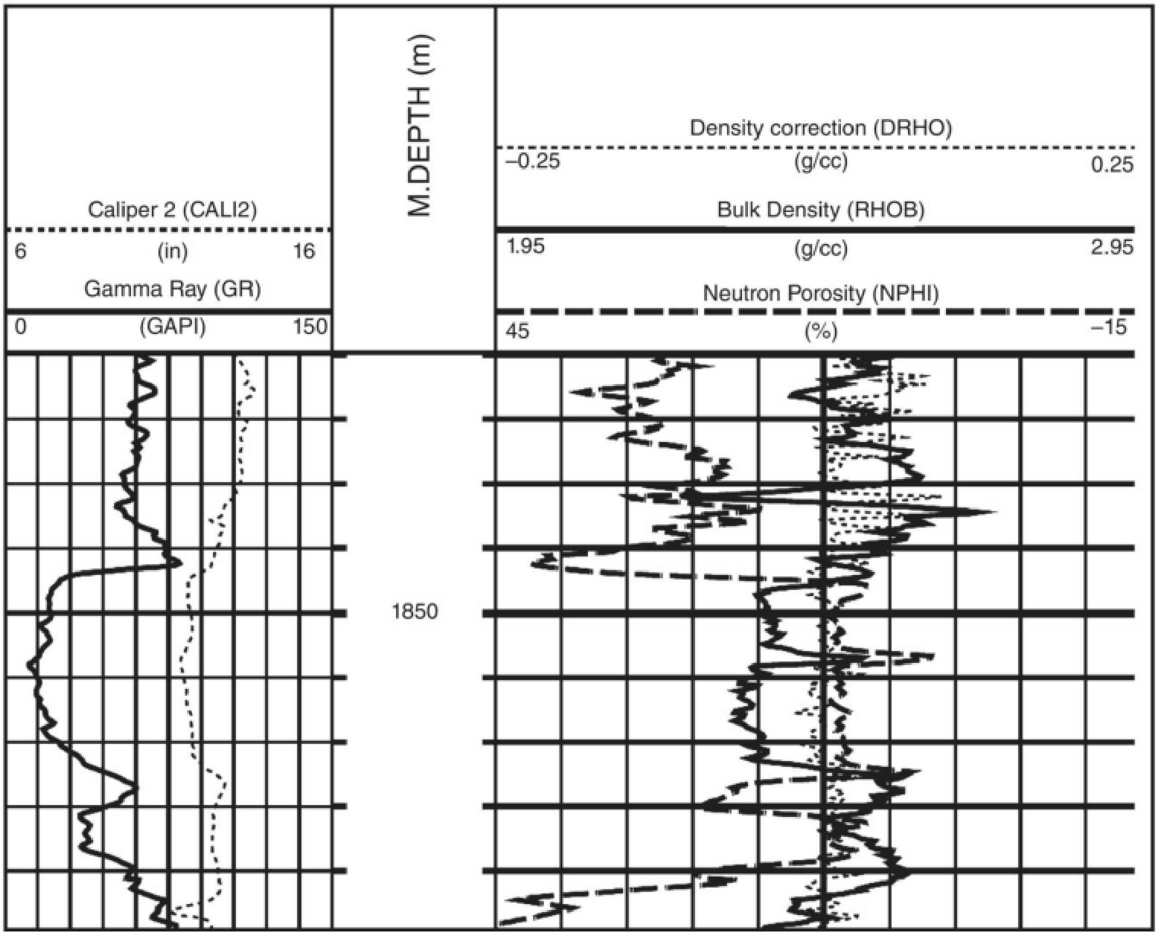

Figure 3.4 The Compensated Neutron Porosity Tool: Mode of Operation, Applications, and Typical Display (Connor, 2016).

3.4.4 Density Logs

Using the expected density of the formation and drill fluid, a density log calculates the formation's porosity in grams per cubic centimetre (g/cm^3) (Evenick, 2018). Because the measured bulk density in a gas-filled formation is lower, the standard porosity calculation will overestimate the porosity. Densities are low in shale, coal, and bentonite beds but high in sandstones and carbonates. The grain density of sandstone is usually 2.65g/cm^3 (Serra, 1984):

3.4.5 Sonic Logs

The transit time of a compressional sound wave as it moves along the borehole wall's axis is measured by the sonic log. Although it can pass through gases, liquids, and solids, this sound wave moves through solids the quickest. As a result, the sonic device captures the formation's matrix porosity. Additional techniques are required to assess the formation's overall porosity in situations when vugs or secondary porosity are present, as is the case with many carbonates and sandstones.

One or more ultrasonic transmitters and two or more vertically aligned receivers make up a sonic instrument. The consequences of borehole rugosity are lessened and compensated for using this configuration. The transit time (t) is directly proportional to the sound wave's velocity as it passes through the formation and is expressed in microseconds per foot or metre (s/ft or s/m). This velocity is determined by the properties of the formation, including fluid-filled porosity and lithology. On track 3 of a conventional API display, the acoustic log is usually shown on a scale of 40-140 s/ft, with slowness increasing to the left of the display (Connor, 2016).

3.5 Review of Methods

3.5.1 Core Grain Density

In rock evaluation, grain density is defined as the density of the grains within a formation or core sample (Schlumberger, 2013). In the analysis of logs and core samples, the word "grain" encompasses all solid materials found in the rock, with no distinction made between the grains and other solid materials. Matrix densities for various lithologies are shown in Table 3.3.

Table 3.3 Matrix density of typical lithology (Schlumberger, 2013).

Lithology	Matrix value (g/cm^3)
Clay mineral	2.02-2.81
Chlorite	2.81
Illite	2.61
Kaolinite	2.55
Smectite	2.02
Coal	1.19
Halite	2.04
Sandstone (Quartz)	2.65
Limestone	2.71
Dolomite	2.85
Orthoclase	2.57
Plagioclase	2.59
Anhydrite	2.98

Siderite	3.88
Pyrite	4.99

3.5.2 Core Porosity

The ability of a rock to hold liquids like water, gas, or oil in its pore spaces is known as porosity (Rider, 2002). Such spaces can be found in rock or soil cracks, between particles, or inside cavities. Porosity can be represented as a percentage between 0 % and 100 % or as a fraction between 0 and 1 (Glover, 2001). Porosity normally varies from less than 1 % to as much as 40 % for many rock types. Because porous rocks are good at storing fluids, they are essential to oil and gas reservoirs. The porosity estimates derived from well-log data are often calibrated using core porosity (Crain, 2013).

Two distinct types of porosity are measured using different methods. Effective porosity is assessed using the gas expansion method, while total porosity is calculated by destructively examining the sample to estimate its grain volume (Opuwari, 2010). Effective porosity represents the volume of interconnected pore spaces within the rock. In contrast, total porosity refers to the overall volume of the rock that can be occupied by fluids, encompassing interconnected and isolated pore spaces. The porosity of reservoirs generally ranges from approximately 5 to 47.6 %.

Several factors play a role in determining porosity, including particle sorting, grain packing, compaction, and cementation. The effective porosity is greatly reduced when bigger sand grains are combined with smaller particles, such as silt or clay (Djebbar and Donaldson, 2015). Soft, unconsolidated rocks tend to have high porosities, whereas well cemented sandstones usually have low porosities (Djebbar and Donaldson, 2015). Both lithification and the alteration of rocks by circulating groundwater result in cementation.

Common cementing materials include calcium carbonate, dolomite, clays, and various combinations of these substances. Furthermore, compaction affects porosity by decreasing the volume of interconnected pore spaces.

The classification of the porosity of a reservoir is shown in the Table 3.4 below:

Table 3.4 Classification of Reservoir Porosity (Modified after Djebbar, 1999).

Porosity values (%)	Classification
0 – 5	Negligible
5 – 10	Poor
10 – 15	Fair
15 – 20	Good
> 20	Very good

3.5.3 Core Permeability

The ability of a fluid to pass through porous medium is measured by its permeability (Glover, 2001). A rock's effective porosity, which is impacted by various elements such grain size, shape, distribution (sorting), and packing, determines its permeability. Another important factor influencing permeability is the degree of cementation and consolidation. Permeability can also be affected by the kind of cement or clay that exists between sand grains, especially in freshwater environments. Depending on the characteristics of the reservoir, rocks can exhibit permeabilities that range from less than one millidarcy (mD) to over 1000 mD. This study calibrated the permeability values obtained from log curves against core permeability data. Liquid permeability was utilised to evaluate consistency throughout the research.

The classification of the permeability of a reservoir is shown in the Table 3.5 below:

Table 3.5 Classification of the Permeability of a Reservoir (Modified after Djebbar, 1999).

Permeability Values (mD)	Classification
Less than 1	Poor
Between 1 and 10	Fair
Between 10 and 50	Moderate
Between 50 and 250	Good
Above 250	Very good

3.5.4 Porosity versus Permeability Relationship

Permeability is vital in the hydrocarbon industry since it dictates the feasibility of extracting fluids from reservoir rocks (Glover, 2001). The most significant factor affecting permeability is porosity. An essential technique for analysing permeability data involves plotting it on a logarithmic scale using a poroperm cross-plot diagram (Figure 3.5).

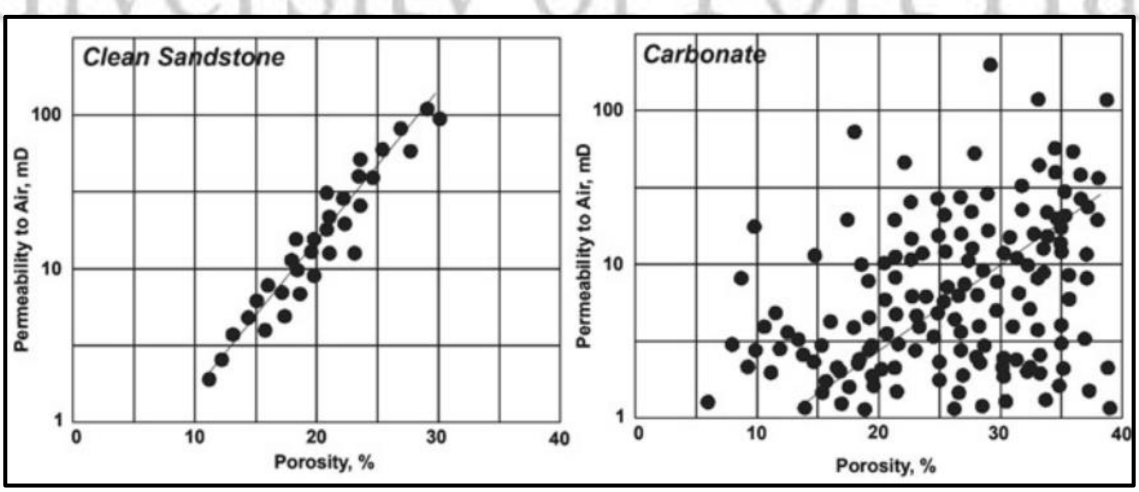

Figure 3.5 Poroperm Cross-plots (Glover, 2001).

To achieve better results, poroperm cross-plots must be created for clearly defined reservoir zones. Typically, a relationship exists within specific rock units, and the variations between different rock units can be significant in reservoir rock analysis

(Glover, 2001). The primary purpose of the poroperm cross-plot is to assess the strength of the relationship between porosity and permeability. For instance, the data presented in Figure 3.6 illustrates that in clean sandstone, porosity influences permeability. In contrast, the carbonate plot shows more scattered data, indicating that while porosity has an effect, other primary factors also govern permeability (Glover, 2001). It is common for some carbonate reservoirs to exhibit high porosity but low permeability due to a lack of interconnection between the reservoir's effective porosity, such as vugs or cavities. Figure 3.6 presents the poroperm relationships for various lithologies.

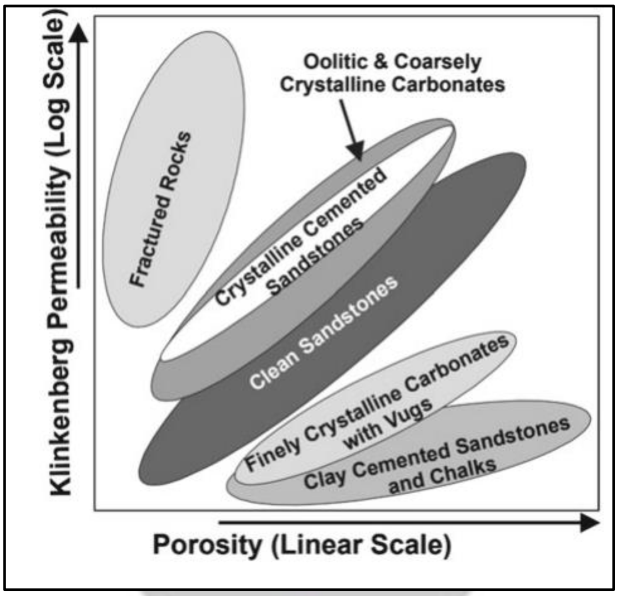

Figure 3.6 Poroperm Relationships for Different Lithologies (Glover, 2001).

3.5.5 Fluid Saturation

Understanding the porosity of a reservoir is essential because it indicates the rock's ability to store fluids such as oil, gas, and water. Similarly important is the degree to which the pores of the rock are filled with specific fluids, known as fluid saturation. This property is a fraction or percentage of the total pore volume occupied by oil, gas, or water. Fluid saturation is crucial for determining initial reserves and significantly influences the flow properties of the reservoir, mainly through its effect on relative permeability. For this study, water saturation (Sw) was considered.

Chapter 4

4 Petrophysical Interpretation of Sandstone Reservoirs

4.1 Introduction

The effectiveness of CO_2 storage in sandstone reservoirs depends on the physical and chemical properties of geological formations that are used for storing CO_2 underground (Munish & Lauderdale-Smith, 2024). Understanding the petrophysical properties of sandstone reservoirs is crucial for CO_2 storage because properties such as volume of clay, water saturation, porosity, pore throat size distribution, and permeability play an essential role in storing CO_2. Higher porosity generally leads to increased storage capacity.

Permeability, on the other hand, influences CO_2 movement within the reservoir. Higher permeability enhances CO_2 storage by improving injectivity (Yu & Uchida, 2020). Water saturation influences the spreading and mixing of water and CO_2 in porous media, which is crucial for long-term storage (Abbaszadeh & Shariatipour, 2018). This chapter will focus on properties such as clay volume, permeability, water saturation, porosity, pore throat size, and 3D parameter viewer to better understand the reservoir properties and their distribution.

Specific requirements must be met before storing CO_2 underground. The reservoir in question should be a depleted oil and gas reservoir, specifically of the sandstone type, as sandstones are generally highly porous and permeable. An impermeable caprock must be present to prevent any flow or leakage to the surface. Furthermore, the reservoir must be situated at a depth greater than 800 metres to ensure the CO_2 remains in its supercritical state (Agartan et al., 2018). Petrophysical evaluation involves analysing the chemical and physical parameters of the rock-pore-fluid system using geological data, fluid samples, well logs, and reservoir rock.

4.2 Aims and Objectives

This chapter aims to perform a petrophysical analysis of the selected sandstone reservoirs to assess their suitability for CO_2 storage. The study focused on various physical rock properties, including the volume of clay, porosity, permeability, water saturation, and the distribution of pore throat sizes across the selected reservoir intervals. The research objectives were to:

- Interpret the conventional core analysis data.
- Identify potential sandstone reservoirs below 800 metres using gamma-ray logs and core samples.
- Calculate the clay volume from the gamma-ray log in the chosen reservoirs.
- Calculate porosity, permeability, and water saturation in the identified reservoirs and validate the log-derived results with the core data wireline logs
- Calculate pore throat radius using Winland Equation (1972).
- Calculate storage and flow capacity using formulae from Gunter et al., (1997)
- Create a 3D parameter viewer for the True Vertical Depth model using Geoactive Interactive Petrophysics (IP) 4.3 to illustrate the distribution of calculated reservoir parameters across the study area.

4.3 Methodology and Materials

4.3.1 Analysis of Data

The data used in this study was gathered by Schlumberger Service Company and supplied by the Petroleum Agency of South Africa (PASA). The dataset included the following: geophysical wireline logs in LAS format, conventional core analysis, core description, and geological well completion reports. The wireline log data was organised, sorted, and cautiously prepared for easy access before being loaded into Interactive Petrophysics (IP) 4.3 for display as log curves.

4.3.2 Log editing: Environmental Corrections

Any material between the measuring probe and the target rock can distort or severely influence gamma radiation measurements (Lehmann, 2010). The primary causes of the impacts are cementation, drill pipe, well fluid, casing, etc. Thus, to facilitate log correlations and provide quantifiable rock properties, environmental correction of wireline logs is a crucial processing step (Lehmann, 2010). The adjustments to E-AQ1, E-G2, F-A10, and F-A13 focused on the gamma-ray log. The following parameters were used for the corrections:

- Bit size
- Mud weight
- Mud sample – resistivity and temperature
- Mud cake sample – resistivity and temperature

Figure 4.1 shows the log before environmental corrections (Gr_Splice) and after environmental corrections (GrC).

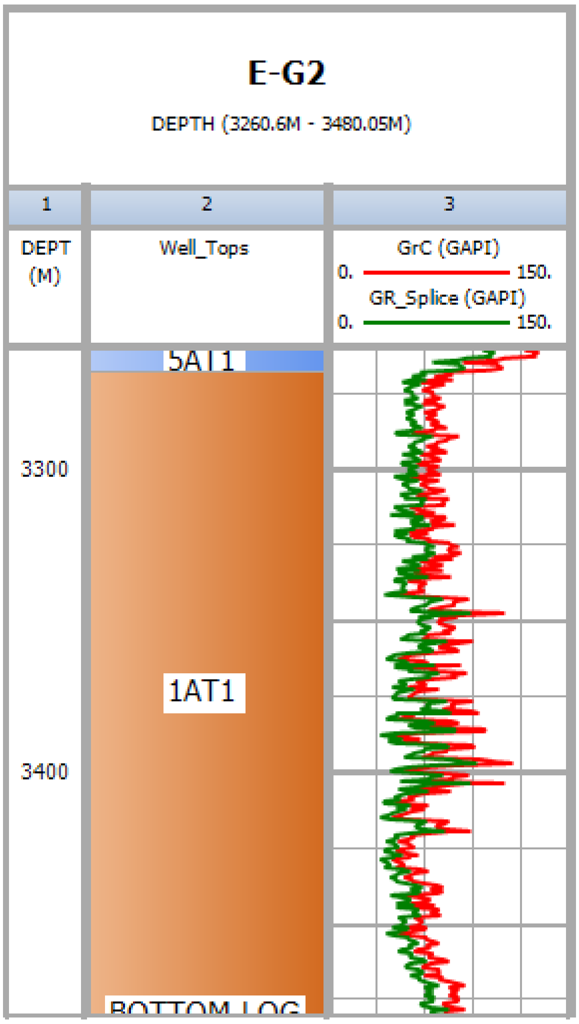

Figure 4.1 Example of the Log Before and After Correction.

4.3.3 Log Splicing

Log Splicing combines more than one LAS file for a well or multiple curves of the same type in a LAS file to ensure complete data coverage (Snow, 2021). Figure 4.2 and Figure 4.3 show examples of logs before and after splicing.

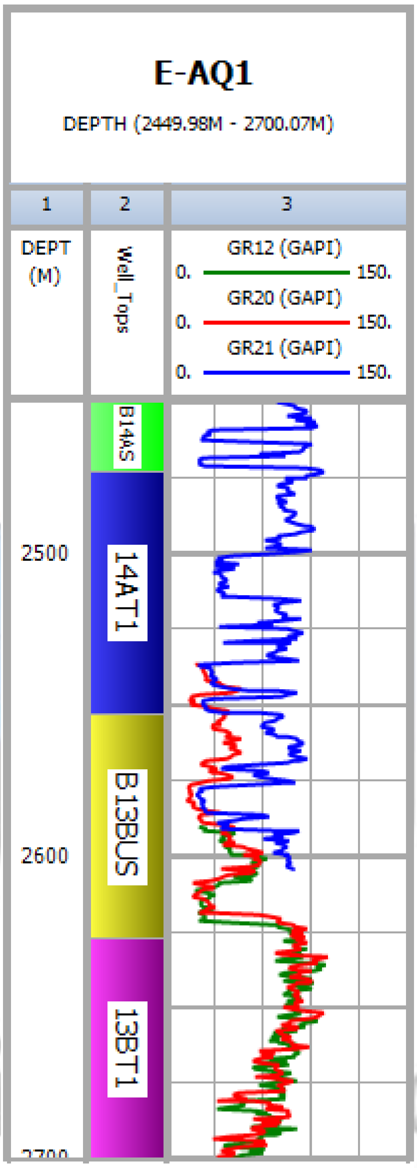

Figure 4.2 Example of Gamma-ray Logs Before Splicing.

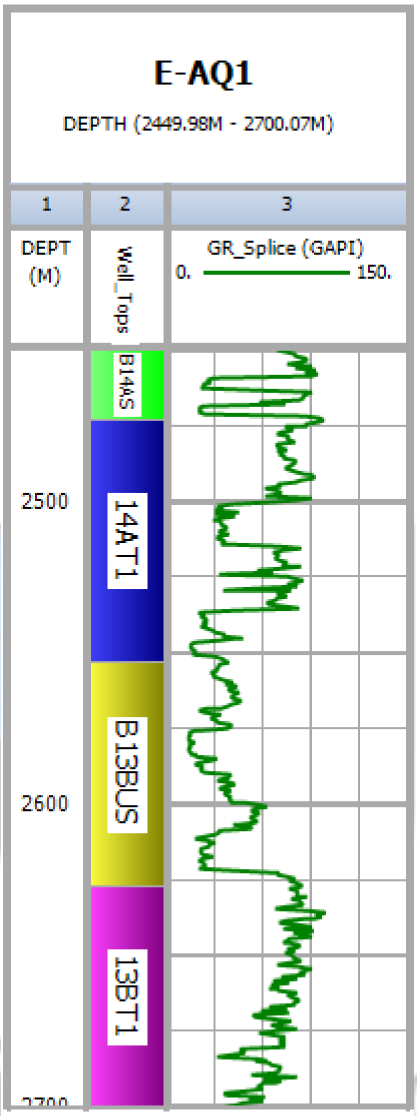

Figure 4.3 Example of Gamma-ray Logs after Splicing.

4.3.4 Sandstone Reservoir Determination

The gamma-ray log identified four potential sandstone reservoirs from each well. Through log curve observations, it is generally accepted that the minimal deflection to the left denotes clean sandstone, whereas the maximum deflection to the right indicates a shale (Figure 4.4).

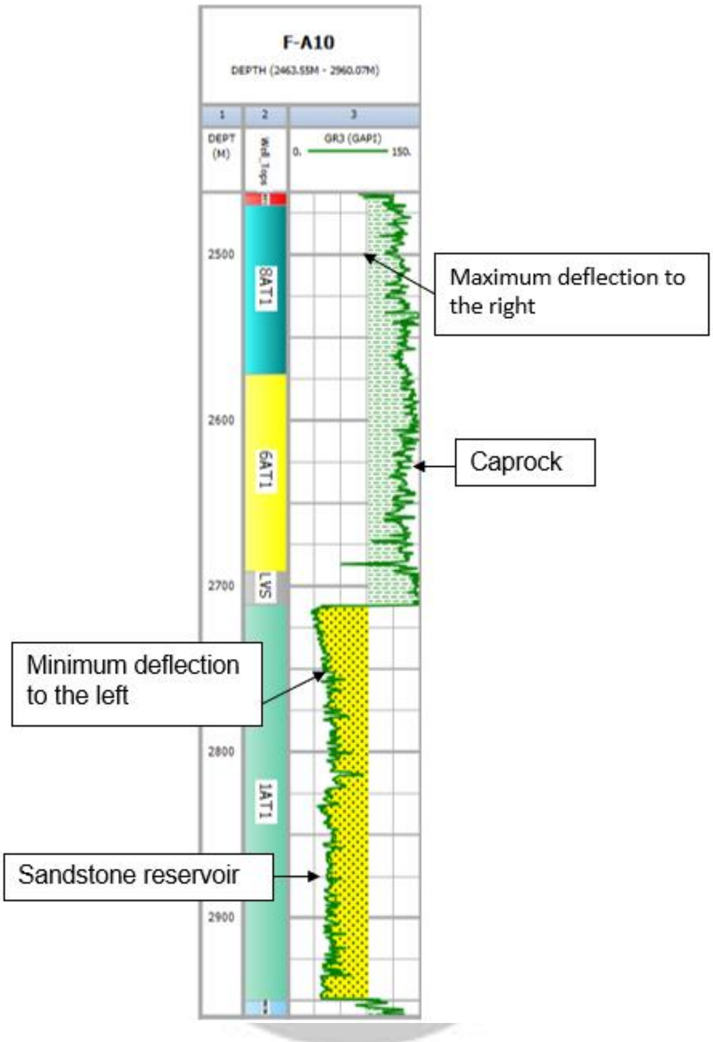

Figure 4.4 Example of an Identified Sandstone Reservoir for well F-A10.

4.3.5 Fluid Saturation Parameters from Standalone Picket Plot

The fluid saturation parameters—m, a, n, and Rw—were found within a water-bearing zone of the studied wells. To establish these parameters, a resistivity versus porosity plot commonly known as a Standalone Pickett Plot was used and is outlined in Appendix B. These characteristics play a significant role in log interpretation and include:

- Tortuosity factor (a)
- Cementation factor (m)
- Water saturation factor (n)
- Water resistivity factor (Rw)

In the cross-plot, the straight lines represent varying levels of water saturation: the red line denotes 100% water saturation, the line at 0.5 indicates 50%, the line at 0.3 represents 30%, and the line at 0.2 corresponds to 20% (Magoba, 2014).

4.3.6 Estimation of Clay Content

The wetted shale content in a unit volume of reservoir rock is called the volume of shale (Vsh). It represents the amount of water chemically bound to the clay minerals in shale (Norman, 1991). Shale, which consists of clay-sized particles with little to no silt, is frequently found in clastic sedimentary rocks (Norman, 1991). Clay minerals are the primary minerals found in shale and comprise most source rocks and sealing structures. Because of its low permeability, clay can act as a caprock or seal that prevents CO_2 from escaping once injected underground.

Since shale is typically more radioactive than sand or carbonate, the amount of shale/clay can be calculated from the gamma-ray curve (Jensen et al., 2013) and presented as a percentage or decimal fraction. The gamma-ray index (IGR), used as an input parameter, must be calculated first to get the volume of shale. The following linear equation is used to determine the gamma-ray index (linear response (V_{shale} = IGR):

$$V_{shale} = IGR = \frac{GR_{log}}{GR_{max}} - \frac{GR_{min}}{GR_{max}} \dots\dots\dots\dots\dots\dots\dots\dots..(2)$$

Where:

V_{shale} = Volume of shale

IGR= A parameter known as the gamma-ray index derived from gamma-ray measurements

GR_{log} = Gamma-ray value recorded for each zone under analysis

GR_{min} = The lowest gamma-ray reading (clean sand)

GR_{max} = The highest gamma-ray reading (shale)

To get the best value that may be used for interpretation, the value of (Vshale) must be corrected using a reliable formula (Jensen et al., 2013). The following formula was chosen to calculate Vsh:

- Steiber (1970): $V_{sh} = \frac{I_{GR}}{3-2\times I_{GR}} \dots\dots\dots\dots\dots\dots\dots\dots\dots\dots\dots\dots\dots\dots\dots\dots\dots\dots\dots (3)$

The Steiber model was selected because it applies to tertiary rocks, and the rocks examined in this study belong to the Lower Cretaceous period of the Mesozoic Era. The minimum and maximum values used in the equation were derived from the gamma-ray multi-well histogram plots, as shown in Figure 4.5.

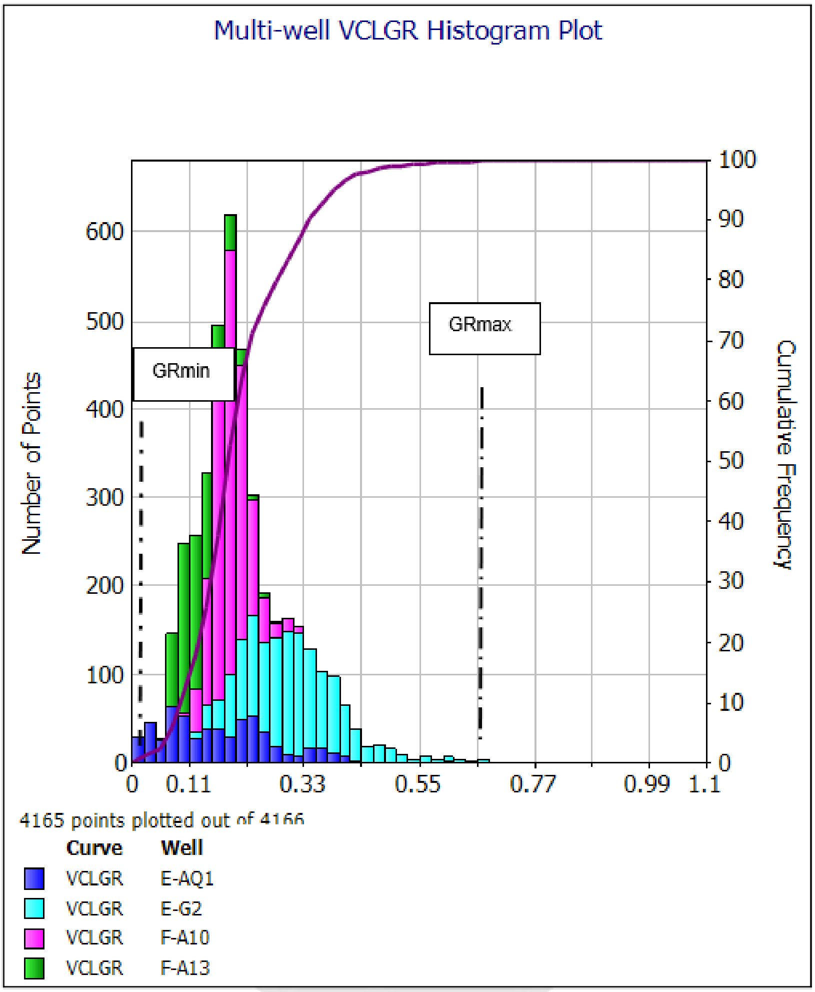

Figure 4.5 Multi-well Volume of Clay Histogram plot.

Table 4.1 Parameters are Used to Calculate the Volume of Clay Within the Reservoirs.

Well name	Top Depth (m)	Bottom Depth (m)	GR_{min} (API)	GR_{max} (API)	GR_{log} (API)
E-AQ1	2535	2622	0.0051	0.6042	0.1673
E-G2	3267.6	3469.4	0.1192	0.7617	0.3073
F-A10	2711.8	2948	0.1058	0.3466	0.1887
F-A13	2610.5	2719.7	0.0566	0.3199	0.1266

4.3.7 Evaluating Porosity Using Wireline Logs

This study used the density log for E-AQ1, E-G2, F-A10, and F-A13. The principles behind the application of these logs are described below:

Density Log-Derived Porosity

Density tools release gamma rays with intermediate energy into the desired rock. These medium energy rays scatter and lose energy as they meet the formation's electrons (Parker, 2014). A similar quantity of electrons per unit volume is produced with every impact. The bulk and electron densities of fluids and formations are generally relative (Crain, 2004; Opuwari, 2010). The electron density of the fluids, which is associated with the formation's porosity, and the rock matrix that constitutes the formation are considered in bulk density measurements. The following formula is utilised to derive the density log curve:

$$\varphi = \frac{P_{ma} - P_b}{P_{ma} - P_f} \dots\dots\dots\dots\dots..(7)$$

Where:

φ = The porosity obtained from density log measurements

P_b = Represents the fluid density of the mud filtrate (g/cc)

P_{ma} = The density of the rock matrix density (g/cc)

P_f = fluid density (g/cc); which is typically assumed to be 1 for salt mud and fresh water

4.3.8 Water Saturation Determination

Water saturation from log curves can be determined using two models: clean sand (shale-free) and shaly sand. This study focuses on shaly-sand reservoirs; therefore, shaly-sand water saturation models were employed to assess water saturation. The two shaly-sand water saturation models used are the Simandoux (equation 9) and the Indonesian (equation 10). The following relationship by Simandoux (1963):

$$Sw = \frac{aRw}{2\varphi^m} - \left(\frac{V_{sh}}{R_{sh}} + \sqrt{\left(\frac{V_{sh}}{R_{sh}}\right)^2 + \frac{4}{F} * R_w * R_t} \right) \dots\dots\dots\dots.(9)$$

Sw = Represents the fraction of pore spaces occupied by water within the reservoir

a = The tortuosity factor which adjusts for the complexity of the pore network

R_w = The resistivity of the water in the reservoir

R_{sh} = The resistivity of shale in the reservoir

V_{sh} = The volume of shale in the reservoir

F = The formation resistivity factor

R_t = The true resistivity of the formation, derived from the corrected deep resistivity log readings

φ = Effective porosity, expressed as a fraction

m = A parameter that describes how pore geometry and rock texture affect the restivity of the rock known as the cementation exponent

$$\frac{1}{\sqrt{R_t}} = \left(\frac{\varphi em}{a * R_w} + \frac{Vcl^{\left(1-\frac{Vcl}{2}\right)}}{\sqrt{R_{cl}}}\right) * \ S_w{}^{\frac{n}{2}} \ldots\ldots\ldots\ldots\ldots\ldots (10)$$

Where:

R_t = The resistivity curve from the deep log reading

R_{cl} = The electrical resistance of clay when fully saturated with water

φe = The fraction of interconnected pores in the rock that can store and transmit fluids.

S_w = The ratio of water-filled pore volume to the total pore volume, given as a fraction

V_{cl} = Volume of shale or clay, expressed as a fraction of the total formation

R_w = Resistivity of the formation water

m =Cementation exponent

a =Tortuosity factor

n = Saturation exponent

4.3.9 Permeability Determination from Core Data

The least expensive approach is to estimate permeability using well-log data and comparing the core and log-derived permeability is essential, as it lets the log-derived curve to be calibrated with in-situ core measurements. This study used the multiple variable regressions method to determine the permeability. The equation was developed from the multi-well cross-plot of porosity vs. permeability usually called a Poroperm cross-plot (Figure 5.5). Figure 1.3 shows that the four wells are nearby hence, the multi-well cross-plot regression equation was used. The following regression equation was used to predict the permeability of the wells:

$$K = 10^{\wedge}(-2.39214 + 26.354 * PhiDen)\ldots\ldots\ldots\ldots\ldots\ldots\ldots (11)$$

Where:

K= Permeability

PhiDen= Porosity

4.3.10 Distribution of Pore Throat Sizes

The sizes and distribution of pore throats significantly influence fluid transportation within reservoirs, affecting key properties such as fluid saturation, porosity, permeability, and even wettability to some degree (Lake, 1989). A high aspect ratio, defined as the relationship between pore-body radius and pore-throat radius, alters the fluid interface, leading to the preferential flow of the wetting phase into the pore throats. This behavior enhances the saturation of the non-wetting phase. As a result, narrower pore throats are considered more effective for CO_2 storage compared to wider ones (Grobe et al., 2009; Pentland et al., 2012).

The variability in pore-throat size distribution plays a serious role in the movement and storage processes of CO_2 (Wei et al., 2014). Despite this, a considerable amount of heterogeneous rocks can still store injected CO_2 effectively, thanks to dispersed flow pathways (Ambrose et al., 2008). One effective measure for identifying well-connected pore throats in rocks with intergranular porosity is the 35-pore-throat radius, which depends on factors such as entry size and pore throat sorting (Hartman & Coalson, 1990). The equation developed by Winland (1972), later published by Kolodzie (1980), is presented below:

$$Log\ (r35) = 0.732\ + 0.588 * \log(K) - 0.864 * \log \varphi \ \ldots\ldots\ldots\ldots\ (12)$$

Where:

r35= pore throat radius in micrometres

K= Permeability in millidarcies

φ= porosity (%).

This study calculated the pore throat size using the Winland equation. The pore throat size can be classified based on the petrophysical rock type (Table 4.2) (Opuwari & Dominick, 2021).

Table 4.2 Classification of Pore Throat Size (Opuwari & Dominick, 2021).

r35(μm)	Pore Radius Threshold	Rock Type	Porosity (%)	Permeability(mD)
>10	1	Megaporous	15-20	100-500
4-10	2	Macroporous	10-15	20-100
2-4	3	Mesoporous	5-10	5-20
1-2	4	Microporous	5-10	1-5
<1	5	Nanoporous	<5	<1.0

4.3.11 Storage and Flow Capacity

Storage Capacity is defined as the ability of a rock to store fluids, such as CO_2. Flow Capacity is the ease at which a fluid can flow through a reservoir. To calculate storage capacity, you need to find the product of porosity and thickness (equation 13) (Gunter et al., 1997). For flow capacity, the product of permeability and thickness must be calculated (equation 14).

$$\varphi h = \ \varphi\ \times h \ \ldots\ldots\ldots\ldots\ldots\ (13)$$

$$kh = k \times h \ldots\ldots\ldots\ldots\ldots.. (14)$$

where φ = porosity

h = thickness

k = permeability

These two parameters can provide more understanding of the ability of a reservoir to store and transmit CO_2. To further understand the flow and storage capacity of sedimentary rocks for CO_2 storage efficiency, a storage capacity vs. depth and flow capacity vs. depth graph was constructed using Excel.

4.3.12 3D Visualization Petrophysical Properties Across the Field

The general patterns of petrophysical characteristics in the study area were displayed using a 3-D parameter viewer. Four properties and their averages were the focus of the analysis: clay volume, water saturation, permeability, and porosity. The studied reservoirs were used to evaluate these properties. Interactive Petrophysics was used to display the data and plot it against True Vertical Depth (TVD). The parameter values were distinguished using a legend bar that used a colour scale for clarity. The values for all four reservoirs were presented, each reflecting their respective average reservoir values. They were displayed in the form of figures, from figure 4.29A to figure 4.29D.

4.4 Results and Interpretation

Two different methods were used to interpret the results: qualitative and quantitative.

4.4.1 Conventional Core Analysis Interpretation

This study analysed cored sections from three wells, viz. E-G2, F-A10, and F-A13. The E-AQ1 conventional core analysis report recorded only two values, making it insufficient for consideration. This will not affect the validity of the results because the four wells are in proximity in the study area, so they share similar geological characteristics.

4.4.2 E-AQ1 Interpretation

The core analysis results for E-AQ1 show an excellent poroperm characteristic for the sandstone with porosity ranging from 5 to 18 % porosity and permeability ranging from 130 to 193 mD and more than 90 % water saturation. The conventional core analysis measurements include grain density, porosity, permeability, water saturation, and calcimetry (for calcite and dolomite). The grain density varies from 2.65 to 2.73 g/cc, with a mean of 2.65 g/cc. Sandstone (quartz) is expected to have a grain density of 2.65 g/cc (Table 3.3). There is more calcite than dolomite, which indicates that the dominant cementing agent is calcite. The variation in calcite and dolomite percentages is evidence of a complex diagenetic history. Some reservoir parts may have undergone significant calcite cementation, while others may have experienced dolomitization. Table 4.3 shows the data obtained from the conventional core analysis report for E-AQ1.

Table 4.3 Conventional Core Analysis of Well E-AQ1.

Depth (m)	Porosity (%)	Permeability KL (mD)	Sw (%)	Calcite (%)	Dolomite (%)	Grain density (g/cc)
Core 1						
2502.12	17.3	139.42	93	0.0	4.0	2.66
2502.33	18.2	133.35				2.68
2502.60	18.1	140.08				2.67
2502.76	18.5	194.34	91	1.5	1.0	2.65
2503.05	17.4	118.98				2.66
2503.58	5.4	0.02	71	34.0	6.0	2.72
2512.50	7.6	0.06				2.73
Core 3						
2614.05	0.3	0.03	60	0.0	0.0	2.70
2616.65	2.2	0.06	56	0.0	0.0	2.70

4.4.3 E-G2 Interpretation

The core analysis results gave an average porosity of about 12.00 % with a range of 5.10 to 15.90 % and permeabilities of 0 to 1.1 mD. The data is shown in Table 4.4. The grain density for E-G2 ranges from 2.38 to 2.53 g/cc with a mean value of 2.42 g/cc (Figure 4.6A). Clay minerals are anticipated at the grain density of 2.38g/cc (Table 5.1). The presence of clay likely reduces porosity and permeability due to the pores being blocked and restricted fluid flow. There is more dolomite than calcite, which indicates that the dominant cementing agent is dolomite. The variation in calcite and dolomite percentages is evidence of a complex diagenetic history.

Some parts of the reservoir may have undergone significant dolomite cementation, while others may have experienced a minor amount of calcite cementation. The standard deviation measures how much individual values deviate from the mean. In this case, it is calculated to be 0.04 g/cc. This indicates that the grain density ranges from a minimum of 2.38 g/cc to a maximum of 2.53 g/cc. The core porosity also span from 0.05 to 0.15 % (Figure 4.6B). The average porosity of the samples is 12.20 %, with a standard deviation of 2.88 %.

The porosity histogram reveals two distinct zones (Figure 4.6A). One zone displays 5 and 10.00 % porosity, which corresponds to silt. The second zone shows values ranging from 10.00 to 16.00 %, indicating the presence of massive, clean sandstone. This average porosity of 12.20 % suggests a relatively favourable condition for CO_2 storage. Core permeability ranges from 0.10 to 0.90 mD, with an average permeability of 0.32 mD, as illustrated in Figure 4.6C. The standard deviation for permeability is 0.26, categorising the average permeability as poor (Table 3.6). In the E-G2 reservoir, core water saturation ranges from 19.00 to 71.00 %, with an average saturation of 34.27 % (Figure 4.6D) and a standard deviation of 14.22 %.

Table 4.4 Results Obtained from the Conventional Core Analysis of Well E-G2.

Depth (m)	Porosity (%)	Permeability (KL) mD	Sw (%)	Calcite (%)	Dolomite (%)	Grain density (g/cc)
Core 1						
3308.35	0.15	0.1	21	1	1	2.46
3308.86	0.01	0	54	0	2	2.47
3309.48	0.15	0.9	33	1	2	2.39
3310.3	0.13	0.4	28	0	1	2.40
3311.27	0.13	0.1	40	0	2	2.39
3312.04	0.12	0.3	33	1	2	2.42
3313.35	0.11	0.1	24	0	2	2.41
3314.35	0.12	0.4	20	0	2	2.40
3315.23	0.09	0	45	0	1	2.45
3317.33	0.11	0.1	19	0	1	2.47
3318.22	0.15	0.5	24	0	2	2.39
3319.27	0.12	0.6	36	0	2	2.38
3320.06	0.09	0	39	0	1	2.48
3321.65	0.13	0.1	27	0	2	2.39
3323.48	0.05	0	71	0	0	2.53

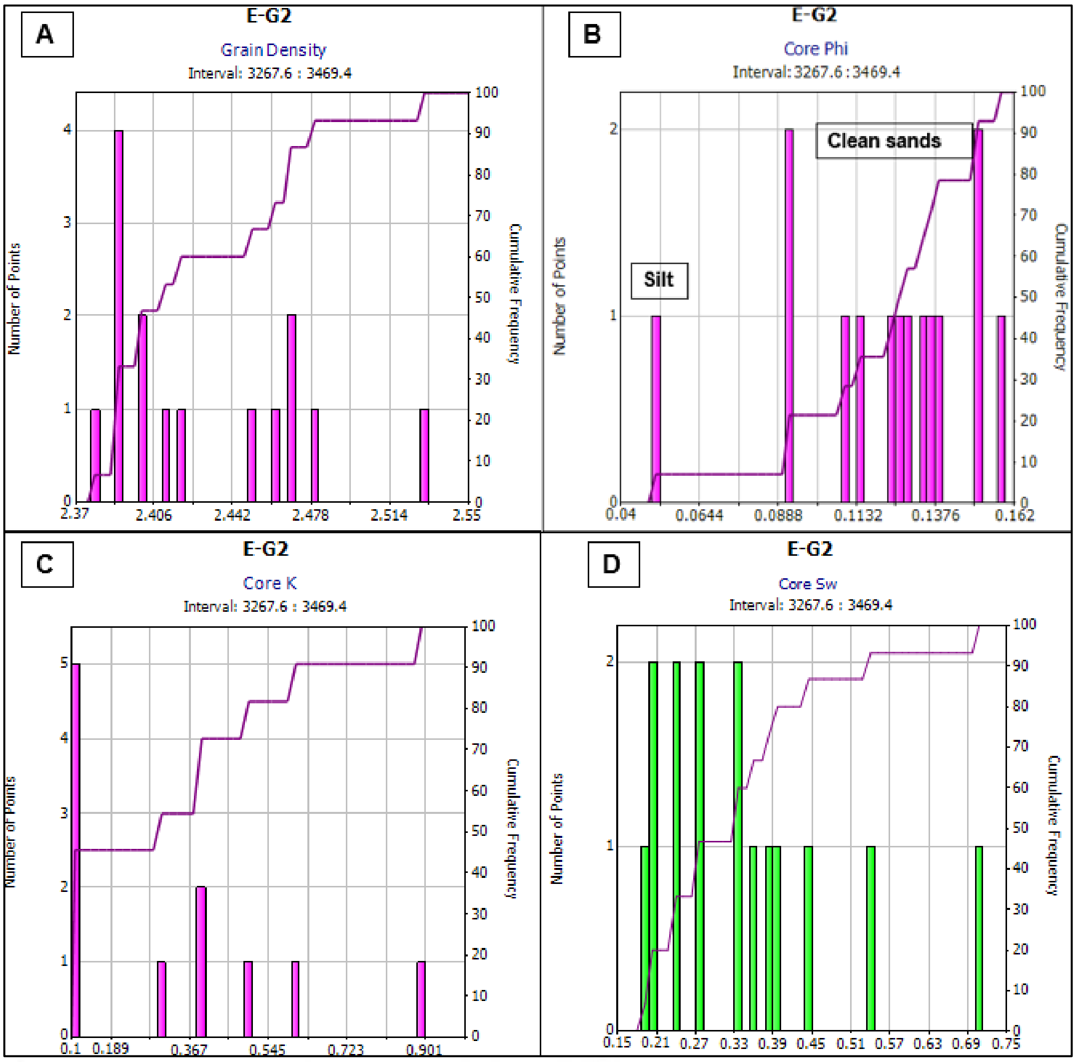

Figure 4.6 Core Histograms for E-G2. (A) Grain Density (B) Core Porosity (C) Core Permeability (D) Core Water Saturation.

4.4.4 F-A10 Interpretation

The porosity ranges from 5.8 to 19.7 %, and the permeability ranges from 0.26 to 924.00 mD. The results are shown in Table 4.7 in appendix A. The sum for calcite is 56, and the sum for dolomite is 100, which means there is more dolomite than calcite, indicating that the dominant cementing agent is dolomite. The variation in calcite and dolomite percentages is evidence of a complex diagenetic history. Some parts of the reservoir may have undergone significant dolomite cementation, while others may have experienced a minor amount of calcite cementation.

In the F-A10, core porosity varies from 5.80 % to 19.70 %, with an average of 14.12 % and a standard deviation of 3.40 %. The porosity histogram reveals two distinct zones (Figure 4.7A). The first zone displays porosity ranging from 5.00 to 10.00 %, indicative of silt, while the second zone shows values between 10.00 and 16.00 %, comprising massive clean sandstone. The average porosity of 14.12 % suggests a relatively favourable condition for CO_2 storage. Core water saturation ranges from 0.11 to 0.80 %, with an average of 0.45 % (Figure 4.7B) and a standard deviation of 0.14 %. The core permeability fluctuates between 0.18 and 924.00 mD, yielding an average of 34.55 mD with a standard deviation of 44.08 mD (Figure 4.7C). This average permeability can be classified as moderate (Table 3.6).

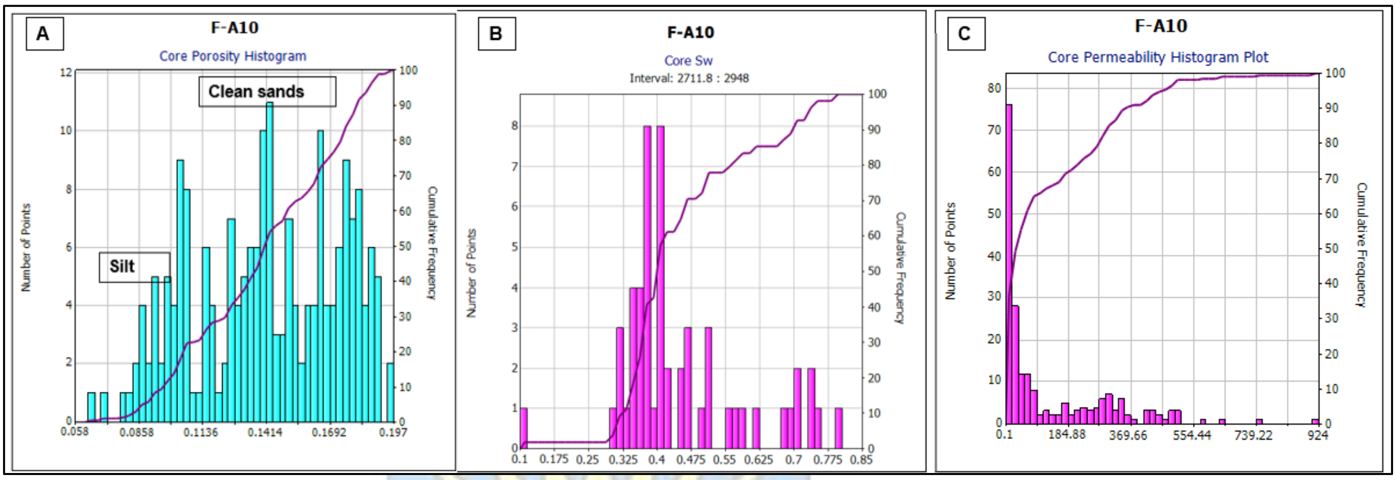

Figure 4.7 Core Histograms for F-A10. (A) Core Porosity (B) Core Water Saturation (C) Core Permeability.

4.4.5 F-A13 Interpretation

The sandstone shows a range of porosities from 3.8 to 22.3 %, with an average of 16 %. The range of permeabilities is 10 to 1600 mD, with an average of approximately 200 mD. The porosities and permeabilities decrease downwards as the sandstones become calcareous and fossiliferous. The last 10 m has an average porosity of 9 % with an average permeability of 0.3 mD. The core analysis results are shown in TABLE 4.8 Appendix A. The grain density of F-A13 varies between 2.67 and 2.79 g/cc, with an average value of 2.6989 g/cc (Figure 4.8A). The standard deviation is 0.025 g/cc.

Consequently, the grain density predominantly falls within the range of 2.67 to 2.72 g/cc. The core porosity varies from 3.80 to 23.10 %, with a standard deviation of 0.04, and an average porosity is 15.00 %. Three distinct porosity zones were displayed by the porosity histogram (Figure 4.8B). One zone, which was composed of clay and shale, had a porosity of less than 4%. The second zone, which is silt, had a porosity ranging between 5 and 10 %.

The third zone, which was composed of large, clean sandstone, had a porosity ranging from 10 to 16 %. A good porosity that is suitable for CO_2 storage is demonstrated by the average porosity of 15.3 %. The average core water saturation is 0.37 %, with values from 0.23 to 0.75 % (Figure 4.8C). The standard deviation is 0.0707 %. The mean core permeability is 245.0519 mD, with values ranging from 0.03 to 2190 mD (Figure 4.8D). According to Table 3.6, the average permeability is categorised as good.

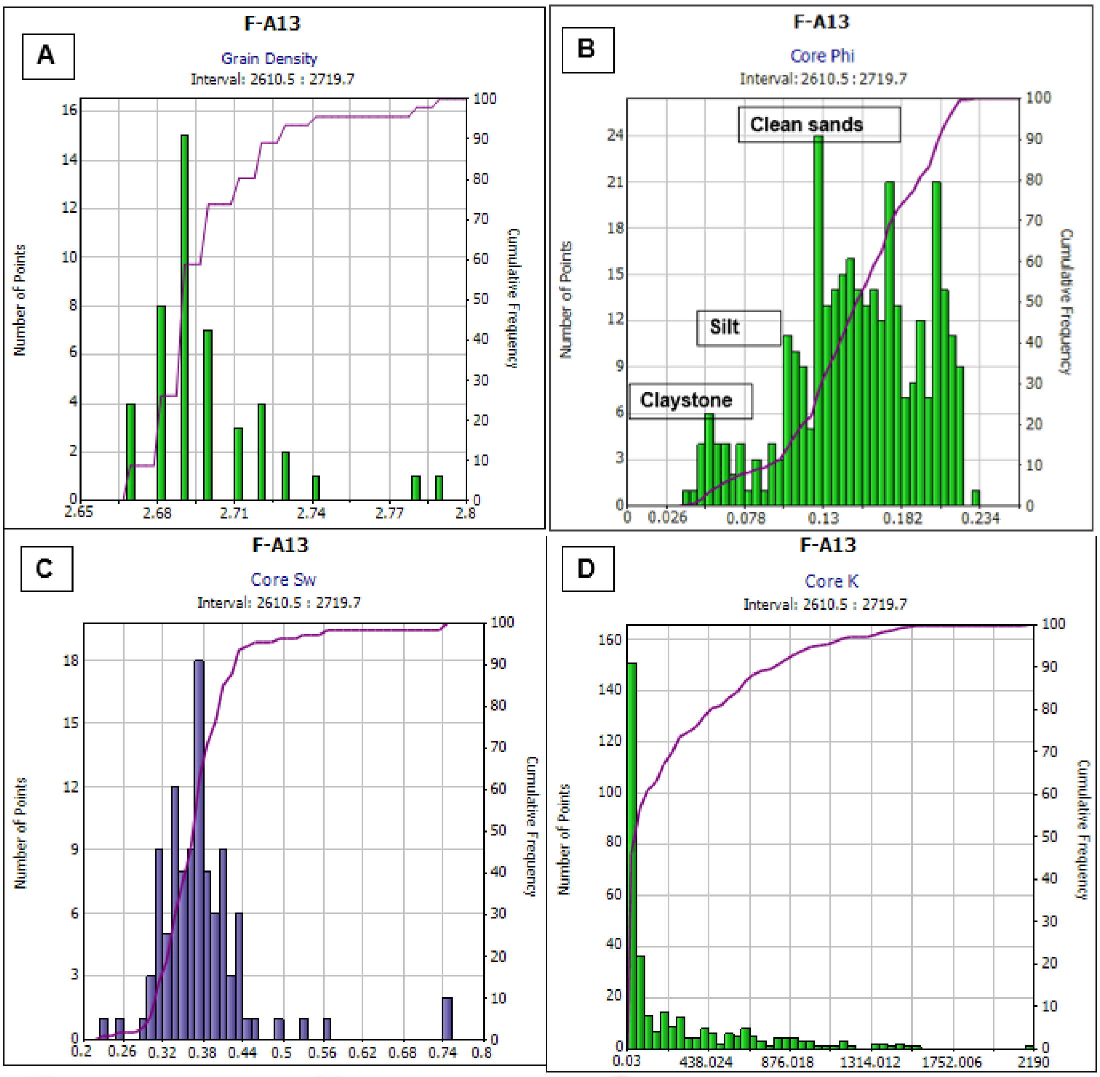

Figure 4.8 Core Histograms for F-A13. (A) Grain Density (B) Core Porosity (C) Core Water Saturation (D) Core Permeability.

4.4.6 Multi-well Core Histograms

With a mean of 2.56 g/cc and a standard deviation of 0.02 g/cc, the grain density in multi-well core histogram displayed a range of values from 2.42 to 2.69 g/cc (Figure 4.9A). Apart from E–G2, carbonate minerals (calcite and dolomite) were present in all cored intervals in relatively small amounts and at a few depths. Carbonate cement is present throughout the cored interval in E-G2. F-A13 had the greatest mean value, 2.69 g/cc, while E-G2 had the lowest, 2.42 g/cc. The porosity multi-well histogram shows F-A13 and F-A10 as the wells with the highest porosities (Figure 4.9B).

E-G2 recorded the lowest porosity of 12.20 %. The greater the porosity of a reservoir, the more pore space there is to store CO_2. Therefore, E-G2 has less pore space to store CO_2 than F-A10 and F-A13. The multi-well core water saturation histogram shows that F-A10 has more water saturation than E-G2 and F-A13 (Figure 4.9C). Lower water saturation allows for a more significant fraction of the pore space for CO_2, increasing storage capacity. High water saturation increases capillary pressure, making it more challenging to inject CO_2. The core permeability multi-well histograms show that E-G2 has the lowest permeability of 0.32 mD (Figure 4.9D).

Low-permeability reservoirs can act as effective caprocks or seals, trapping CO_2 within the storage reservoir and minimising the risk of CO_2 leakage. F-A10 and F-A13 have the highest permeabilities of 34.55 and 245.05 mD. The values greater than a 100 mD at a depth of 800 m or above satisfy the requirements for CO_2 storage (Chabangu et al., 2014). High-permeability reservoirs are more porous and have a remarkable ability to transmit fluids. This allows for easy injection and withdrawal of CO_2, making it suitable for CO_2 storage projects that require efficient and rapid injection or monitoring.

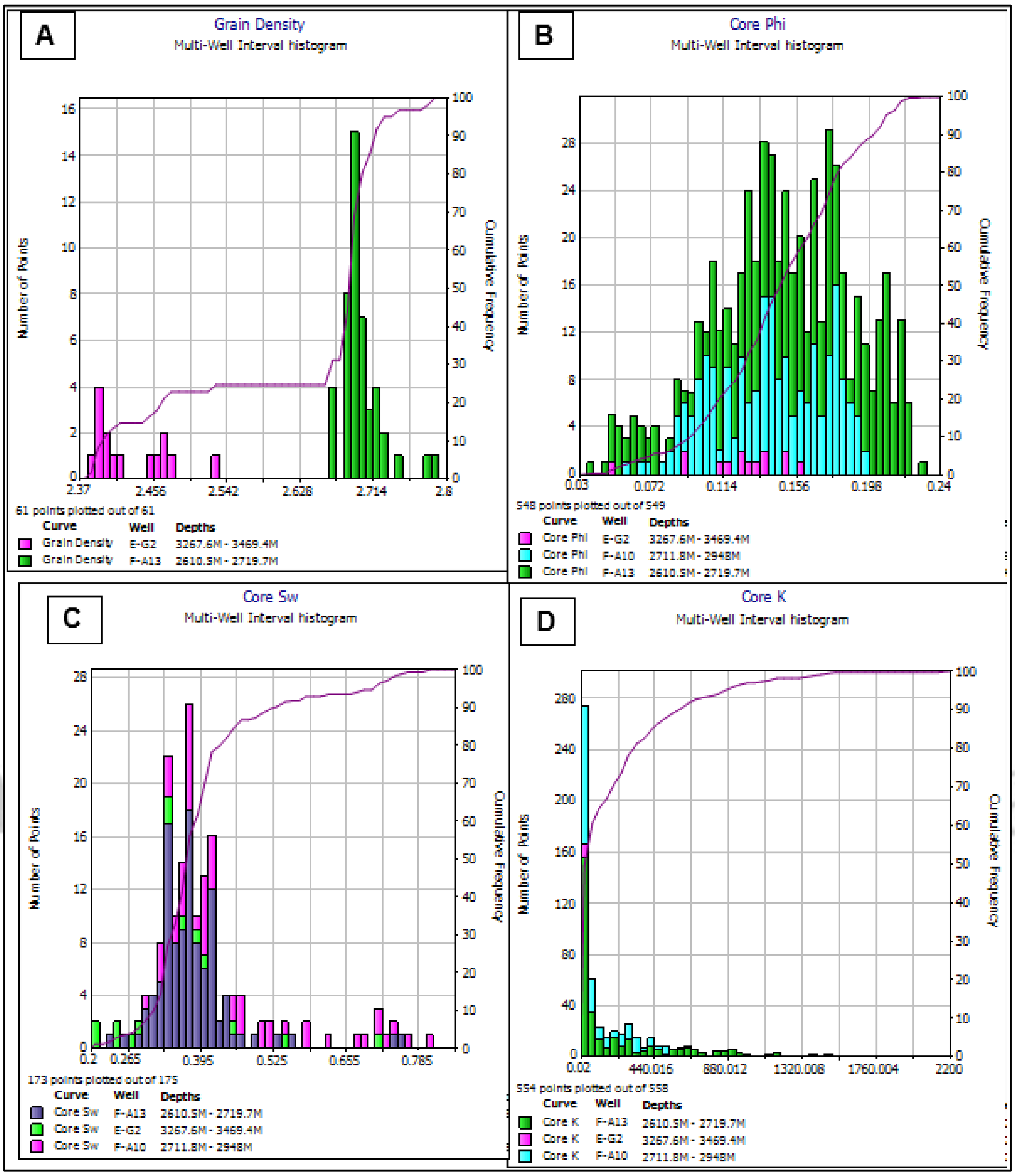

Figure 4.9 Multi-well Core Histograms. (A) Grain Density (B) Core Porosity (C) Core Water Saturation (D) Core Permeability.

4.4.7 Porosity-Permeability Relationship

The various scatter plots for E-G2, F-A10, and F-A13 are displayed in Figures 4.10–4.12. Due to the scattered nature of the data for E-G2 and the absence of a clear trend, it was challenging to define its behaviour accurately. This indicates that there were other factors affecting permeability besides porosity. According to Table 3.3, these elements can be calcite (carbonate cement) and dolomite. The low correlation between porosity and permeability is indicated by the regression value of 0.18 (Figure 4.10). The regression value for F-A10 is 0.95. The trend data is visible, as shown in Figure 4.11. The regression value for F-A13 is 0.88, this suggests that porosity was the primary factor controlling permeability. The data trend is visible, as shown in Figure 4.12.

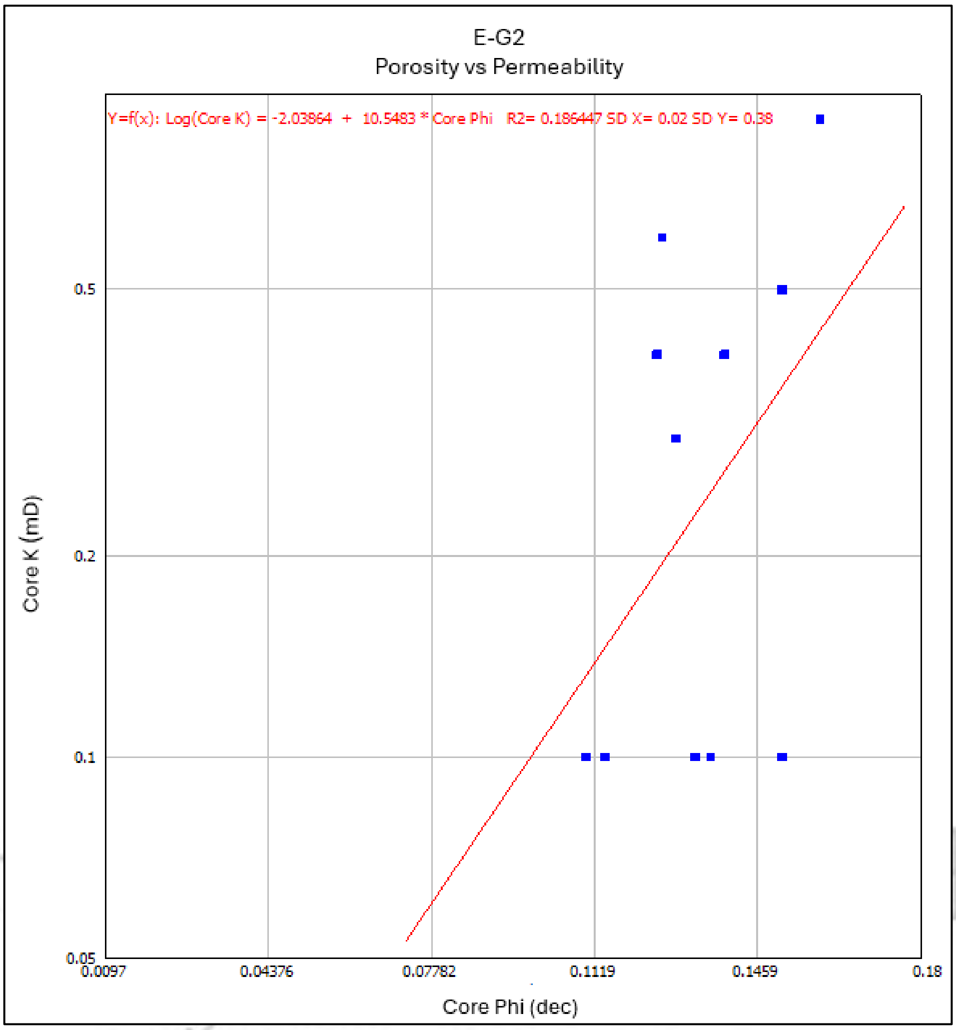

Figure 4.10 Poroperm Plot for E-G2.

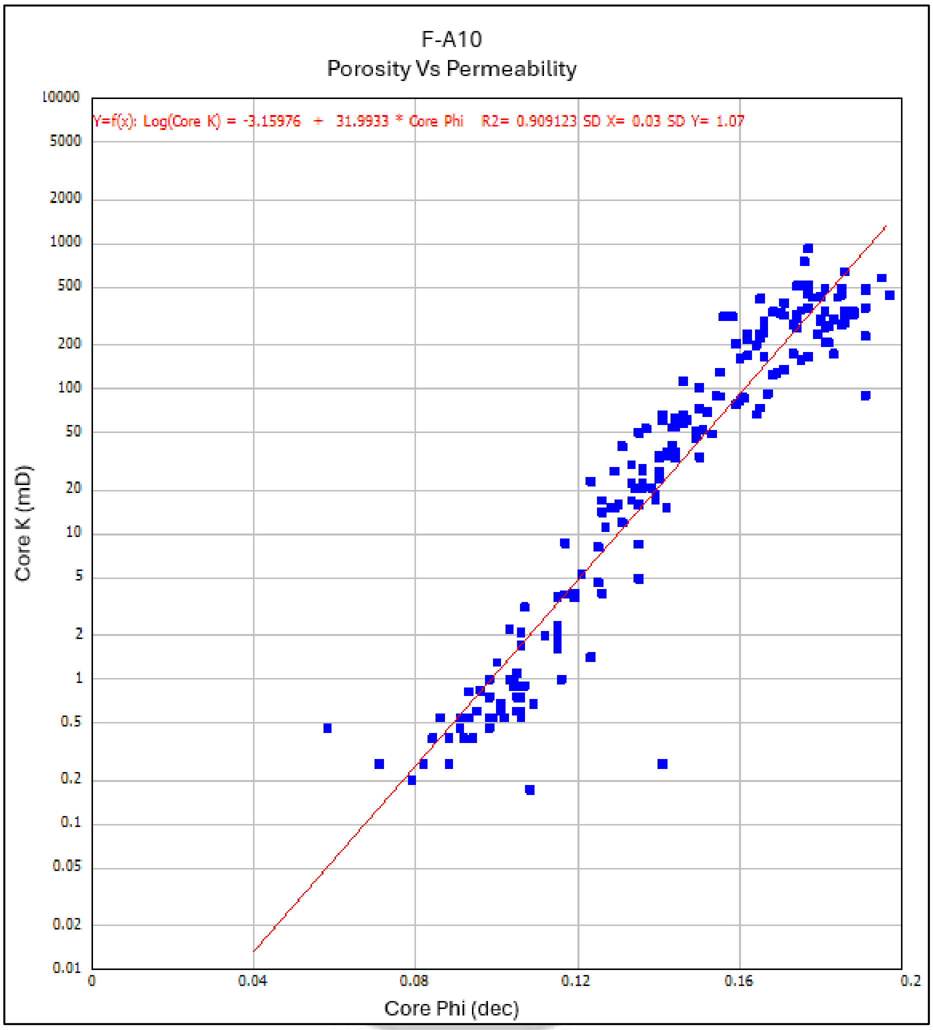

Figure 4.11 Poroperm Plot for F-A10.

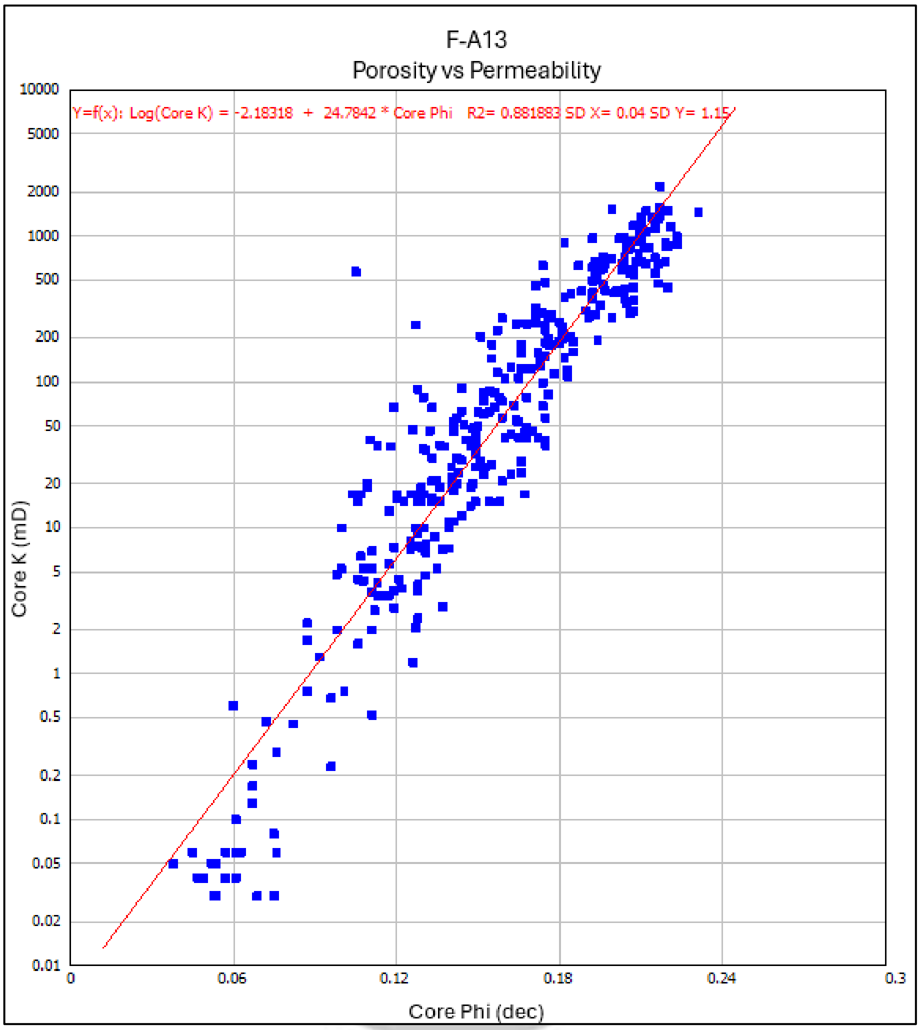

Figure 4.12 Poroperm Plot for F-A13.

4.4.8 Qualitative Interpretation of Wireline Logs

Wireline log curves were interpreted using a qualitative methodology. When investigating geological formations for carbon dioxide storage, different wireline logs are essential to evaluate the subsurface conditions, reservoir properties, and potential for safe and effective CO_2 storage. These logs are:

- Resistivity (LLD): Helps determine the porosity of the rock and evaluate the presence of fluids like water.
- Sonic (DT): Measures the velocity of the sound waves through the rock, helping to estimate porosity.
- Bulk density (RHOB): Gives information on the bulk density of the rock, which can be used to estimate porosity and evaluate whether a reservoir is suitable for CO_2 storage.
- Gamma ray (GR): Used to identify lithology of the different rock types, helping in the assessment of reservoir and cap rock layers.
- Neutron porosity (NPHI): Used in conjunction with the density log to help estimate porosity and assess the fluid content of the reservoir.

By differentiating between sandstone and shale and recognising rocks that are reservoirs and those that are not, the wireline logs offer substantial information on lithology. Potential sandstone reservoirs are defined as sandstone layers that are 50 m or more in depth and surrounded on both sides by a non-reservoir rock (shale). Log data from four reservoirs (E-AQ1, E-G2, F-A10 and F-A13) were examined for this investigation. The interpretation below of the wireline logs used for the reservoirs refers to figure 4.13 to 4.16. They were interpreted based on the description of the different logs written above.

The sandstone reservoirs (1AT1 formation) were identified using well formation tops and gamma-ray log curves. Sandstones have a low gamma-ray log value, while shales have a high one. This difference is due to the presence of radioactive minerals such uranium, thorium, and potassium which occur mostly in shales, hence the high gamma-ray log value. When a gamma-ray log curve bends to the left it indicates a sandstone and when it bends to the right it indicates clay/shale. In the reservoir, the deep resistivity log (LLD) is the one that often deflects to the right as compared to the shallow resistivity log (LLS).

Deflection to the right indicates that the resistivity is high. High resistivity is associated with less presence of fluids, in this case less water saturation. Water saturation plays a role in CO_2 storage because it limits the available pore space available for other fluids (CO_2). Less water saturation means that there is pore space available for CO_2 storage. The density log (RHOB) in the reservoir has a low density (deflection to the right), a low density means that the rocks are less dense making them more porous. In neutron porosity logs (NPHI), a deflection to the right indicates a higher porosity. This means that there is enough pore space.

The time it takes for the sound waves to move through the formation is measured by the sonic log (DT). The sonic readings are low in pore spaces and high in tightly packed formations with few or no pore spaces. When the wave deflects to the right, it indicates an increase in the sound wave traveling through the reservoir. This suggests that the reservoir is denser and less porous.

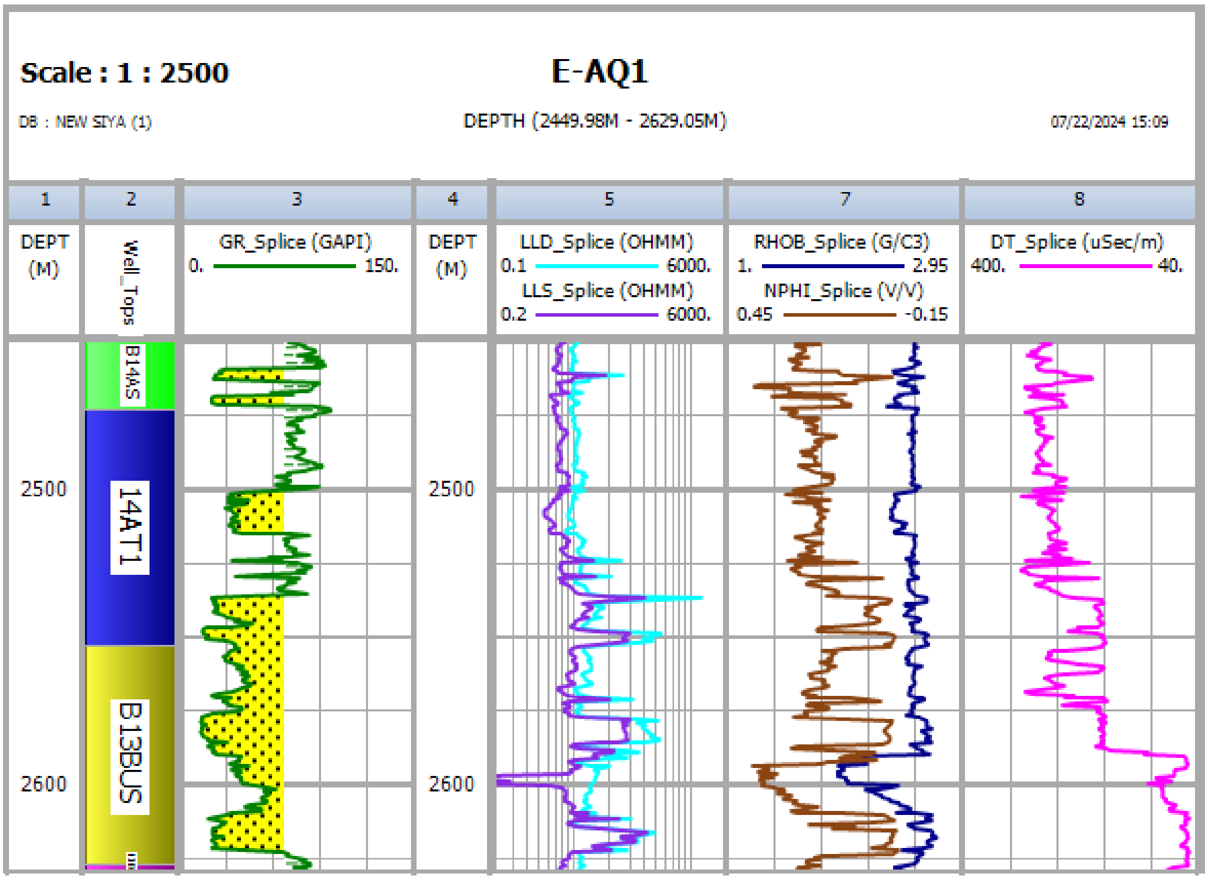

Figure 4.13 Petrophysical Log Analysis of a Sandstone (2535-2622 m), a 14AT1-B13BUS formation of E-AQ1.

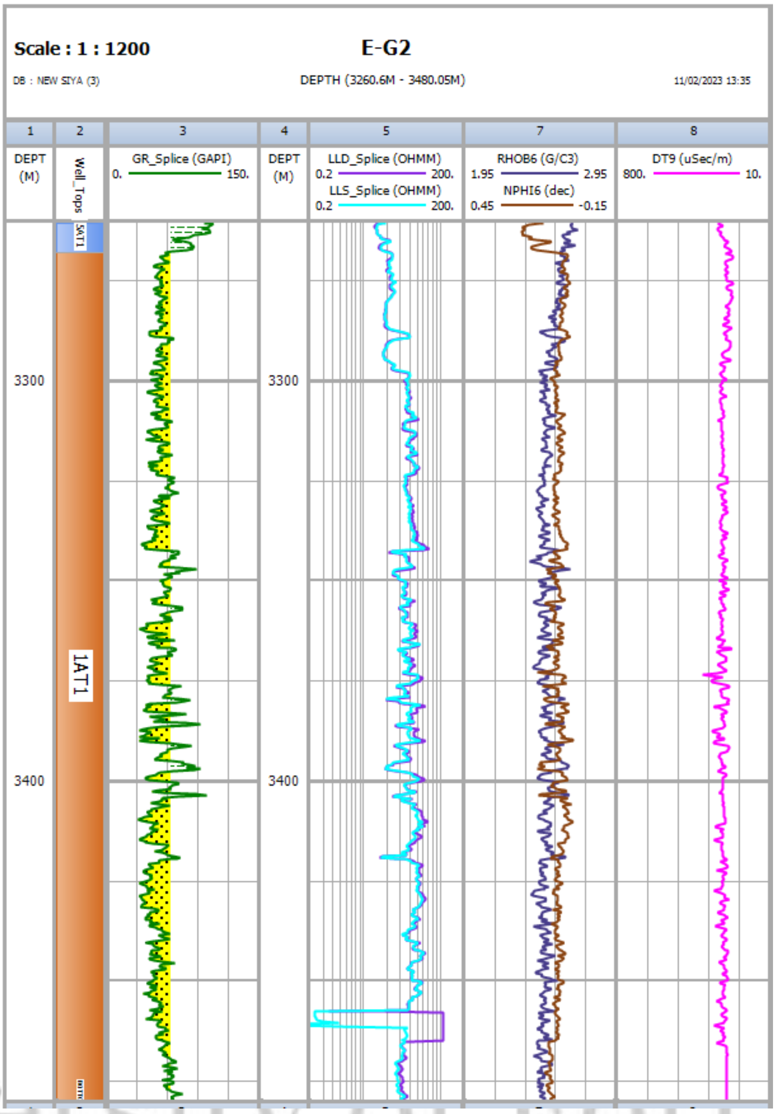

Figure 4.14 Petrophysical Log Analysis of a Sandstone (3267.6 – 3469.4 m), a 1AT1 formation of E-G2.

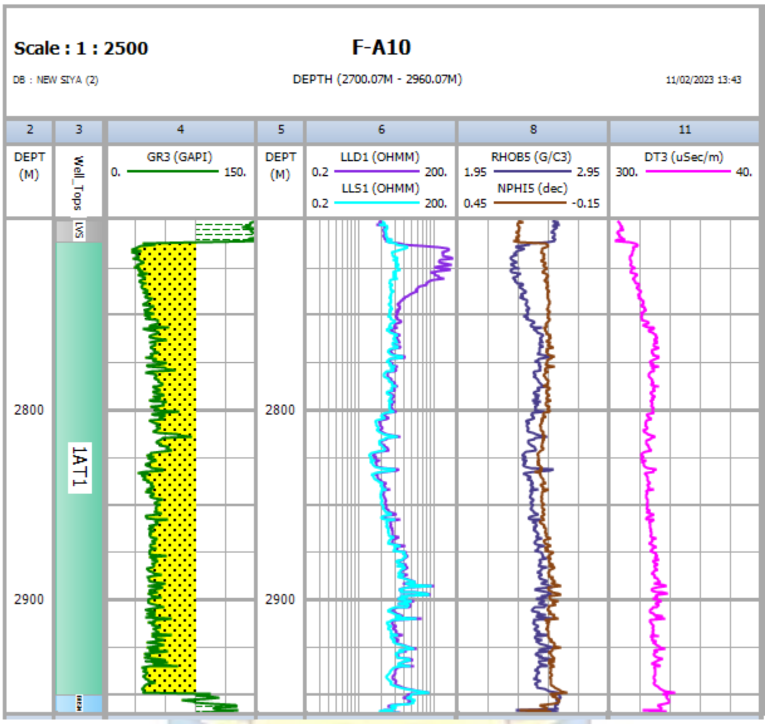

Figure 4.15 Petrophysical Log Analysis of a Sandstone (2711.8 - 2948 m), a 1AT1 Formation of F-A10.

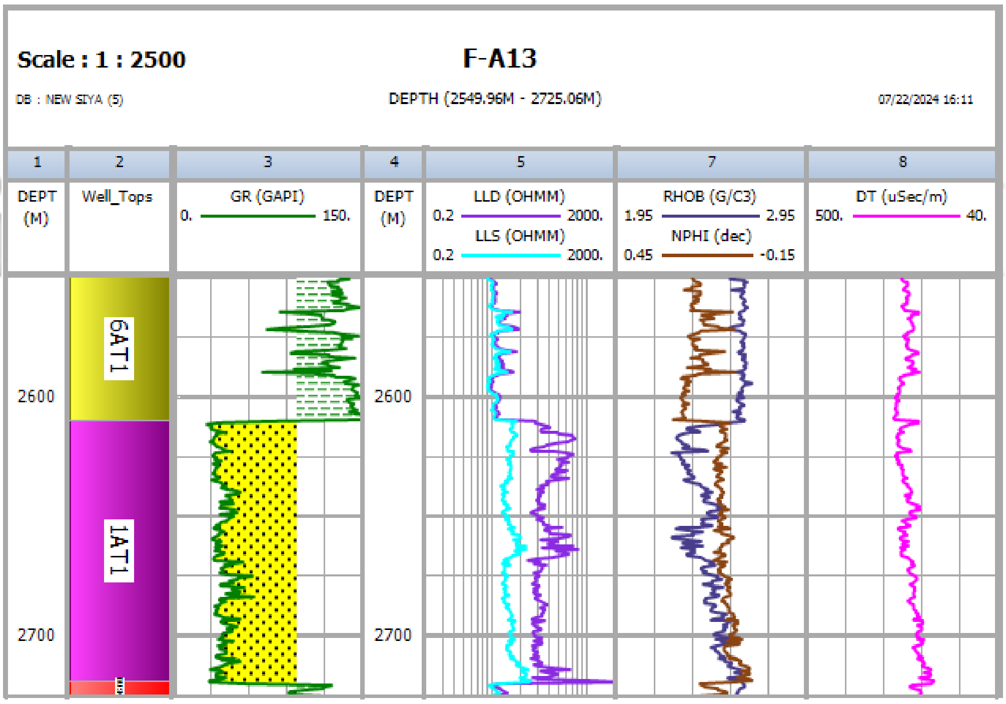

Figure 4.16 Petrophysical Log Analysis of a Sandstone (2610.5 – 2719.7 m), a 1AT1 Formation of F-A13.

4.5 Quantitative Interpretation

The results of each well's chosen reservoirs were analysed using a quantitative method. Table 4.5 displays the calculated petrophysical properties for reservoirs.

4.5.1 Initial fluid Saturation

Determining the initial fluid saturation is essential for the petrophysical evaluation of sandstone reservoirs. These parameters significantly influence the petrophysical results, as they serve as input for the empirical formulas used to calculate reservoir properties like water saturation and porosity.

4.5.1.1 Water Saturation Exponent (n)

The water saturation exponent is determined based on the formation's wettability and the pore framework's geometry. Although this exponent can vary depending on the formation, it is commonly accepted to be around 2. An inaccurate estimation of this exponent can lead to significant errors in the approximation of water saturation, as noted by Bennion et al., (1996). Due to the difference in the "n" values being based on lithology and wettability, it is common practice to use samples that represent a range of porosity, permeability and lithology present in the formation for measuring the "n" value. For this study, the saturation exponent for each of the reservoirs was obtained from the Standalone Pickett plots (Appendix B), where porosity is plotted against resistivity.

4.5.1.2 Tortuosity factor (a)

In certain lithologies, tortuosity is experimentally derived across various porosity values (Bennion et al., 1996). The Archie constant is affected by the degree of consolidation, in general, the tortuosity constant decreases with decreasing consolidation degree. According to Bennion et al., (1996), this constant can vary from 1 for well-consolidated sands to 0.62 for weakly consolidated sands. The sands in all four wells are compacted and consolidated, as indicated by the tortuosity constant value of 1 in this study (Table 4.6), which was obtained from the Standalone Pickett plots (Appendix B).

4.5.1.3 Cementation exponent (m)

The type and extent of cementation inside the pore system affect the cementation exponent's value. Although the degree of cementation influences how this factor may differ, 2.0 is a frequently used value (Bennion et al., 1996). A strongly cemented or oolitic rock may have an "m" value as high as 3.0, whereas a poorly cemented rock may have one that is less than 2.0. The m values for the wells is shown below in Table 4.6. E-AQ1, E-G2, and F-A13 have values that are less than 2. F-A10 is the only well with a value that is greater than 2. The degree of cementation in F-A10 is moderate.

4.5.1.4 Formation water resistivity

The resistivity of formation water is crucial for evaluating initial water saturation, as it is affected by the ionic content of the water. The type of water found in the reservoir is dependent on this property. For example, freshwater has a high resistivity, whereas saline water or brine has a low one. Water resistivity (Rw) was determined using the Standalone Pickett plot. The results for water resistivity are shown in Table 4.5.

Table 4.5 Basic Log Analysis Parameters Calculated from the Standalone Pickett Plots.

Well name	Top Depth (m)	Bottom Depth (m)	Rw	m	N	a
E-AQ1	2535	2622	0.12	1.47	2	1
E-G2	3267.6	3469.4	0.0999	1.55	2	1
F-A10	2711.8	2948	0.0927	2.11	2	1
F-A13	2610.5	2719.7	0.0119	1.47	2	1

4.6 Quantitative Results

4.6.1 E-AQ1 Quantitative Results

The E-AQ1 reservoir measures 2535 to 2622 m and has a total thickness of 87 m (Figure 4.17). The reservoir is classified as a shaly sand based on its average clay volume of 16.73 %. The average water saturation is 52.72 %. Furthermore, the average porosity and permeability are 13.52 % and 11.21 mD, respectively. These values show that the reservoir is appropriate for CO_2 storage.

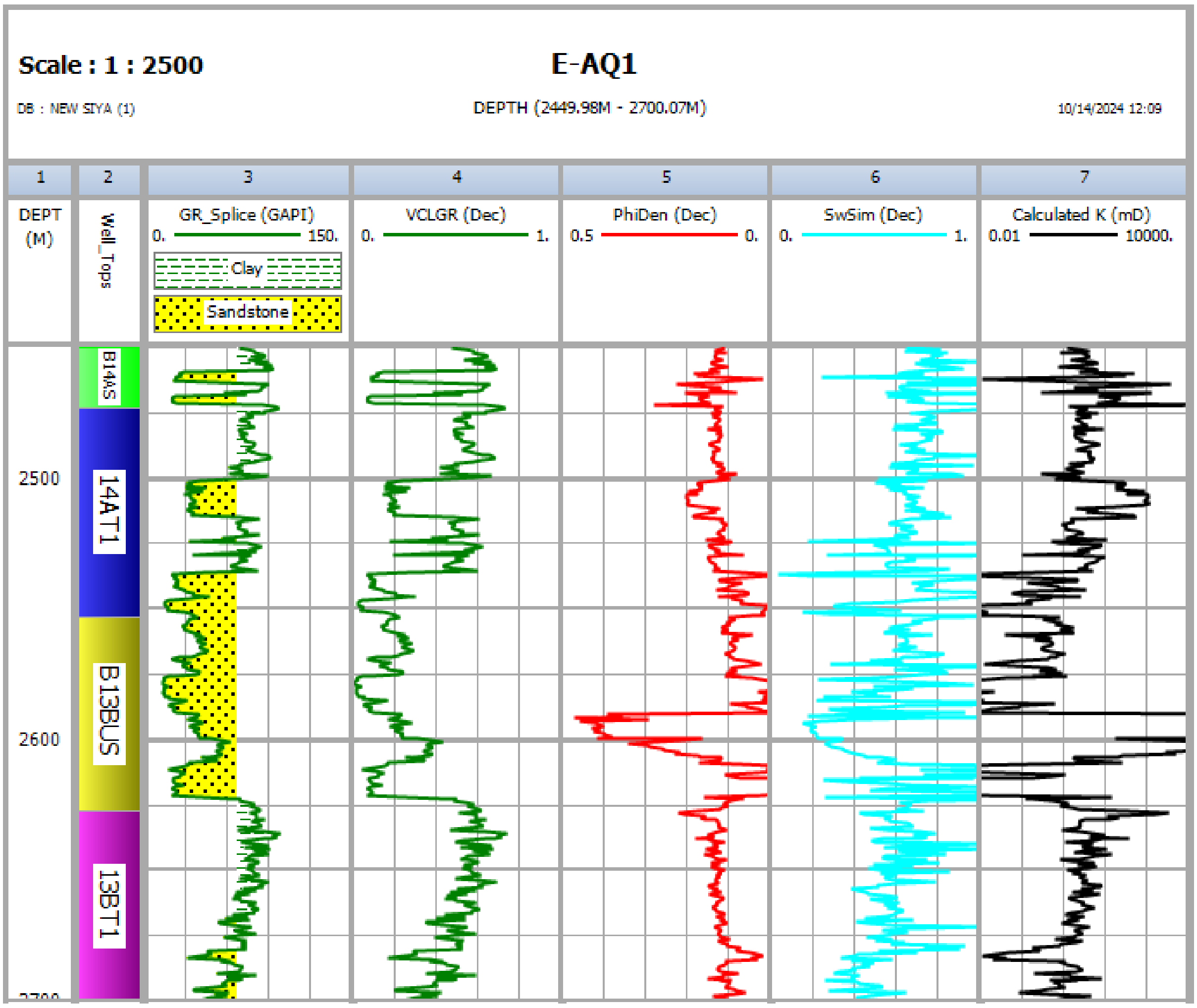

Figure 4.17 Calculated Reservoir Results of E-AQ1.

4.6.2 E-G2 Quantitative Results

The E-G2 reservoir measured between 3267.6 - 3469.4 m and with a total thickness of 201.8 m. An average clay volume of 30.7 % suggests that the reservoir is composed of shaly sand. The reservoir showed an average water saturation of 33.5 %. Core and log water saturation were calibrated and showed good calibration. Similarly, core porosity was calibrated using log-derived findings and exhibited good calibration (Figure 4.18). Core and log permeability were calibrated, although there was a weak correlation between the two values.

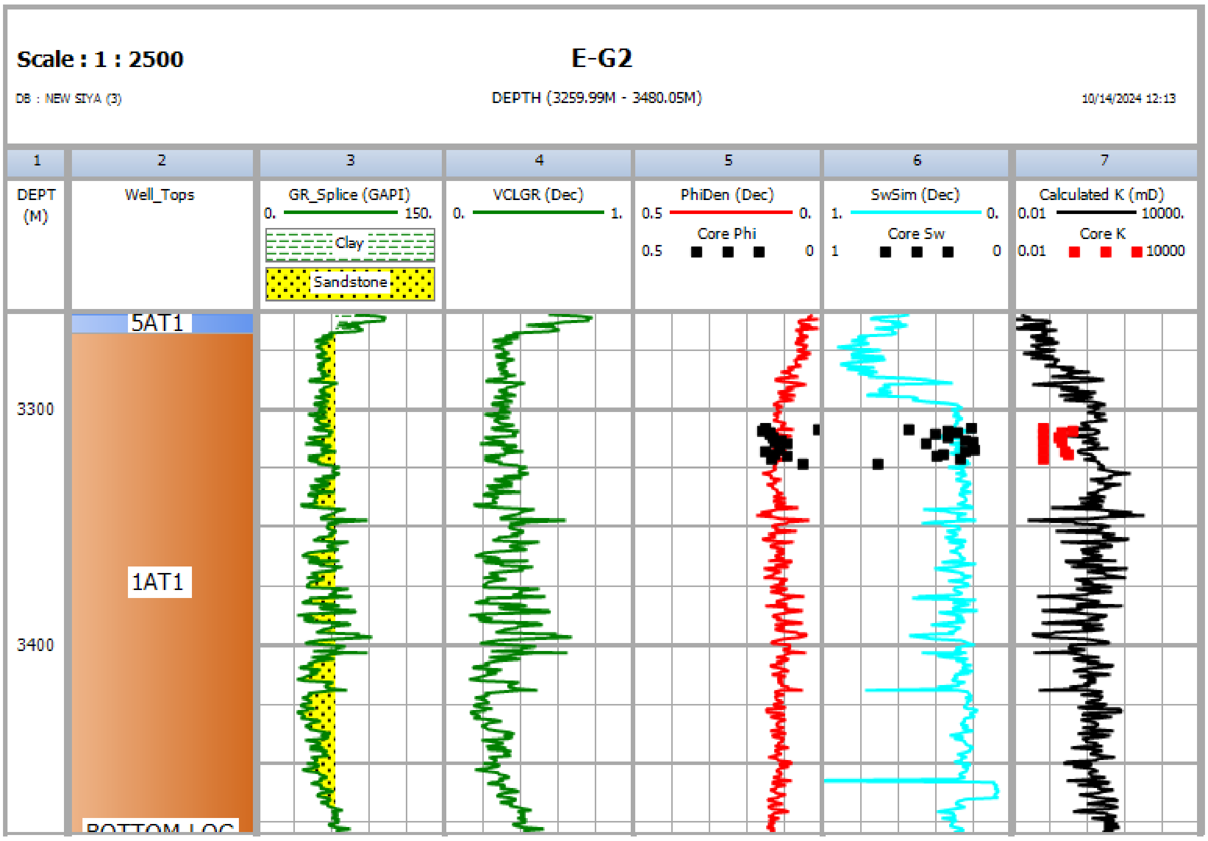

Figure 4.18 Calculated Reservoir Results of E-G2.

4.6.3 F-A10 Quantitative Results

The F-A10 reservoir has a gross thickness of 236.2 m and ranges from 2711.8 to 2948 m. The reservoir is categorised as a shaly sand because of its average clay volume of 18.87 %. The water saturation level is 68.88 % on average. There is a strong correlation between core and log porosity, as shown by their calibration (Figure 4.19). In the same way, there is good consistency in the calibration of core and log water saturation. Additionally, a reliable correlation between the two datasets has been demonstrated by the calibration of core and log permeability.

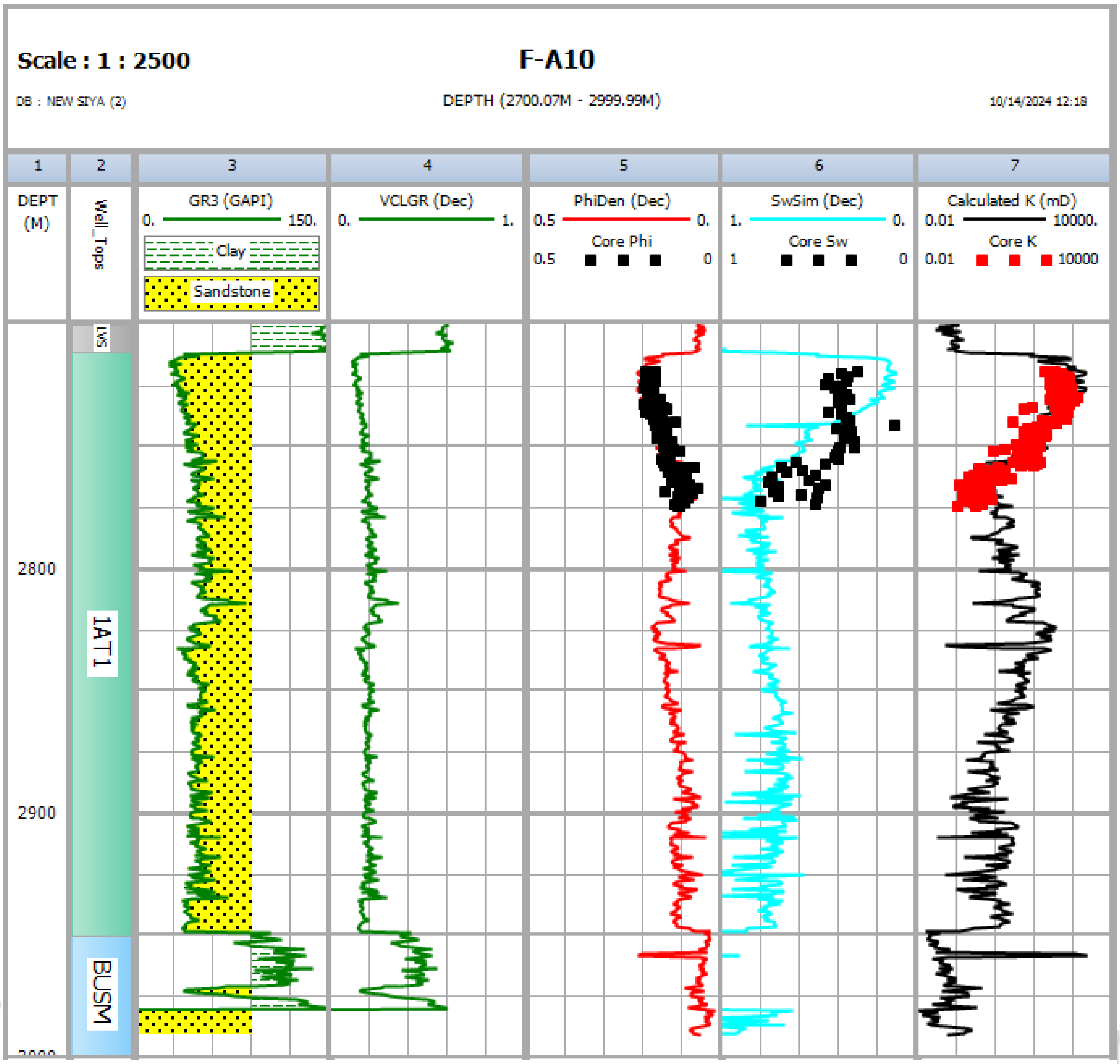

Figure 4.19 Calculated Reservoir Results of F-A10.

4.6.4 F-A13 Quantitative Results

The F-A13 reservoir has a total thickness of 109.2 m and extends from 2610.5 to 2719.7 m. Shaly sand makes up most of the reservoir, as indicated by the average clay volume of 12.66 %. The average water saturation 6.17 %. When core and log porosity were calibrated, a high correlation between the two values was found (Figure 4.20). On the other hand, there was little correlation between the calibration of core and log water saturation.

Since core water saturation is measured at the surface after hydrocarbons have leaked out during the retrieval process, this inconsistency could be caused by problems with core handling and preservation (Magoba et al., 2024). Furthermore, the influence of water-bearing clay minerals, such as smectite, may also affect the measurements, as discussed in Chapter 5. On a positive note, the calibration between core and log permeability yielded a strong correlation between the two sets of measurements.

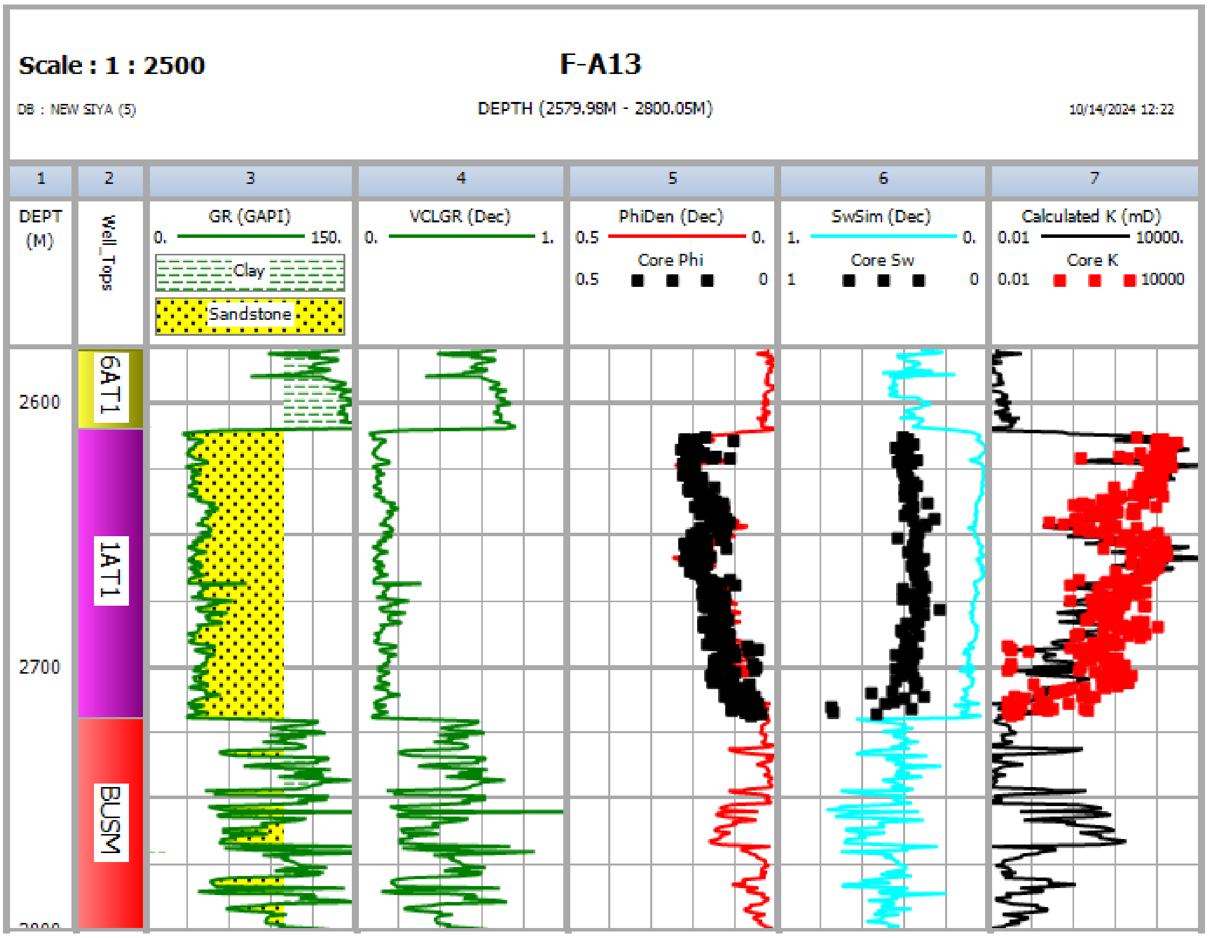

Figure 4.20 Calculated Reservoir Results of F-A13.

Table 4.6 Reservoir Summary Results of all the Studied Wells.

Well name	Zone name	Top (m)	Bottom (m)	Gross (m)	AvPhi (%)	AvSw (%)	AvK(mD)	AvVcl (%)
E-AQ1	14AT1-B13BUS	2535	2622	87	13.52	52.72	11.2115	16.73
E-G2	1AT1	3267.6	3469.4	201.8	9.37	33.52	6.68	30.73
F-A10	1AT1	2711.8	2948	236.2	11.86	68.88	85.57	18.87
F-A13	1AT1	2610.5	2719.7	109.2	13.6	6.17	502.47	12.66

4.7 Pore Throat Size Distribution

4.7.1 Pore Throat Size Distribution for E-G2

The studied reservoir's pore throat radius was less heterogeneous and varied between 0 and 0.46 µm (Figure 4.21). For CO_2, less heterogeneity is advantageous. This implies that when CO_2 is injected into the reservoir, a steady fluid flow will occur.

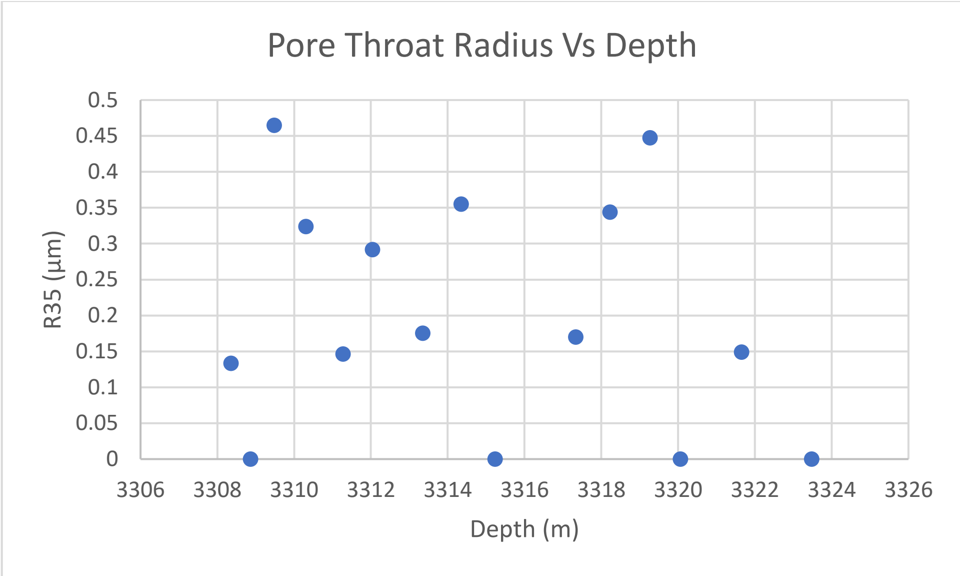

Figure 4.21 Pore Throat Size of E-G2 Reservoir.

4.7.2 Pore Throat Size Distribution for F-A10

In F-A10, the interval 2711.8 – 2948 m shows all pore throat size classes (Figure 4.22). It has a different range of pore throat sizes, which means that it has more heterogeneity. The high heterogeneity will affect the injectivity of CO_2 inside the reservoir, resulting in inconsistent fluid flow because of varying pore throat sizes. The legend in Figure 4.22 shows five different rock types in different colours. The points below a demarcation line represent the rock-type interval. For example, a nanoporous rock type is depicted by a purple line with the associated values (less than 1) under the line.

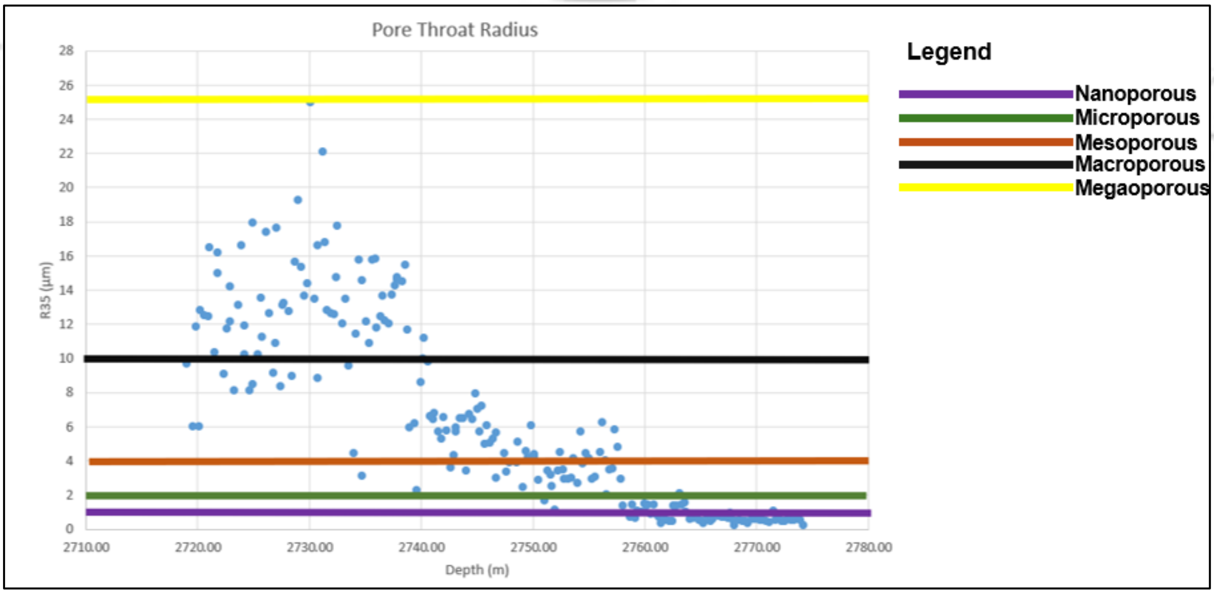

Figure 4.22 Pore Throat Size of F-A10 Reservoir.

4.7.3 Pore Throat Size Distribution for F-A13

F-A13 shows a variety of pore throat sizes (Figure 4.23), indicating a high heterogeneity. High heterogeneity is a cautionary indicator regarding CO_2 injection because it will introduce difficulties regarding fluid flow. The fluid flow will not be uniform.

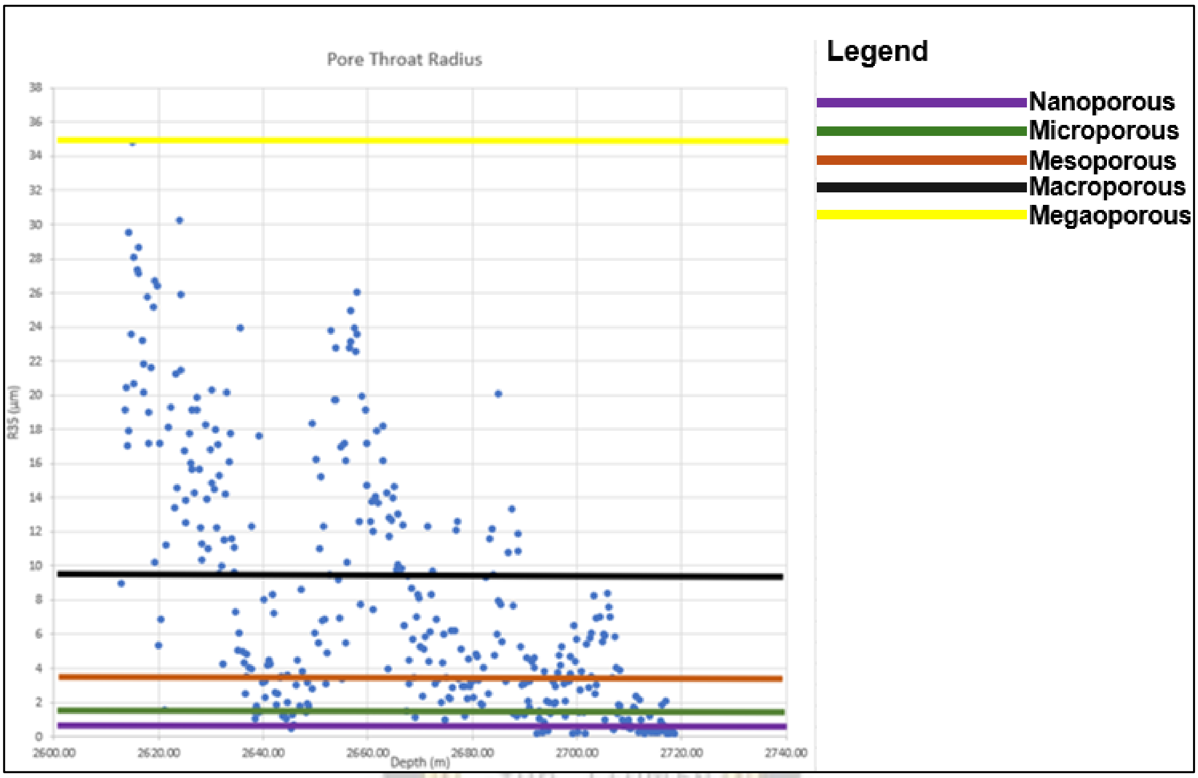

Figure 4.23 Pore Throat Size F-A13 Reservoir.

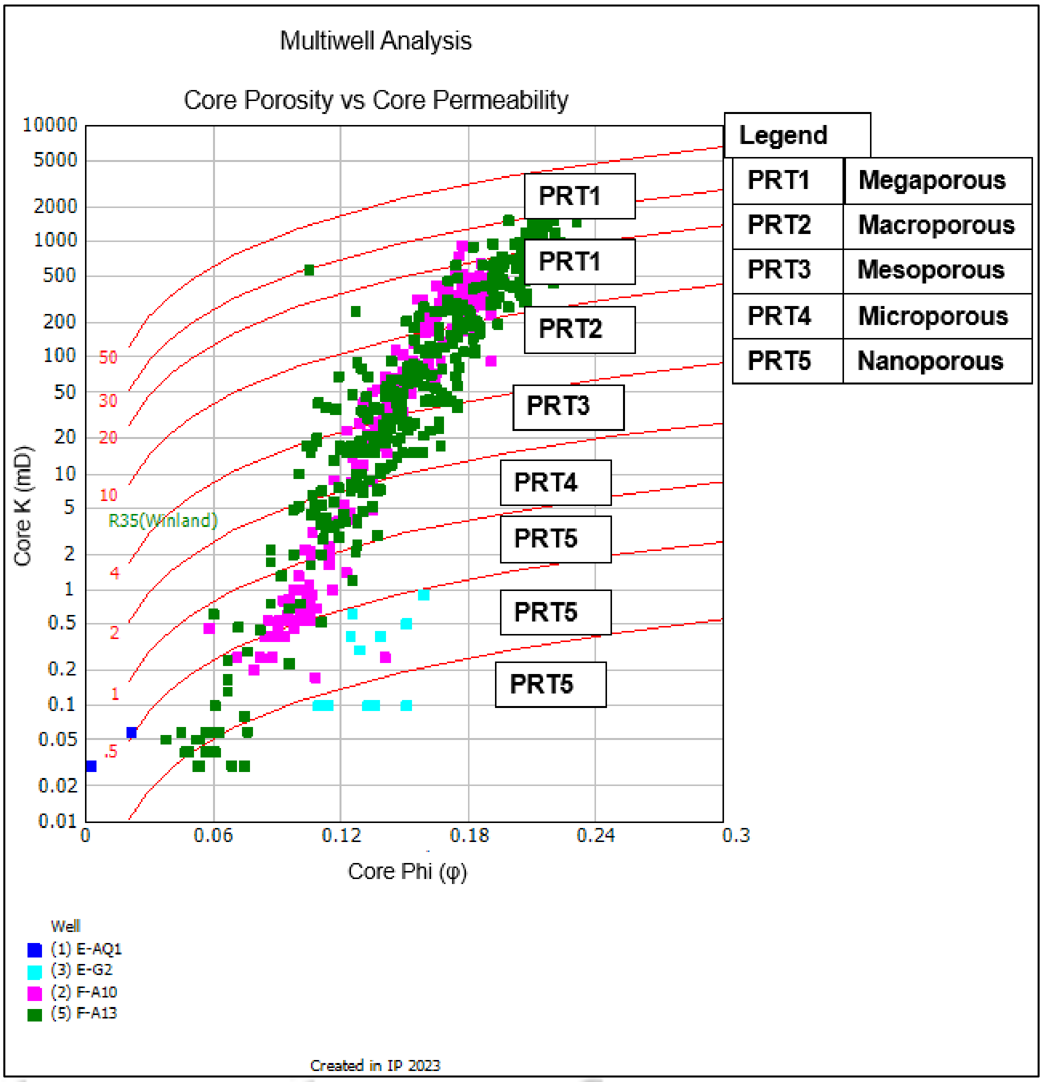

Figure 4.24 Multi-well Pore Throat Size Distribution.

4.8 Storage and Flow Capacity

Figure 4.25A shows that storage capacity fluctuates with depth, generally decreasing slightly. This can indicate that going deeper into the reservoir, there are limited pore spaces for CO_2 storage. Flow capacity sharply decreases with depth (Figure 4.25B). This suggests that the reservoir becomes less permeable, making CO_2 injection and flow difficult. Figure 4.25C shows a more spread-out trend of storage capacity. Most points are concentrated at lower values, suggesting that storage capacity decreases with depth. There is a decline in depth regarding the flow capacity for F-A10 (Figure 4.25D), making the reservoir less permeable at higher depths. The presence of smectite in F-A10 may have caused the reduction in permeability as it tends to expand when exposed to fluids. Figure 4.25E shows the storage capacity being clustered at lower values, with some higher values suggesting heterogeneity in the pore spaces. Additionally, flow capacity decreases with depth (Figure 4.25F). This suggests that the reservoir becomes less permeable, and during CO_2 injection, the CO_2 might not spread efficiently in the reservoir.

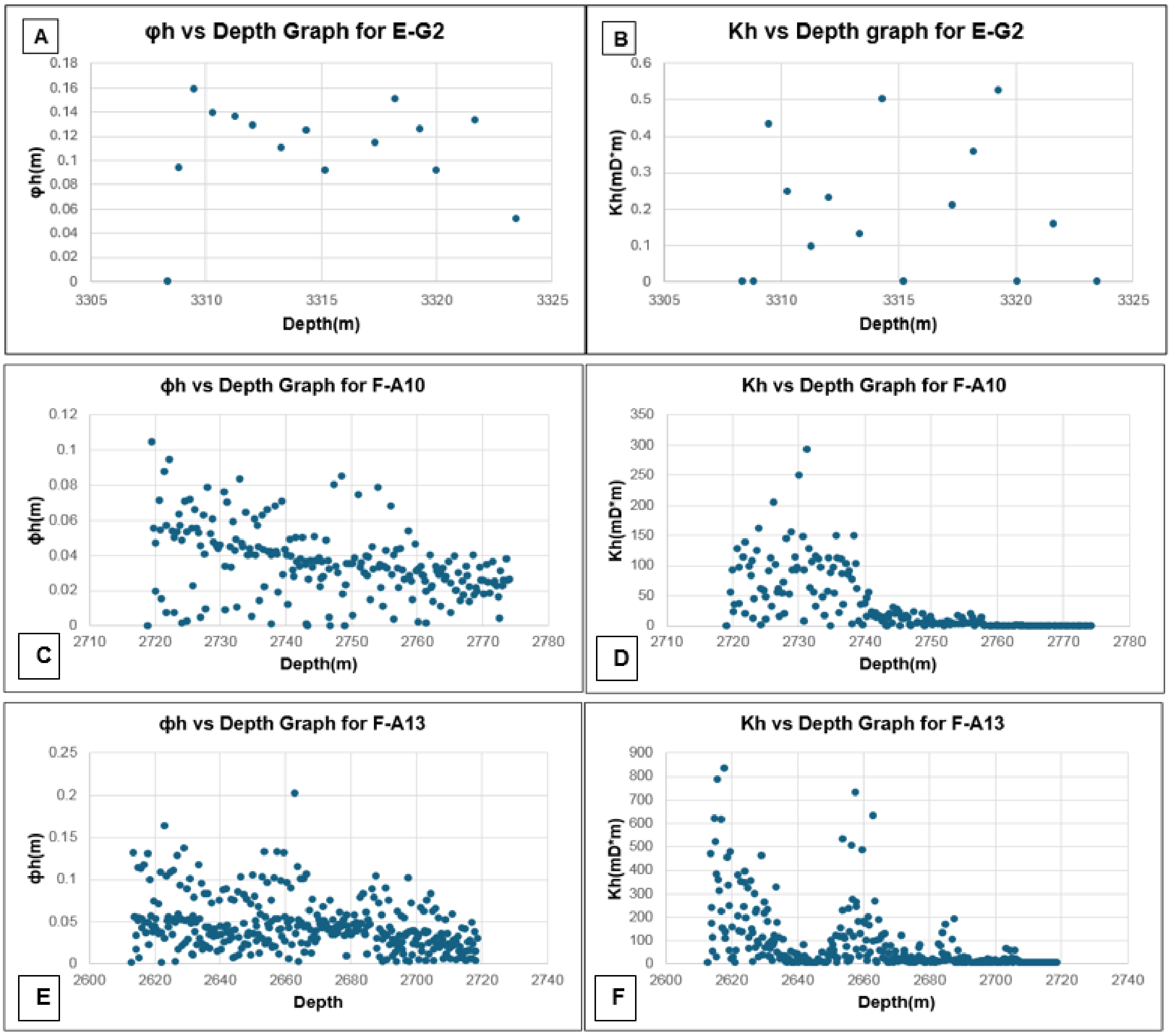

Figure 4.25 Storage and Flow Capacity vs Depth Graphs for All Studied Reservoirs.

The storage capacity represented here is a fraction of the total reservoir volume. Only the porous and permeable parts of the reservoir contribute to the available pore space for CO2 storage. In E-G2 (Figure 4.26), the storage capacity ranges from 78.11–498.04 m, and the flow capacity ranges from 56.49 – 9946.02 mD*m. The average storage and flow capacities are 352.87 m and 3886.11 mD*m, respectively. In F-A10 (Figure 4.27), the storage capacity ranges from 102.83 – 598.37 m, and the flow capacity ranges from 100.72 – 9949.23 mD*m. The average storage and flow capacities are 356.77 m and 4760.80 mD*m, respectively. In F-A13 (Figure 4.28), the storage capacity ranges from 5.45 – 666.65 m, and the flow capacity ranges from 12.43 – 9923.89 mD*m. The average storage and flow capacities are 355.64 m and 2972.81 mD*m, respectively. E-G2 has the lowest storage capacity, and F-A10 has the highest storage capacity. F-A13 has the lowest flow capacity, and F-A10 has the highest flow capacity.

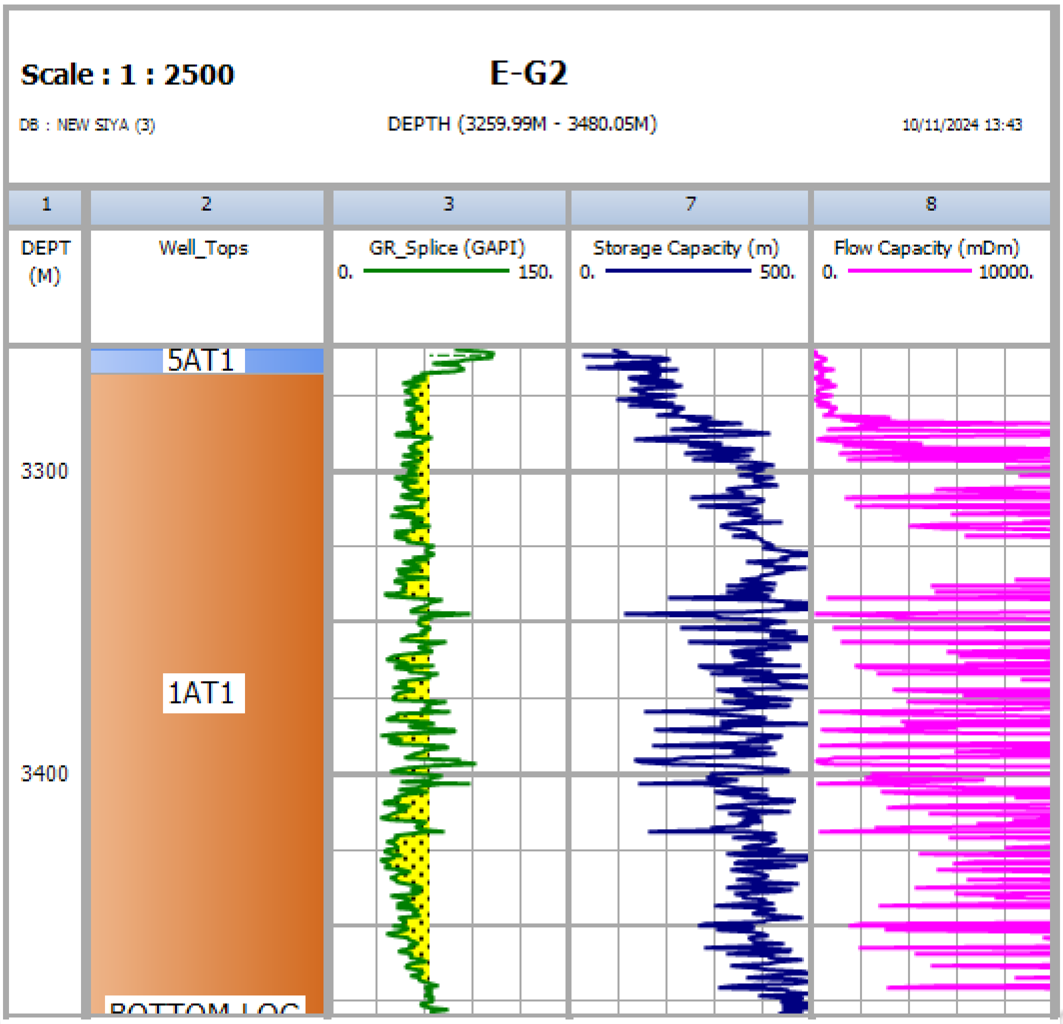

Figure 4.26 Gamma-ray Log of a Sandstone Reservoir (E-G2) with Storage and Flow Capacity Curves.

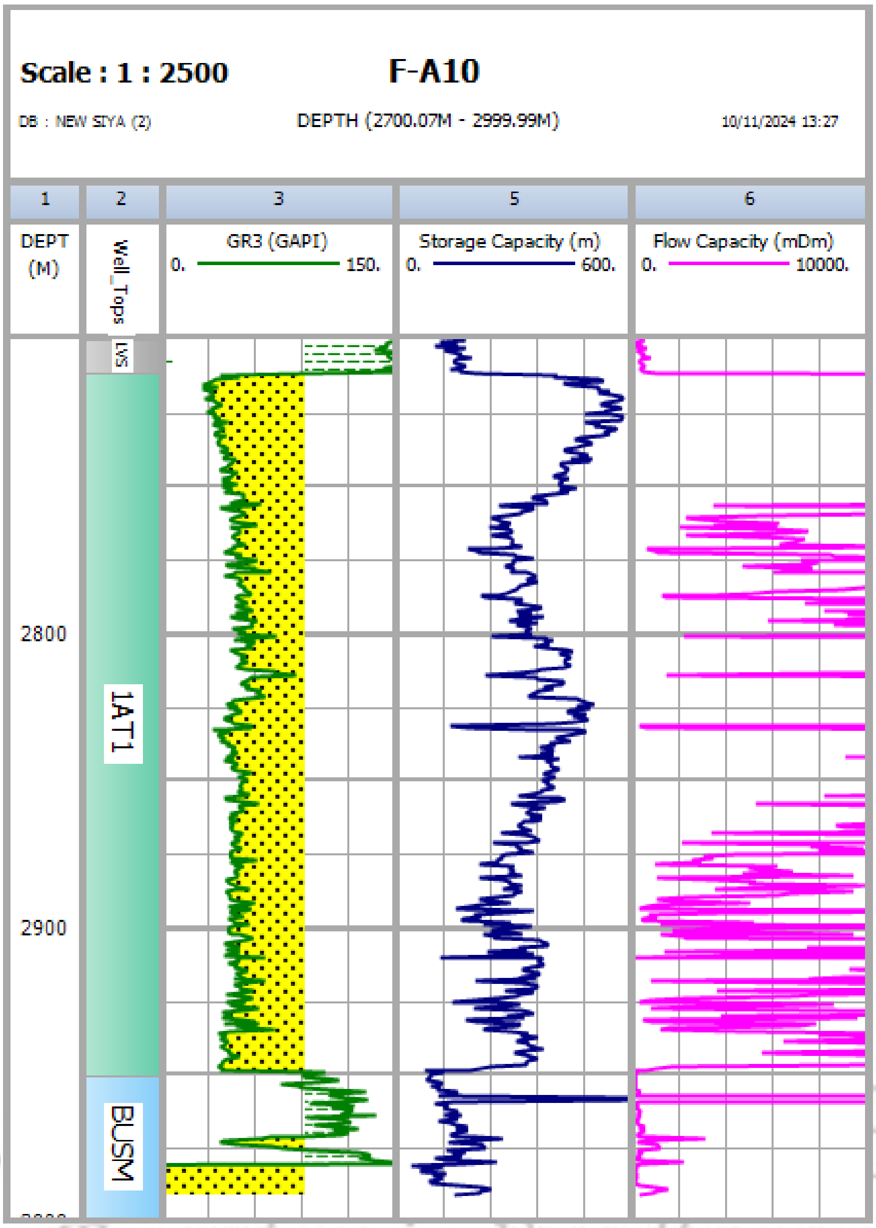

Figure 4.27 Gamma-ray Log of a Sandstone Reservoir (F-A10) with Storage and Flow Capacity Curves.

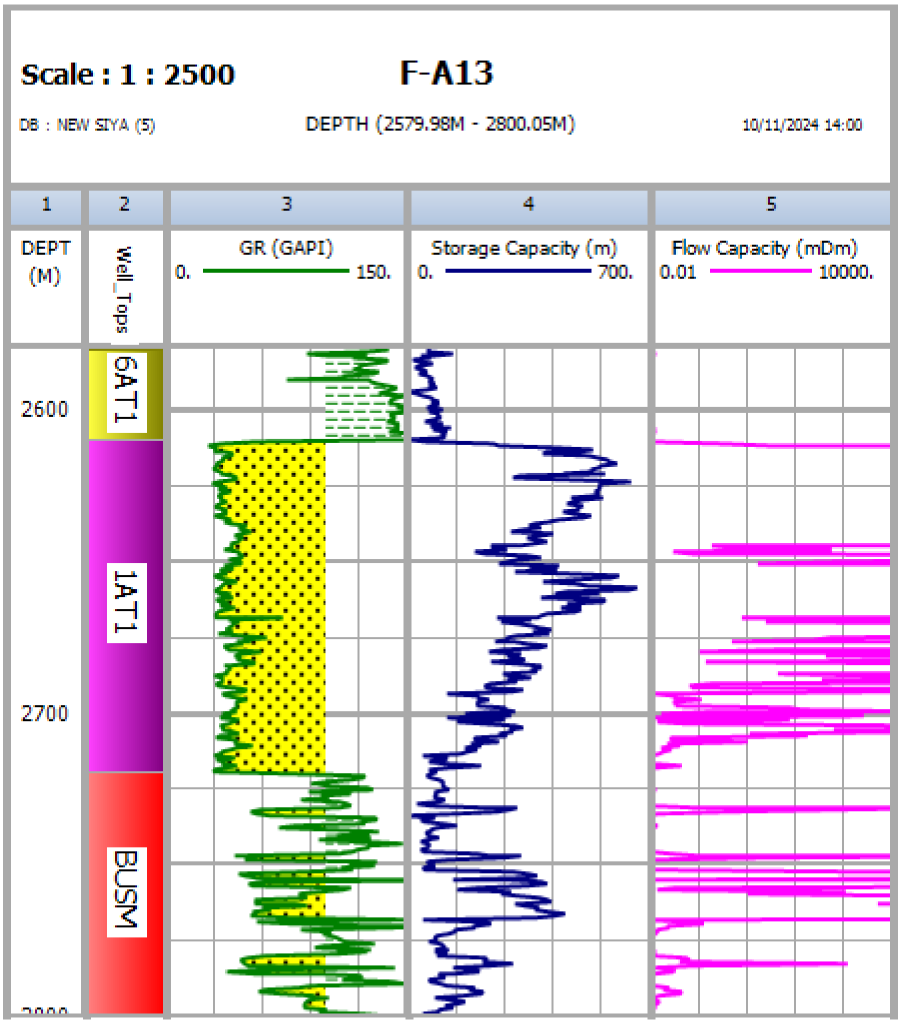

Figure 4.28 Gamma-ray Log of a Sandstone Reservoir (F-A13) with Storage and Flow Capacity Curves.

4.9 3D Visualization Petrophysical Properties Across the Field

Figure 4.29A shows the trend in the average volume of clay. F-A13 in the north has the lowest volume of clay at 0.12v/v (12%), and E-G2 in the south has the highest volume of clay at 0.30v/v (30%). Figure 4.29B shows the trend of the distribution of average porosity, with E-G2 in the south having the lowest porosity of 0.10v/v (10%) and F-A13 having the highest porosity of 0.13v/v (13%). Figure 4.29C shows the trend of average water saturation, with F-A13 in the south having the lowest water saturation of 0.06v/v (6%) and F-A10 having the highest water saturation of 0.68v/v (6%). Figure 4.29D shows the trend of the distribution of average permeability, with E-G2 in the south having the lowest porosity of 6.68 mD and E-AQ1 having the highest permeability of 531.38 mD.

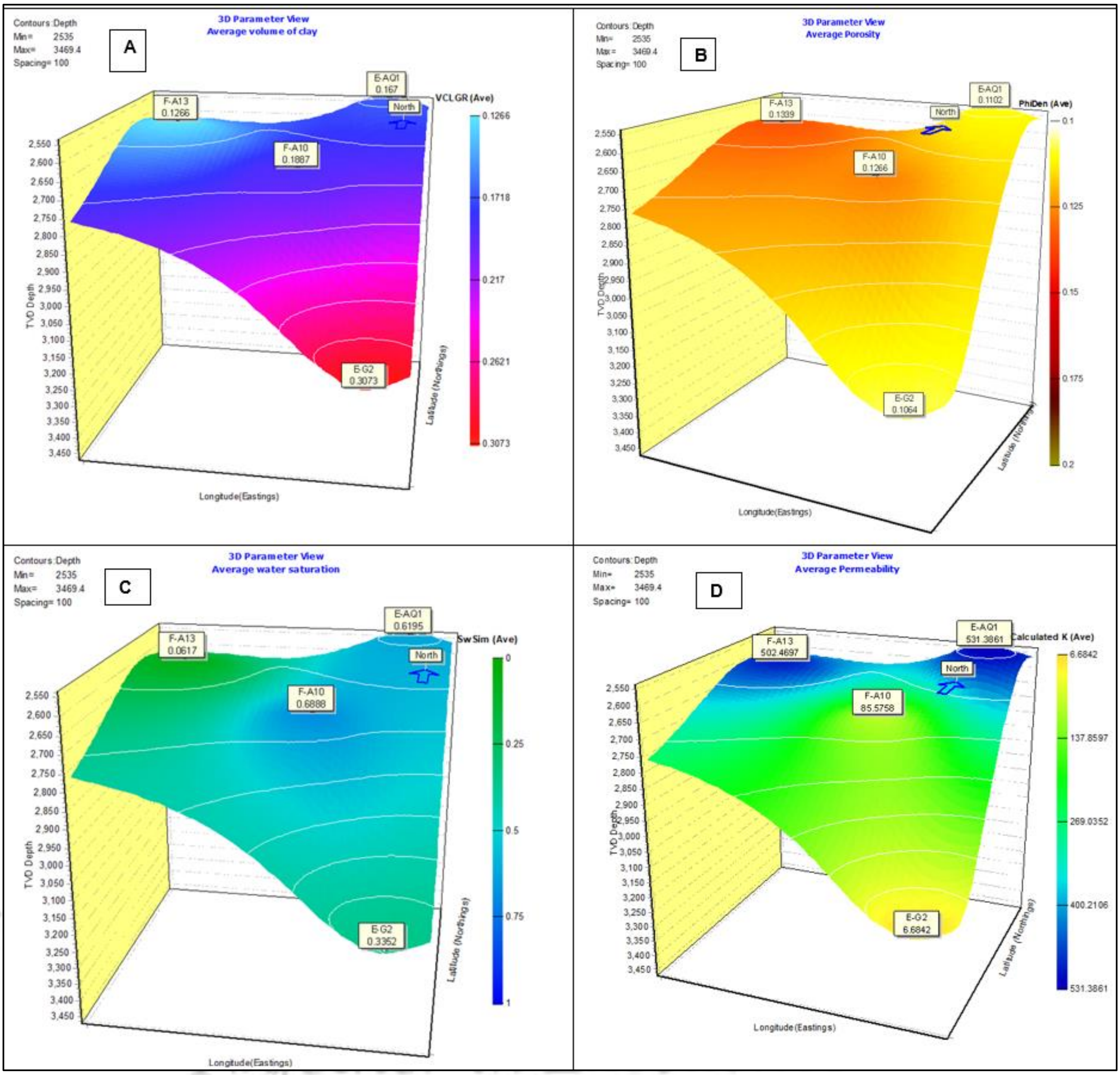

Figure 4.29 A 3-D Parameter Viewer Showing the General Trend of Petrophysical Properties within the Studied Field. (A) Average Volume of Clay, (B) Average Porosity, (C) Average Water Saturation, (D) Average Permeability.

The results from the 3D parameter view show a clear difference across the main parameters affecting carbon storage potential. The low volume of clay and water saturation, high porosity and permeability observed in F-A13 suggest that this reservoir may offer the best conditions for carbon storage, as these factors enhance storage capacity. In contrary, reservoirs with high volume of clay, water saturation and high porosity may cause challenges for carbon storage like restricting the ability of carbon dioxide to flow in between pore spaces.

Chapter 5

5 Impact of Clay Minerals on Petrophysical Properties of Sandstone Reservoirs

5.1 Introduction

The findings and interpretation of the petrographic analysis and core description of the reservoirs are presented in this chapter. A core description of potential sandstone reservoir involves studying core samples extracted from the subsurface of the sedimentary basin during drilling to understand reservoir properties better, as they play a role in storing fluids such CO_2. In sedimentary basins, clay minerals such as kaolinite, illite, smectite, and chlorite are the most common in clastic reservoir rocks. The mode in which clay minerals occupy pores, whether pore-filling, pore-lining, or pore-bridging, can significantly affect basic petrophysical properties (AlKharraa et al., 2023). Certain clay minerals like kaolinite, chlorite, and illite can negatively influence permeability by blocking interconnected pore throats with fine particles within porous media (Ahmad, 2019).

Glauconite is frequently found in sedimentary deposits across marine shelves (Odin & Matter, 1981). SEM-EDS and thin sections were conducted to examine the micro-morphology of the clay minerals on the effect of porosity and permeability of the reservoirs. Integrating core description with petrography analysis provides a deeper understanding of the sandstone reservoirs. Core description alone does not show mineralogical and textural characteristics that may explain diagenetic history, porosity, and permeability.

5.2 Aim and Objectives

This study aimed to examine the core samples and investigate the effect of clay minerals on porosity, permeability, and pore throat size. The core samples were analysed by identifying their physical characteristics, such as lithology, texture, and colour. Thin-section and SEM-EDS analysis were used to investigate the mineralogy of the samples. The thin sections described the grain size, shape, packing, compaction, and cementation. Meanwhile, SEM provided an understanding of the microscale features of the rock samples, thereby improving the knowledge of their morphology.

5.3 Materials and Methods

5.3.1 Data Analysis

The Schlumberger Service Company gathered the data used in this study, which was supplied by the Petroleum Agency of South Africa (PASA). It included geological well completion reports, 13 core samples, 16 thin-section slides, and geophysical wireline logs. Before the data was loaded into Interactive Petrophysics (IP) 2023 for log curve display, it was carefully processed, organised, and packaged for accessibility and quality control (QC). The Petroleum Agency of South Africa's core warehouse in Cape Town, South Africa, is where the core description and thin section slides were conducted and acquired. The biology department at the University of Fort Hare conducted the eight SEM-EDS analysis.

5.3.2 Thin Section Analysis

PASA supplied polished thin sections for each well in this study (Figure 5.1A). The depth of the chosen reservoirs was taken into consideration when selecting the thin sections. A petrographic microscope (Figure 5.1B) was used to observe rock samples under a microscope using a 10 μm scale in both plain and crossed polarised light. This assisted in the detection of minerals, sorting, authigenic cement appearance, and pore space characteristics. The desktop PC displayed the thin-section photographs (Figure 5.1C).

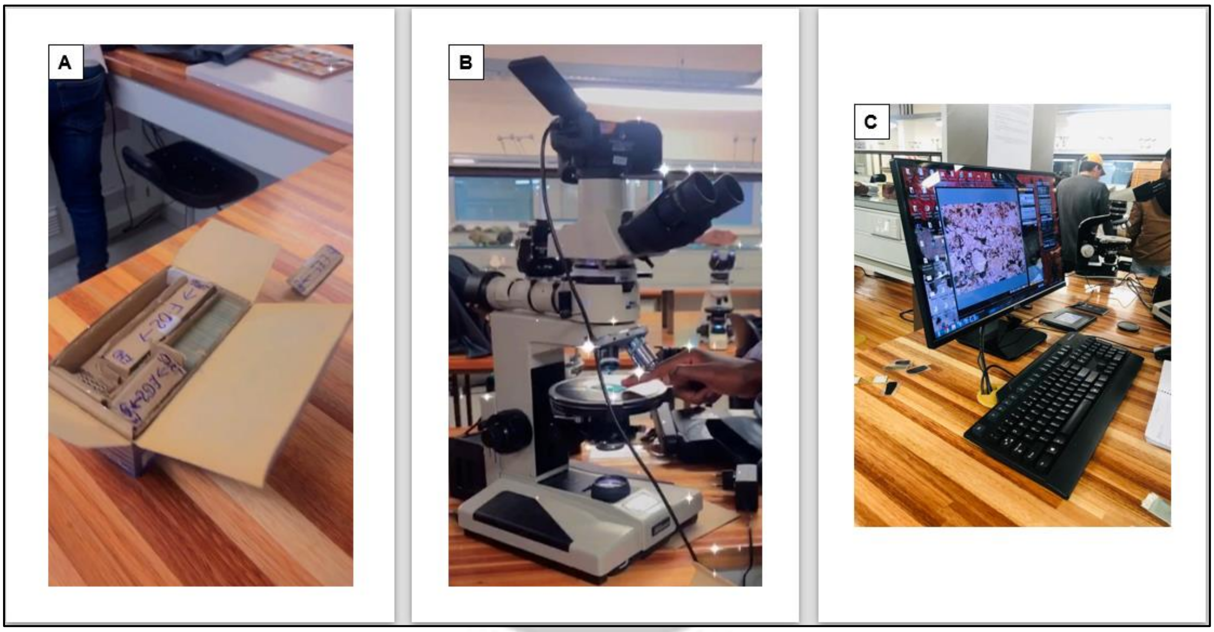

Figure 5.1 Thin-Section Analysis Procedure, (A) Polished Thin Sections, (B) Petrographic Microscope, (C) Desktop

5.3.3 Scanning Electron Microscopy-Energy Dispersive X-ray Spectroscopy Analysis

The core samples were broken into smaller pieces (Figure 5.2B) to fit inside the coating machine (Figure 5.2A). The JEOL JSM-6390LV SEM (Figure 5.2C) equipment was utilized to analyse the samples. Gold was used to coat the samples in the AC100V Eiko IB-2 Ion coater for 30 minutes prior to performing SEM-EDS analysis. Coating the samples is an essential step as it reduces the charge of the sample, making it easier to analyse. The samples were inserted into the SEM for analysis. The results were observed from the two monitors, one for SEM and the other for EDS.

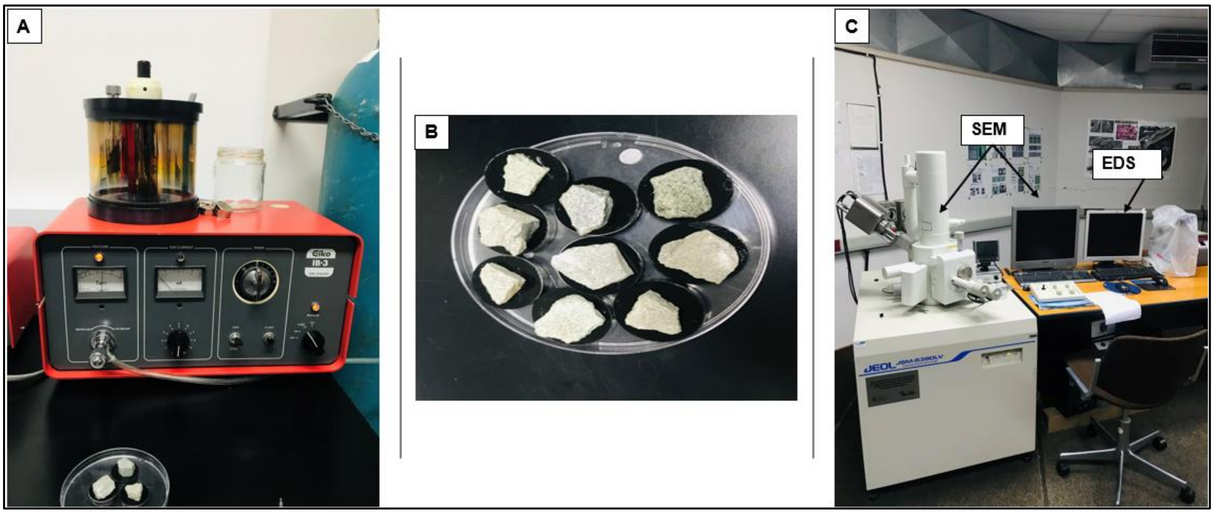

Figure 5.2 Procedure for SEM Analysis, (A) Coating Machine, (B) Core Samples, (C) JEOL JSM-6390LV SEM/EDS

5.4 Core description results

5.4.1 Core Description for E-AQ1

Four cores were cut back to back to examine the physical properties and investigate the reservoir properties. Core 1 was cut from 2502 - 2513 m; Core 2 was cut from 2614 - 2614.10 m; Core 3 was cut from 2614.10 - 2618 m; and Core 4 was cut from 2958 m to 2964 m. Only 15 % of core 1, consisting of 100 % massive non-fluorescing sandstone, was recovered. 0 % was recovered for core 2, 73.8 % was recovered for core three, and 84 % recovered for core 4. Three cores at different intervals were examined for E-AQ1.

Core sample 1 is the uppermost sandstone unit (Figure 5.3). It is clean, well-sorted, and fine-grained. The sand is glauconite and shelly (with bivalve and echinoderm remains) at the top, decreasing slightly with depth. It is light green-grey and has calcite cement. Core sample 2 was found at 2614.12 m (Figure 5.3). It was identified as a massive, light greenish grey, fine to occasionally medium, well sorted, round glauconitic, carbonaceous, and very calcareous sandstone.

Core sample 3 was obtained from 2615.30 – 2615.50 and 2615.72 – 2616.60 m. The sandstone is extensively fractured. At least two episodes of steep pentecontemporaneous fracturing occurred. Some of these open fractures are calcite-filled. Wavy bands randomly oriented, darker, more argillaceous, and carbonaceous materials may be remnant bedding planes or stylolites. The sandstone is tight due to pervasive calcareous cement.

Figure 5.3 Core samples for E-AQ1. Core Sample 1: 2502.23-2502.40 m, Core Sample 2: 2614.2 m, Core Sample 3: 2615.30 – 2615.50 and 2615.72 – 2616.60 m.

5.4.2 Core Description for E-G2

A single core in the pre-horizon C (Portlandian age) shallow-marine sandstones was cut from 3307 - 3325 m with 100 % recovery. The core is a massive sandstone with pale blue to pale yellow fluorescence throughout. Two cores found at different intervals were examined (Figure 5.4). Core samples 1 and 2 were obtained from 3499.47 and 3500.30 m, respectively. They are both light grey sandstones and very fine-grained. Core sample 1A and core sample 1B have an abundance of silica and feldspar cement with visible reservoir bitumens that block duct deformation grains and the pore throats. Glauconite is also present. Reservoir bitumens are highly viscous, asphaltene-rich hydrocarbons (Saidian et al., 2015). Core sample 2A and core sample 2B are very calcareous.

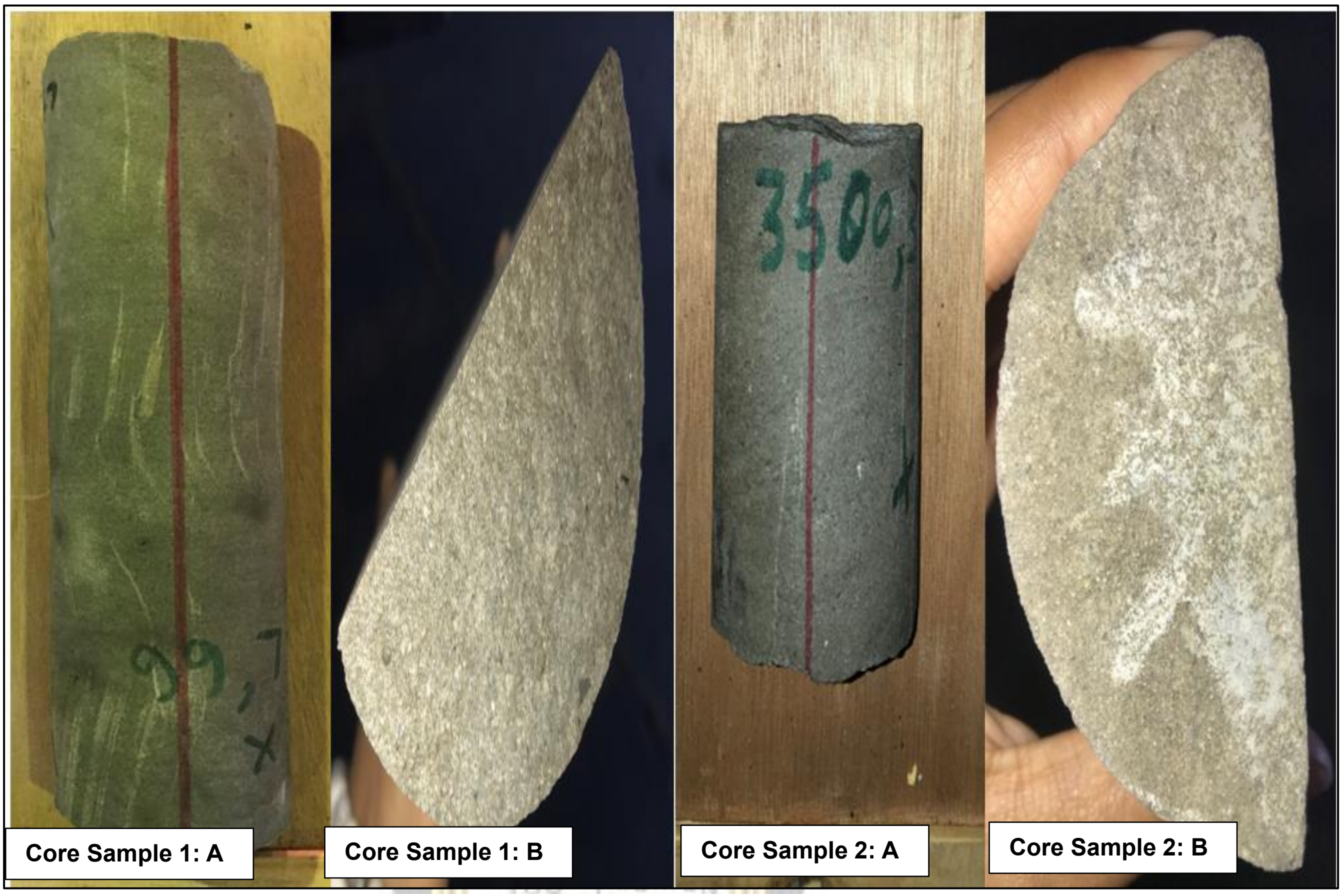

Figure 5.4 Core samples for E-G2. Core Sample 1A and B: 3499.47 m. Core Sample 2A and B: 3500.30 m.

5.4.3 Core Description for F-A10

Three 18m cores each in the pre-horizon C shallow-marine sandstones were successfully cut back-to-back, with cores 1 and 2 having 100 % recovery and core 3 having 98.9 % recovery. When a significant drop in ditch gas levels suggested that the gas-water contact had been intersected, coring was stopped after core 3. Four cores found at different intervals were examined (Figure 5.5). Core sample 1 was obtained at 2719.37 m. It is a massive glauconitic sandstone that is light grey. The abundance of glauconite suggests a shallow-marine coastal sandstone deposit.

Core sample 2 was obtained at 2724.62 – 2724.85 m. It is a medium grey sandstone with mud drapes, medium to fine-grained. Core sample 3 was obtained at 2733.12 – 2733.4 m. It is a light to medium green-grey calcareous, medium-grained and occasionally fine-grained sandstone. Core sample 4 was obtained at 2757.57-2758.03 m. It is a light-medium grey sandstone with better-preserved cross-bedding features. Bioturbation is also present in heavily burrowed zones, which are mostly horizontal. This implies a relatively high-energy shallow depositional environment.

Figure 5.5 Core samples for F-A10. Core Sample 1: 2719.37 m, Core Sample 2: 2724.62 – 2724.85 m, Core Sample 3: 2733.12 – 2733.4 m, Core Sample 4: 2757.57- 2758.03 m.

5.4.4 Core Description for F-A13

From 2613 to 2741 m, seven cores were cut consecutively. A glauconitic sandstone that turns fossiliferous with depth is found between 2613-2720 m. Below 2720 m, claystone is more common. Four cores were examined for this reservoir (Figure 5.6). Core sample 1 was found at 2613.78 m. It is a light to medium green-grey sandstone with visible pore spaces. There are also visible pyrite streaks and white patches on the core, which could be leached patches. The rock texture is medium-grained. Core sample 2 was obtained at 2648.82 – 2648.96 m. It is a medium grey shelly sandstone. The rock texture is fine to coarse-grained. Bioturbation is also visible. Core sample 3 was obtained at 2664.2 – 2665.08 m. It is a medium grey sandstone that changes its rock texture as you go down with depth. It changes from fine-grained to medium-grained. The core sample is also poorly bedded. Core sample 4 was found at 2719.81 m. It is a very finely laminated green claystone that is highly bioturbated.

Figure 5.6 Core samples for well F-A13. Core Sample 1: 2613.78 m, Core Sample 2: 2648.82 – 2648.96 m, Core Sample 3: 2664.2 – 2665.08 m, Core Sample 4: 2719.81 m.

5.5 Petrography Results

5.5.1 E-AQ1 Mineralogy Interpretation

Figure 5.7A shows glauconite and detrital quartz as the most dominant minerals at 2589-99 m, suggesting that the sandstone was deposited in a shallow marine environment. The presence of early poikolotopic calcite cementation suggests that the cementation occurred in early diagenesis and is not uniformly distributed. The cementation also forms irregular patches within the rock. Additionally, figure 5.7B shows quartz overgrowth that is depicted by a yellow arrow. Generally, quartz overgrowths are quartz layers forming on the surface of quartz grains in a sedimentary environment as cement (Sanderson, 1984).

Micrite calcite cementation can be observed filling the pore spaces between the detrital grains in Figure 5.7B. Figure 5.7C shows a fracture (navy arrow) cemented by coarse crystals of ferroan dolomite (brown hue), suggesting that the fracturing occurred together with the cementation of the sands. Figure 5.7D shows an abundance of glauconite with echinoderm and bivalve shell fragments and carbonaceous material. There are also small patches of carbonaceous material. Calcite grain was also observed to be pinkish.

Feldspar grains, characterized by their grey colour and high relief are visible. The SEM microphotographs (Figure 5.8) show an abundance of authigenic quartz (yellow arrow) at 2502.23 m. The red arrow shows a fractured face, and the step-like features (Figure 5.8A) which could be brittle fractures where the rock broke along specific planes. There are no visible pore spaces on the SEM at 2615.30 m. The calcite cementation may have filled them. The EDS in Figure 5.8D shows the elemental composition of quartz found in the sandstone at 2502.23 m.

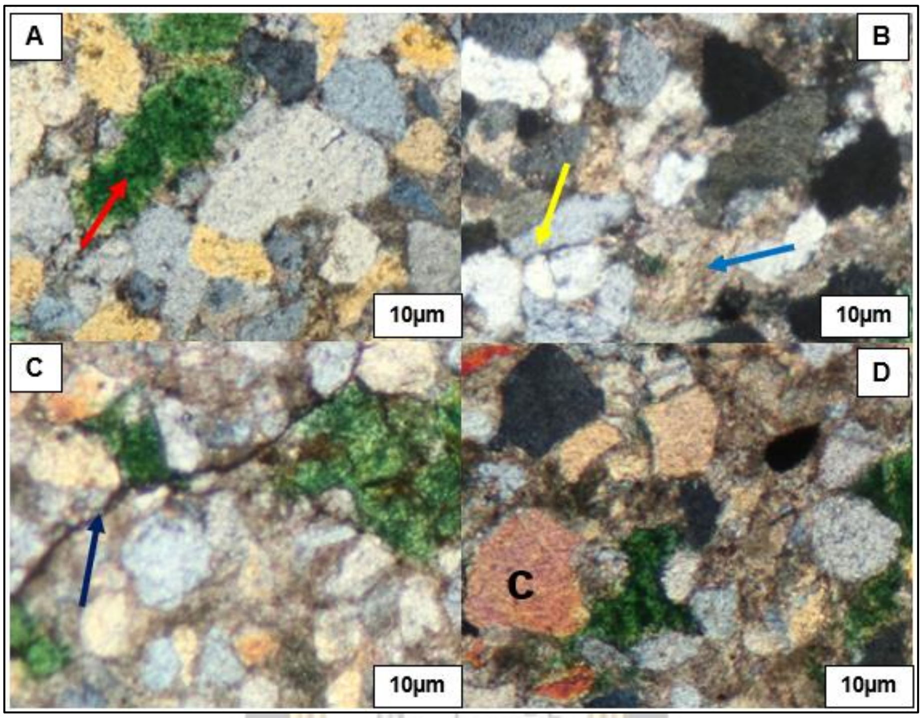

Figure 5.7 (A) glauconite (red arrow) (B) 2589-99 m: quartz overgrowth (yellow arrow), calcite cementation (blue arrow) (C) 2614.50 m: fracture (navy arrow), (D) 2614.50 m: C= calcite.

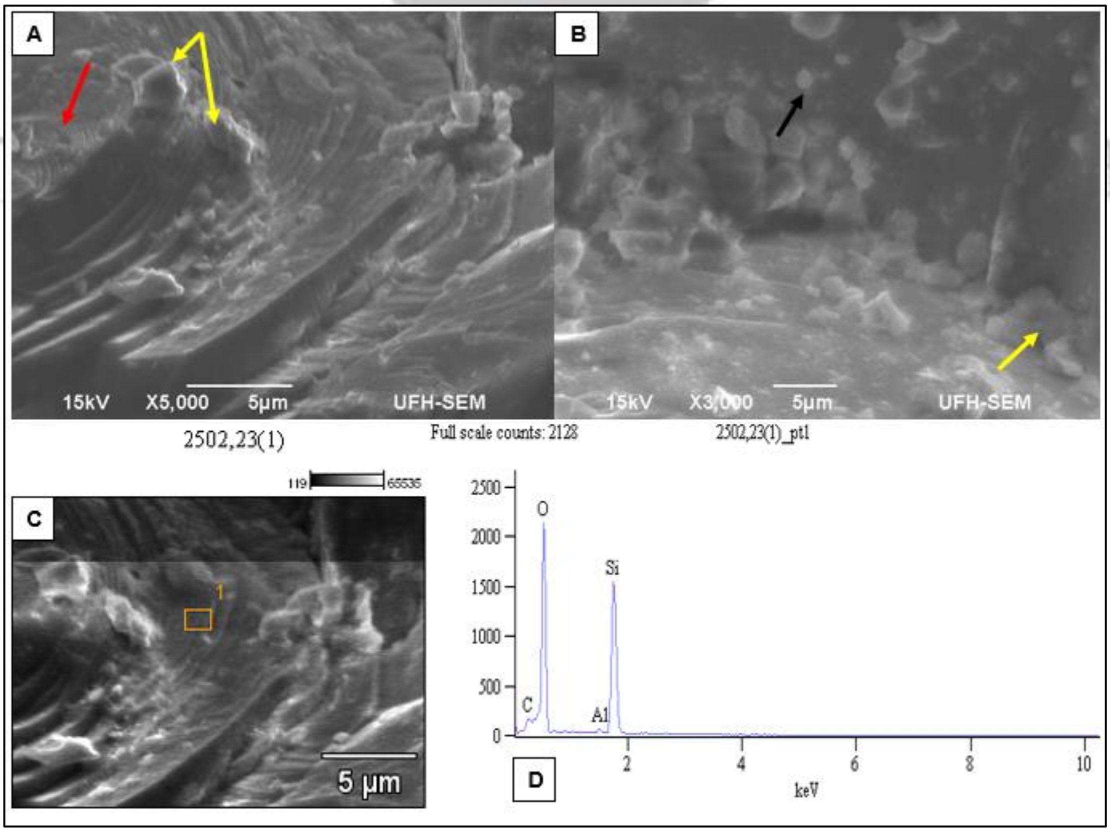

Figure 5.8 E-AQ1 SEM and EDS analysis. (A) authigenic quartz grain with arc-shaped steps at 2502.23 m (yellow arrow) (B) aggregate quartz (yellow arrow) and calcite crystals (black arrow) grain arranged in a different orientation at 2615.30 m (C) Analysed point for EDS marked as 1 (D) EDS data showing the elemental composition of quartz.

5.5.2 E-G2 Mineralogy Interpretation

In Figure 5.9A, the minerals are closely packed, showing evidence of compaction and hematite cementation. Figure 5.9B shows feldspar alteration (yellow-brown) that is also filling the pore spaces. The alteration is evidence for mineralogical changes influenced by diagenetic processes. In addition, there is also a presence of flakes, which could imply the existence of organic matter, which darkens the rock. The evidence of compaction in the closely packed minerals indicates the effects of burial and diagenesis, decreasing the rock's porosity and permeability. Resulting in a tight reservoir.

Figure 5.9D shows a grey feldspar marked by cleavage planes, which contributes to the detrital components of the sediment. Glauconite is also present. The red arrow shows feldspar overgrowth, which is evidence of diagenetic processes. The feldspar overgrowth can reduce the permeability and porosity of the reservoir as the overgrowth fills in the remaining pore spaces. The SEM (Figure 5.10A) shows angular quartz grain (yellow arrow) and a wavy-like feature (blue arrow) at 3499.47 m.

The webby rosette like morphology observed in the SEM images indicate the possibility of smectite to chlorite transformation shown by the red arrow in Figure 5.10B. This suggestion is also supported by the visible pore space depicted by the orange arrow and chlorite is often associated with its pore-lining nature. Smectite recrystallisation tends to fill the pore spaces as the chlorite precipitates. The EDS in Figure 5.10D shows the elemental composition of quartz and the possibility of calcite cement found in the sandstone at 3499.47 m.

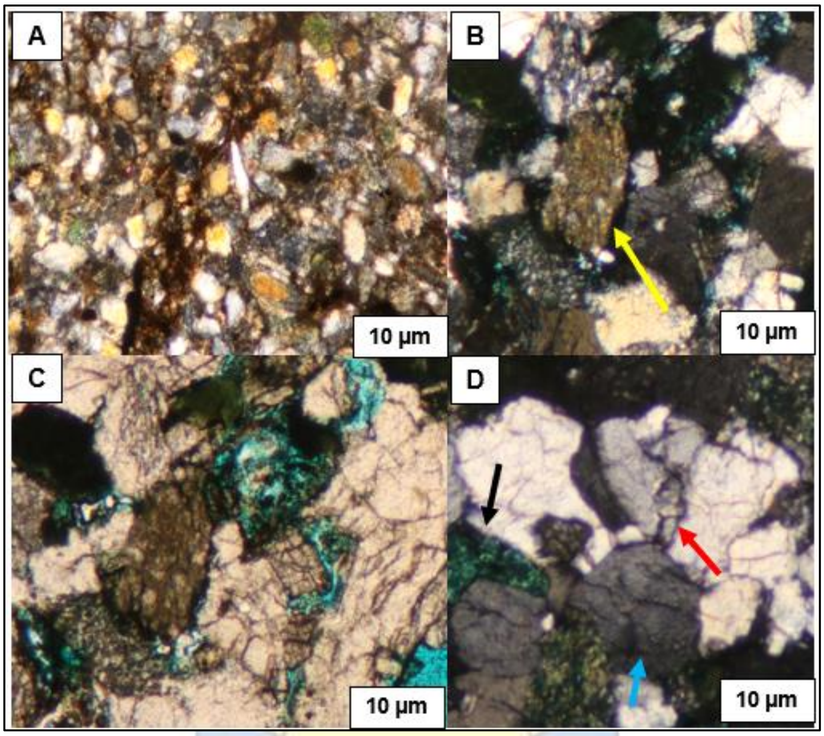

Figure 5.9 (A) 3290-3300 m: hematite cementation (B) 3307.25 m: Feldspar alteration (yellow arrow). (C) 3307.25 m under plane-polarized light (D) 3319.2739 m: feldspar overgrowth (red arrow), glauconite (black arrow), feldspar (blue arrow).

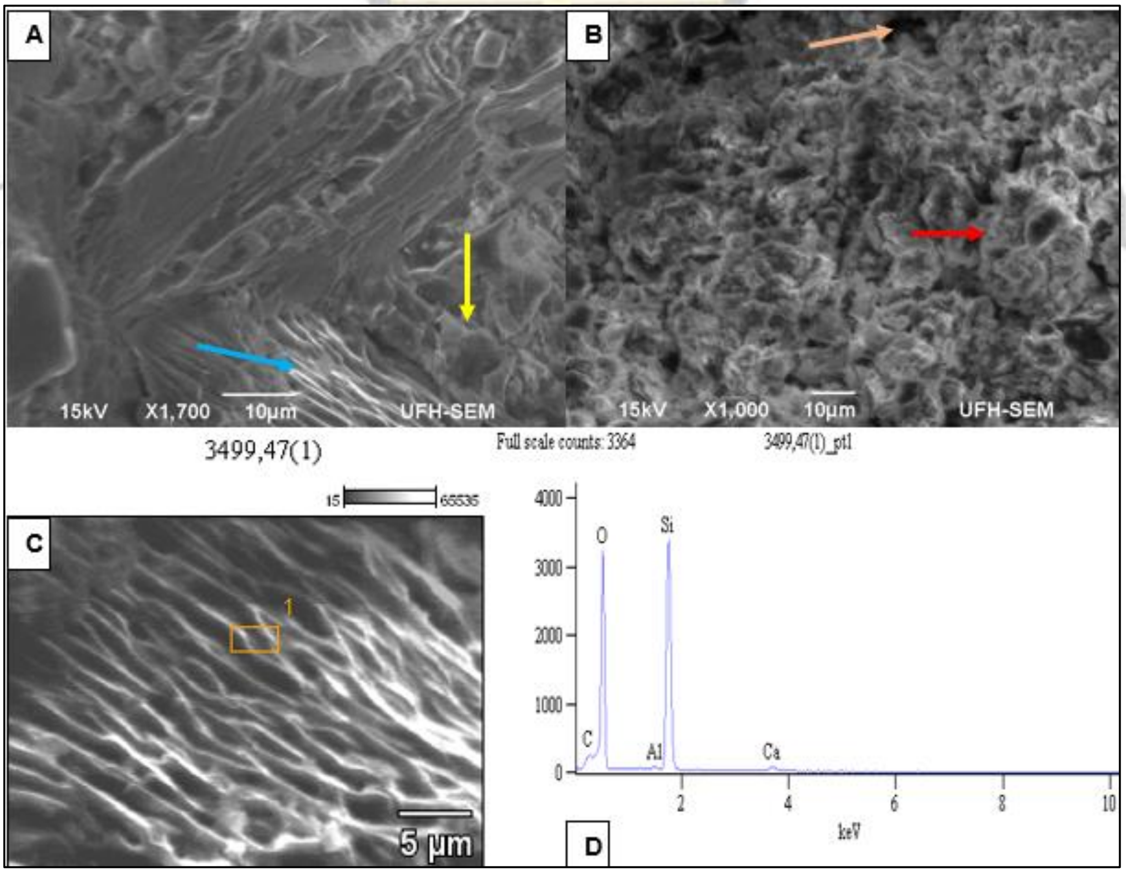

Figure 5.10 E-G2 SEM and EDS analysis. (A) angular quartz grain at 3499.47m (B) recrystallised smectite with quartz grain at 3500.3m (C) Analysed point for EDS marked as 1 (D) EDS data showing elemental composition of quartz, with a possibility of calcite cement.

5.5.3 F-A10 Mineralogy Interpretation

Figure 5.11A shows coarse grains of feldspar which could enhance overall porosity by creating larger pore spaces between grains. Feldspar overgrowth is also visible (black arrow). In Figure 5.11B (yellow arrow), clay minerals are visible, blocking pore spaces and potentially impacting reservoir quality. Additionally, carbonaceous material fills the pore spaces, indicating organic content within the sandstone reservoir. Figure 5.11C (red arrow) shows glauconite minerals containing organic inclusions.

Figure 5.11D shows abundant feldspar alteration, suggesting significant chemical weathering after burial. In Figure 5.12A, SEM microphotographs at 2719.37 m reveal a webby crenulated recrystallised smectite and a quartz grain (yellow arrow). The recrystallised smectite may fill into pore spaces that would otherwise be available for carbon storage. The blue arrow indicates a visible pore space. At 2724.62 m, recrystallised quartz (red arrow) and primary quartz (orange arrow) are observed. The recrystallised quartz affected the texture and structure, possibly due to compaction which is evidenced by their stacking. The orange arrow highlights quartz overgrowth filling pore spaces, potentially impacting porosity and permeability. The EDS in Figure 5.12D shows the elemental composition of carbonate minerals, calcite, or dolomite found in the sandstone at 2719.37 m.

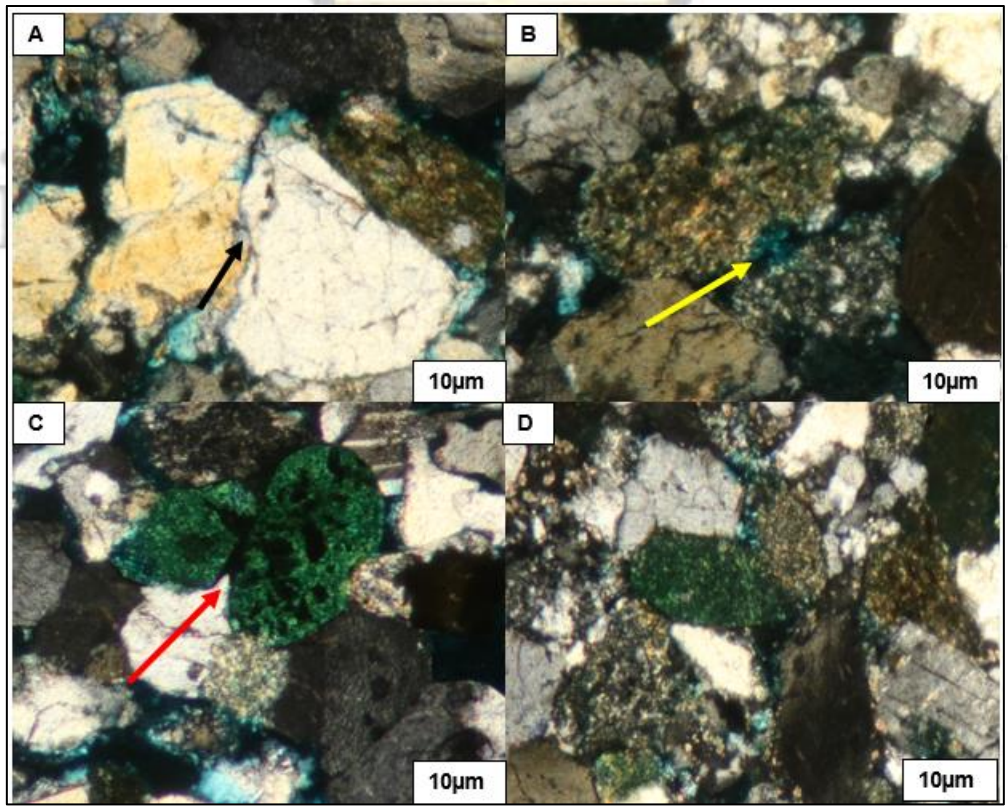

Figure 5.11 (A) 2712.5 m: black arrow showing feldspar overgrowth. (B) 2724.97-2725.16 m: clay mineral blocking pore space. (C) 2756.56-71 m: glauconite (red arrow) (D) 2768.04- 2768.26 m: glauconite and abundance of feldspar alteration.

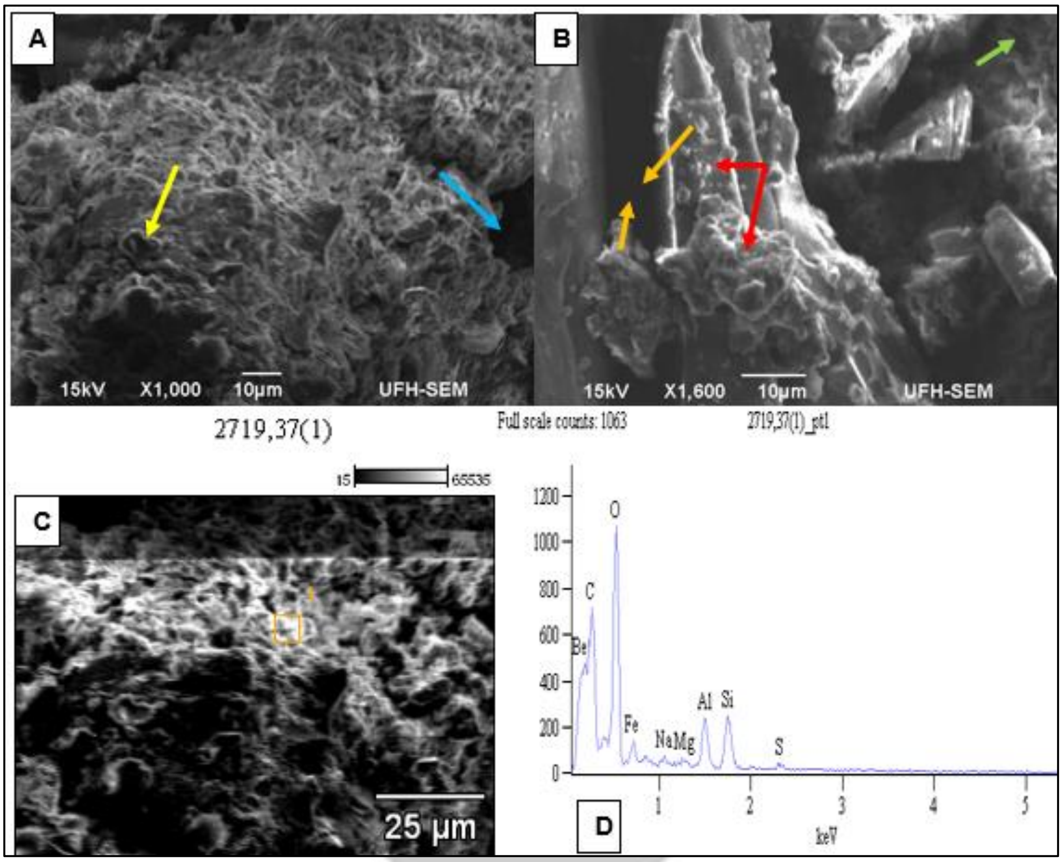

Figure 5.12 F-A10 SEM and EDS analysis. (A) recrystallised smectite with quartz grain (yellow arrow) with visible pore spaces (blue arrow) at 2719.37 m (B) primary quartz (orange arrow) and recrystallised quartz newly grown (red arrow), possible smectite (green arrow) at 2724.62 m (C) Analysed point for EDS marked as 1 (D) EDS data showing elemental composition of carbonate minerals such as calcite or dolomite.

5.5.4 F-A13 Mineralogy Interpretation

The studied reservoir has shown the presence of detrital feldspar grains (grey) and feldspar cement (overgrowth) (Figure 5.13A). Figure 5.13B shows a porous and permeable sandstone rock, with the interconnected pore spaces shown by the blue colour known as a dyed epoxy glue resin. This resin is often visible under plane-polarized light and is used during the preparation of the slides. The interconnected pore spaces show that CO_2 can move freely between the rock grains when it is injected into the reservoir.

The blue arrow in Figure 5.13C shows a pink colour, which could be calcite cementation. The grains in Figure 5.13D shown by the red arrow show calcite cement, which significantly destroys the porosity. Glauconite is also present (green arrow). The SEM in Figure 5.13 shows a webby recrystallised smectite pointed by a red arrow at 2648.82 m. Figure 5.13B shows a needle-like mineral consistent with illite, it is shown by a blue arrow, and an angular quartz grain next to it, shown by an orange arrow.

There is also a presence of smectite (yellow arrow) next to the pore spaces, indicated by its webby look. The EDS in Figure 5.14D shows the elemental composition of quartz at 2648.82 m depth.

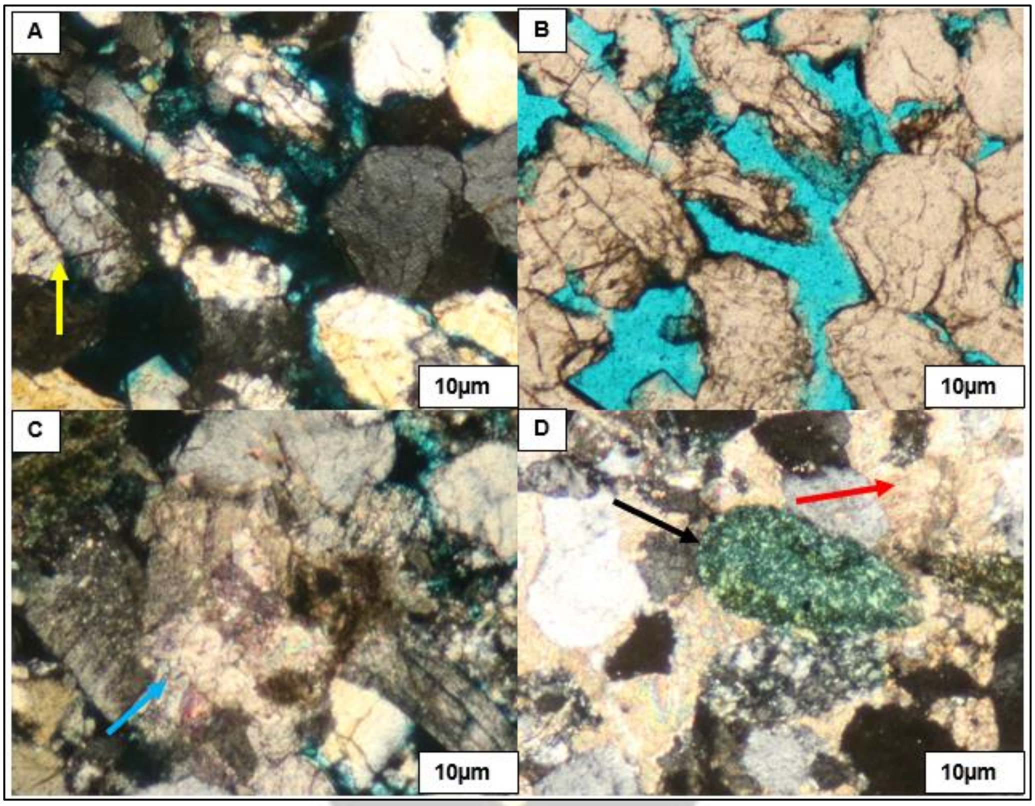

Figure 5.13 (A) 2622.36-62 m: feldspar overgrowth (yellow arrow). (B) 2622.35-62 m: under plane-polarized light, showing visible pore spaces (depicted by blue colour) (C) 2699.92-700.07 m: calcite cementation (blue arrow). (D) 2717.32-56 m: glauconite (black arrow), poor cementation and compaction (red arrow).

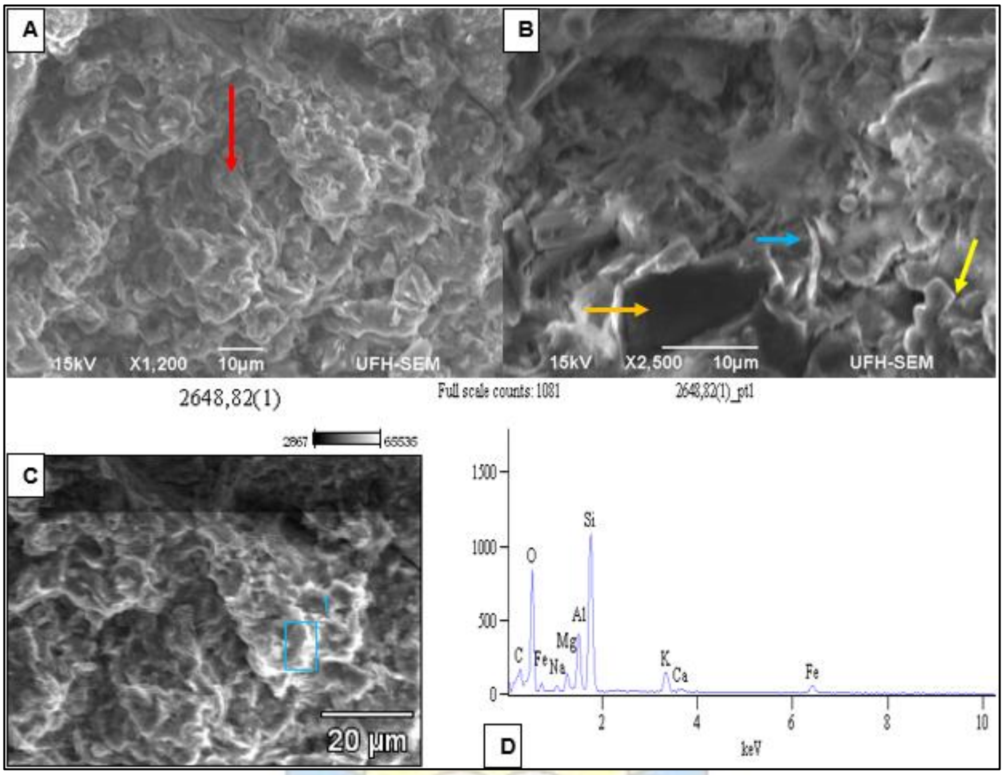

Figure 5.14 F-A10 SEM and EDS analysis. (A) recrystallised smectite with quartz grain (red arrow) at 2648.82 m (B) illite (blue arrow) and quartz grain with angular features (orange arrow), with possible smectite mixture (yellow arrow) at 2648.82 m (C) Analysed point for EDS marked as 1 (D) EDS data showing the elemental composition of quartz.

Chapter 6

6 Conclusion and Recommendations

6.1 Conclusion

The investigation of well logs, core, and petrographic data allowed for the exploration of the petrophysical and petrographic features of the lower cretaceous sandstone reservoirs in the Bredasdorp Basin. These reservoirs had depths ranging from 2535 to 3469.4 metres. The following deductions were made:

1. The calculated average volume of clay for E-AQ1, E-G2, F-A10 and F-A13 is 16.73 %, 30.73 %, 18.87 % and 12.66 % respectively. The average effective porosity for E-AQ1, E-G2, F-A10 and F-A13 is 13.52 %, 9.37 %, 11.86 % and 13.6 % respectively. The average water saturation E-AQ1, E-G2, F-A10 and F-A13 is 52.72 %, 33.52 %, 68.88 %, and 6.17 % respectively. The average permeability for E-AQ1, E-G2, F-A10, and F-A13 is 11.21, 6.68, 85.57, and 502.47 mD, respectively. F-A13 reservoir showed the lowest volume of clay, and the E-G2 reservoir showed the highest volume of clay. The high volume of clay(smectite) can reduce the porosity of the reservoir by filling the spaces between the grains, which can limit the storage volume for CO_2. E-G2 showed the lowest porosity of less than 10 % and lowest permeability of less than ten mD, which is considered poor for CO_2 storage. For CO_2, the reservoir must be highly porous and permeable so that CO_2 can easily flow inside the reservoir. F-A10 showed the highest water saturation, and F-A13 showed the lowest water saturation. The high water saturation for the F-A10 reservoir will impact the efficiency of CO_2 storage because there are fewer pore spaces for it to be stored. In the pore throat size distribution, F-A10 and F-A13 showed a higher heterogeneity, and E-AQ1 and E-G2 showed the lowest heterogeneity. Only E-AQ1 and E-G2 will have a consistent fluid flow when CO_2 is injected. The calculated average storage capacity for E-G2, F-A10, and F-A13 is 352.87, 356.77, and 355.64, respectively. The calculated average flow capacity for E-G2, F-A10 and F-A13 is 3886.11 mD*m, 4760.80 mD*m and 2972 mD*m respectively. E-G2 has the lowest storage capacity, and F-A10 has the highest storage capacity. F-A13 has the lowest flow capacity, and F-A10 has the highest flow capacity. The general trend of the storage capacity in the E-G2 reservoir decreases with depth. This can indicate that going deeper into the reservoir, there are limited pore spaces for CO_2 storage. Flow capacity also sharply decreases with depth. This suggests that the reservoir becomes less permeable, making CO_2 injection and flow difficult. In F-A10, there is a more widespread trend of storage capacity. Most of the values in the graph constructed are concentrated at lower depths, suggesting that storage capacity decreases with depth. There is a decline in the flow capacity with depth in F-A10, making the reservoir less permeable at higher depths. The F-A13 reservoir shows the storage capacity being clustered at lower values, with some higher values suggesting heterogeneity in the pore spaces. Flow capacity decreases

with depth. This suggests that the reservoir becomes less permeable, and during CO_2 injection, the CO_2 might not spread efficiently in the reservoir.

2. The studied reservoirs showed a variety of sandstones. E-AQ1 showed a fine to medium-grained, glauconitic, carbonaceous, very calcareous sandstone with calcite cement, characterized by fracturing and tight cementation. E-G2 showed light grey, fine-grained sandstones, highly glauconitic, and visible bitumens. F-A10 varied from medium to fine-grained, glauconitic, calcareous sandstones with better-preserved cross-bedding and heavily burrowed zones, indicating a high-energy depositional environment. F-A13 showed a medium grey sandstone with varying grain sizes, visible pore spaces, and bioturbation, transitioning from fine-grained to medium-grained with depth. Glauconite was the most abundant in all four wells. In E-AQ1, quartz overgrowth and calcite cementation reduced porosity and permeability, with calcite filling fractures indicating early fracturing before deep burial. The presence of glauconite suggests a marine environment, but the absence of visible pore spaces implies a significant reduction in the reservoir's capacity to store CO_2. The difference in permeability and porosity of the study area is caused by the different lithologies found and their depths. In E-G2, compaction reduced porosity and permeability, with hematite cementation blocking pores and smectite transforming to chlorite due to diagenesis. F-A10 had coarse grains contributing to high porosity, but feldspar alteration, overgrowth, and clay minerals likely reduced permeability. Recrystallisation of smectite and quartz stacking due to compaction indicate diagenetic processes affecting the reservoir. F-A13 reservoir showed dispersed grains that suggest poor compaction, likely due to early burial before significant diagenesis. Hence the excellent porosity and permeability. The SEM microphotographs showed recrystallised smectite, illite, angular quartz, and possible swelling smectite near pore spaces.

Overall, the findings indicate that reservoir characteristics including porosity, water saturation, and permeability affect the basin's capacity to store CO_2. Additionally, lithology, the existence of clay minerals, cementation and compaction all have an impact on these characteristics. Among the reservoirs under study, F-A13 shows the greatest potential for CO_2 storage. Favourable characteristics for CO_2 storage include low water saturation, high porosity and permeability, and a low proportion of clay in F-A13. The reservoir quality was probably maintained by the inadequate compaction.

6.2 Recommendations

This study only focused on reservoir properties to investigate CO_2 storage in the basin. Other factors should also be considered when evaluating a basin, as these reservoir properties can be heterogeneous. These factors include:

- Evaluating pressure and temperature to maintain the CO_2 in a supercritical state.
- Evaluate the stability of the basin in terms of subsurface fluid flow, ensuring that injected CO_2 remains contained within the reservoir.
- Obtaining seismic data to calculate the CO_2 storage capacity of the reservoir.

- XRD analysis is needed to observe the different minerals in the reservoirs and identify specific minerals and their spatial distribution.

By addressing the underexplored impact of clay minerals on petrophysical properties, this study contributes to the knowledge by improving the characterization of reservoir quality and enabling more accurate predictions of CO_2 storage. The results will help in the identification of potential storage sites and inform strategies for efficient and safe CO_2 storage in sandstone reservoirs.

References

1. Acho, C.B., 2015. Assessing hydrocarbon potential in Cretaceous sediments in the Western Bredasdorp sub-basin in the Outeniqua basin South Africa. MSc Thesis, University of Western Cape.
2. Abbaszadeh, M. & Shariatipour, S., 2018. Investigating the impact of aquifer parameters on carbon dioxide dissolution in saline aquifers. Available at: https://doi.org/10.20944/preprints201807.0603.v1
3. Afolayan, B.A., Mackay, E. & Opuwari, M., 2023. Dynamic modelling of geological carbon storage in an oil reservoir, Bredasdorp Basin, South Africa. Scientific Reports, 13, p.16573. https://doi.org/10.1038/s41598-023-43773-9.
4. Afolayan, B.A., Mackay, E. & Opuwari, M., 2023. 3D Static Modelling and CO_2 Static Storage Estimation of the Hydrocarbon-Depleted Charis Reservoir, Bredasdorp Basin, South Africa. Natural Resources Research. Available at: https://doi.org/10.1007/s11053-023-10180.
5. Ahmad, K.M., 2019. The role of flow rate and fluid alkalinity on fine particle movement and influencing the petrophysical properties of reservoir sandstone. Passer Journal of Basic and Applied Sciences, 1(2), pp.10-14. https://doi.org/10.24271/psr.05.
6. Agartan, E., Gaddipati, M., Yip, Y., Savage, B. & Ozgen, C., 2018. CO_2 storage in depleted oil and gas fields in the Gulf of Mexico. International Journal of Greenhouse Gas Control, 72, pp.38–48. https://doi.org/10.1016/j.ijggc.2018.02.022.
7. AlKharraa, H., Wolf, K., Kwak, H., Deshenenkov, I., Al-Duhailan, M., Mahmoud, M. & Zitha, P.L., 2023. A characterization of tight sandstone: effect of clay mineralogy on pore-framework. SPE International Conference, January 24, 2023. https://doi.org/10.2118/212638-ms.
8. Ambrose, W.A., et al., 2008. Geologic factors controlling CO_2 storage capacity and permanence: case studies based on experience with heterogeneity in oil and gas reservoirs applied to CO_2 storage. Environmental Geology, 54(8), pp.1619–1633.
9. Baiyegunhi, O.T., Liu, K., Gwavava, O., Wagner, N. & Baiyegunhi, C., 2020. Geochemical evaluation of the Cretaceous mudrocks and sandstones (Wackes) in the Southern Bredasdorp Basin, offshore South Africa: Implications for hydrocarbon potential. Minerals, 10, p.595. https://doi.org/10.3390/min10070595.
10. Bachu, S., 2000. Sequestration of CO_2 in Geological Media: Criteria and Approach for Site Selection in Response to Climate Change. Energy Conversion and Management, 41, pp.953–970.
11. Bachu, S., 2003. Screening and Ranking of Sedimentary Basins for Sequestration of CO_2 in Geological Media in Response to Climate Change. Environmental Geology, 44(3), pp.277–289.
12. Bachu, S., Bonijoly, D., Bradshaw, J., Burruss, R., Holloway, S., Christensen, N.P. & Mathiassen, O.M., 2007. CO_2 Storage Capacity Estimation: Methodology and Gaps. International Journal of Greenhouse Gas Control, 1(4), pp.430–443.

13. Bailey, S.W., Brindley, G.W., Kodama, H. & Martin, R.T., 1979. Report of the Clay Minerals Society Nomenclature Committee for 1977 and 1978. Clays and Clay Minerals, 27, pp.238–239.
14. Baouche, R. & Kamel, B., 2017. Prediction of permeability and porosity from well log data using the nonparametric regression with multivariate analysis and neural network, Hassi R'Mel Field, Algeria. Egyptian Journal of Petroleum, 26(3), pp.763–778.
15. Belhaj, H.A., 2023. Tight Oil Reservoirs. Characterization, Modelling, and Field Development. Volume 1 in Unconventional Reservoir Engineering Series. Gulf Professional Publishing, pp.85–155. Available at: https://doi.org/10.1016/B978-0-12-820269-2.00001-9.
16. Bennion, D.B., Thomas, F.B. & Bietz, R.F., 1996. Determination of initial fluid saturations—A key factor in bypassed pay determination. Proceedings of the SPE Annual Technical Conference and Exhibition, pp.3–5.
17. Burden, P.L.A., 1992. Soekor partners explore possibilities in the Bredasdorp Basin off South Africa. Oil and Gas Journal, 90(51), pp.109–112.
18. Burden, P.L.A. & Davies, C.P.N., 1997. Exploration to first production on block 9 off South Africa. Oil and Gas Journal, pp.92–98.
19. Broad, D.S., Jungslager, E.H.A., McLachlan, I.R. & Roux, J., 2006. Offshore Mesozoic basins. In: Johnson, M.R., Anhaeusser, C.R. & Thomas, R.J., eds. The geology of South Africa. Geological Society of South Africa, Pretoria: Johannesburg/Council for Geoscience, pp.553–571.
20. Brown, L.F., Brink, J.M., Doherty, G.J., Jollands, S., Jungslager, A., Keenan, E.H.A., et al., 1995. Sequence stratigraphy in offshore South African divergent basins. Studies in Geology, vol. 41. United States: American Association of Petroleum Geologists, pp.83–131.
21. Chabangu, N., Beck, B., Hicks, N., Botha, G., Viljoen, J., Davids, S. & Cloete, M., 2014. The investigation of CO_2 storage potential in the Zululand Basin in South Africa. Energy Procedia, 63, pp.2789–2799.
22. Cloete, M., 2010. Atlas on geological storage of carbon dioxide in South Africa. Pretoria: Council for Geoscience, South Africa.
23. Crain, E.R., 2013. Crain's Petrophysical Handbook. Available at: <www.spec2000.net/14-Swxplot.htm> [Accessed date: 31 August 2022].
24. Crain, E.R., 2014. Crain's Petrophysical Handbook. Available at: <www.spec2000.net/09-corePerm.htm> [Accessed date: 31 August 2022].
25. Connor, S., 2016. Petrophysics: A practical guide. John Wiley & Sons Ltd., UK.
26. Dahmen, T., Engstler, M., Pauly, C., Trampert, P., Jonge, N. d., Mücklich, F. & Slusallek, P., 2016. Feature adaptive sampling for scanning electron microscopy. Scientific Reports, 6(1). https://doi.org/10.1038/srep25350.
27. De Wit, M.J. & Ransome, I.G., 1992. Regional inversion tectonics along the southern margin of Gondwana. In: De Wit, M.J. & Ransome, I.G., eds. Inversion tectonics of the Cape Fold Belt, Karoo, and Cretaceous Basins of Southern Africa. Rotterdam, pp.15–22.
28. Dingle, R.V., Siesser, W.G. & Newton, A.R., 1983. Mesozoic and Tertiary Geology of Southern Africa. A.A. Balkema/Rotterdam, pp.99–106.

29. Djebbar, T. & Donaldson, E.C., 1999. Theory and practice of measuring reservoir rock and fluid transportation properties. Butterworth-Heinemann, USA.
30. Djebbar, T. & Donaldson, E.C., 2015. Petrophysics: Theory and Practice of Measuring Reservoir Rock and Fluid Transport Properties. 4th ed. Gulf Professional Publishing, UK. ISBN 978-0-12-803188-9.
31. DOE, 2008. Carbon Sequestration Atlas of the United States and Canada, Second Edition: Appendix A − Methodology for Development of Carbon Sequestration Capacity Estimates. National Energy Technology Laboratory, United States Department of Energy, Office of Fossil Energy.
32. Evenick, J.C., 2008. Introduction to well logs and subsurface maps. PenWell Corporation, Oklahoma.
33. Fadipe, O.A., 2009. Facies, depositional environments, and reservoir properties of the Albian age gas-bearing sandstone of the Ibhubesi oil field, Orange basin, South Africa. MSc Thesis. University of the Western Cape, pp.10–20.
34. Gaus, I., 2010. Role and impact of CO_2-rock interactions during CO_2 storage in sedimentary rocks. International Journal of Greenhouse Gas Control, 4, pp.73–89.
35. Gauteplass, J., Almenningen, S. & Ersland, G., 2020. Storing CO_2 as a solid hydrate in shallow aquifers: electrical resistivity measurements in hydrate-bearing sandstone. E3S Web of Conferences, 146, 05002. https://doi.org/10.1051/e3sconf/202014605002.
36. Gibson-Poole, C.M., Edwards, S., Langford, R.P. & Vakarelov, B., 2008. Review of geological storage opportunities for carbon capture and storage (CCS) in Victoria. PESA East Australasian Basins Symposium III, pp.1–20.
37. Glover, P., 2001. Petrophysics M.Sc. Course Notes.
38. Grobe, M., Pashin, J.C. & Dodge, R.L., 2009. Carbon dioxide sequestration in geological media: state of the science. AAPG Studies in Geology, 59.
39. Hartman, D.J. & Coalson, E.B., 1990. Evaluation of the Morrow Sandstones in the Sorrento Field, Cheyenne County, Colorado. RMAG Symposium, 91.
40. Hicks, N., Viljoen, J.H.A., Reddering, J.S.V., Davids, S. & Cloete, M., 2012. Storage potential, capacity estimate, and area selection for carbon dioxide storage in the Algoa Basin, South Africa. South Africa-EU Cooperation on Carbon Capture and Storage (SAfECCS). Unpublished Report, Council for Geoscience/Petroleum Agency SA, pp.161.
41. Hicks, N., Davids, S., Beck, B. & Green, A., 2014. Investigation of CO_2 storage potential of the Durban Basin in South Africa. Energy Procedia, 63, pp.5200–5210.
42. Jensen, J.L., Ayers, W.B. & Blasingane, T.A., 2013. Introduction to shaly sand analysis. Department of Petroleum Engineering, Texas A&M University.
43. Lake, L.W., 1989. Enhanced Oil Recovery. Prentice Hall Inc., Old Tappan, New Jersey, pp.361–371, Chapter 9.
44. Lehmann, K., 2010. Environmental Corrections to Gamma-ray Log Data: Strategies for Geophysical Logging with Geological and Technical Drilling. Journal of Applied Geophysics, 70(1), pp.17–26.

45. Liro, L.M. & Dawson, W.C., 2000. Reservoir systems of selected basins of the South Atlantic. In: Mello, M.R. & Katz, B.J., eds. Petroleum systems of South Atlantic margins. Volume 73.
46. Liu, H., 2017. Principles and Applications of Well Logging. Petroleum Industry Press, Beijing, China.
47. Munish, K. & Lauderdale-Smith, G., 2024. Petrophysical considerations for CO_2 capture and storage. Petrophysics, 65, pp.51–69. https://doi.org/10.30632/PJV65N1-2024a3.
48. Maclear, L.G.A., 2001. The hydrogeology of the Uitenhage Artesian Basin with reference to the Table Mountain Group Aquifer. Water SA, 27, pp.499–505.
49. Magoba, M., 2014. Petrophysical evaluation of sandstone reservoirs of wells E-AH1, E-BW1, and E-L1 in the Central Bredasdorp Basin, offshore South Africa. Department of Earth Sciences, University of the Western Cape.
50. Magoba, M., Opuwari, M. & Liu, K., 2024. The effect of diagenetic minerals on the petrophysical properties of sandstone reservoirs: A case study of the upper shallow marine sandstones in the Central Bredasdorp Basin, offshore South Africa. Minerals, 14, p.396. https://doi.org/10.3390/min14040396.
51. Maseko, P.P., 2016. Petrophysical evaluation and characterization of sandstone reservoirs of the western Bredasdorp Basin, South Africa, for well D-D1 and E-AP1. MSc Thesis. University of Western Cape, South Africa, pp.1.
52. Mateos-Redondo, F., Kovács, T. & Berrezueta, E., 2018. Petrographic and petrophysical characterization of detrital reservoir rocks for CO_2 geological storage. Northern Spain.
53. McMillan, I.K., Brink, G.J., Broad, D.S. & Maier, J.J., 1997. Late Mesozoic sedimentary basins off the south coast of South Africa. In: Selley, R.C., ed. Sedimentary Basins of the World—African Basins. Amsterdam: Elsevier Science B.V., pp.319–376.
54. McMillan, I.K., 2003. Foraminiferal defined biostratigraphic episodes and sedimentation pattern of the Cretaceous drift succession (Early Barremian to Late Maastrichtian) in seven basins on the South African and southern Namibian continental margin. South African Journal of Science, 99, pp.537–576.
55. National Grid, 2022. What is Carbon Capture and Storage? Available at: https://www.nationalgrid.com/stories/energy-explained/what-is-ccs-how-does-it-work (Accessed: 23 May 2022).
56. Odin, G.S. & Matter, A., 1981. De glauconiarum origine. Sedimentology, 28, pp.611–641.
57. Opuwari, M., 2010. Petrophysical evaluation of the Albian age gas-bearing sandstone reservoir of the O-M field, Orange Basin, South Africa. PhD Thesis. University of the Western Cape, South Africa.
58. Opuwari, M., Magoba, M., Dominick, N. & Waldmann, N., 2021. Delineation of sandstone reservoir flow zones in the central Bredasdorp Basin, South Africa, using core samples. Natural Resources Research, 1–22.
59. Parker, I., 2014. Petrophysical evaluation of sandstone reservoirs of the central Bredasdorp Basin, Block 9, Offshore South Africa. MSc Thesis. University of the Western Cape.

60. Pentland, C.H., Iglauer, S., Gharbi, O., Okada, K. & Suekane, T., 2012. The influence of pore space geometry on the entrapment of carbon dioxide by capillary forces. Society of Petroleum Engineers.
61. Rider, M., 2002. The Geological Interpretation of Well Logs. 2nd ed. Rider-French Consulting, Scotland, p.1.
62. Rissman, J., Bataille, C. & Aden, N., 2020. Technologies and policies to decarbonize global industry: Review and assessment of mitigation drivers through 2070. Applied Energy, 266.
63. Pestitschek, B., Gier, S., Essa, M. & Kurzwell, H., 2012. Effects of weathering on glauconite: Evidence from the Abu Tartur Plateau, Egypt. Clays and Clay Minerals, 60(1), pp.76–88.
64. Petroleum Agency SA, 2004/5. South African Exploration Opportunities. South African Agency for Promotion of Petroleum Exploration and Exploitation, Cape Town, pp.27.
65. Petroleum Agency SA, 2005. Petroleum Exploration Information and Opportunities: Petroleum Agency South Africa Brochure.
66. Petroleum Agency SA, 2008. Petroleum Exploration: Information and Opportunities 2008. Petroleum Agency SA, 30 pp.
67. Raza, A., Rezaee, R., Gholami, R., Bing, C.H., Nagarajan, R. & Hamid, M.A., 2016. A screening criterion for the selection of suitable CO_2 storage sites. Journal of Natural Gas Science and Engineering.
68. Rider, M., 2002. The Geological Interpretation of Well Logs. 2nd ed. Rider-French Consulting, Scotland.
69. Saffou, E., Raza, A., Gholami, R., Croukamp, L., Elingou, W.R., Donker, J.B., Opuwari, M., Manzi, M.S.D. & Durrheim, R.J., 2020. Geomechanical characterization of CO_2 storage sites: A case study from a nearly depleted gas field in the Bredasdorp Basin, South Africa. Journal of Natural Gas Science and Engineering, 81, p.103446.
70. Sanderson, I.D., 1984. Recognition and significance of inherited quartz overgrowths in quartz arenites. Journal of Sedimentary Research, 54(2), pp.473–486. doi: https://doi.org/10.1306/212F844A-2B2411D78648000102C1865D.
71. Serra, O., 1984. Fundamentals of Well Log Interpretation: The Acquisition of Logging Data. London: Elsevier Science Ltd.
72. Somma, M., 2021. The Effects of Carbon Dioxide on Air Pollution. Available at: https://sciencing.com/list-5921485-effects-carbon-dioxide-air-pollution.html (Accessed: 9 March 2022)
73. Schalkwyk, H.J.M., 2005. Assessment Controls on Reservoir Performance and The Effects of Granulation Seam Mechanics in the Bredasdorp Basin, South Africa. MSc Thesis. University of the Western Cape, South Africa, p.128.
74. Schlumberger Ltd., 2013. Grain Density Classification. Houston, Texas.
75. Snow, C., 2021. Danomics: Petrophysics. Log Unit Conversions and Splicing. Available at: https://www.danomics.com/help/log-unit-conversions-and-splicing/.
76. Sonibare, W.A., 2015. Structure and Evolution of Basin and Petroleum Systems Within a Transform-related Passive Margin Setting: Data-based insights from

Crust-scale 3D Modeling of the Western Bredasdorp Basin, offshore South Africa. PhD Thesis. University of Stellenbosch, pp.16–44.
77. Tinker, J., De Wit, M. & Brown, R., 2008. Linking source and sink: Evaluating The Balance Between Onshore Erosion and Offshore Sediment Accumulation Since Gondwana Breakup, South Africa. Tectonophysics, 455(1), pp.94–103.
78. Turner, J.R., Grobber, N. & Sontundu, S., 2000. Geological Modeling of the Aptian and Albian Sequences Within Block 9, Bredasdorp Basin, Offshore South Africa. In: Kisters, A.F.M. & Thomas, R.J., eds. Journal of African Earth Sciences, Geocongress: A New Millennium on Ancient Crust, 27th Earth Science Congress of the Geological Society of South Africa, p.80.
79. Uchechukwu, E., 2014. Pore Pressure Prediction: A Case Study of Sandstone Reservoirs, Bredasdorp Basin, South Africa. MSc Thesis. University of the Western Cape, Cape Town, p.2.
80. Viljoen, J.H.A., Hicks, N., Botha, G.A., Davids, S. & Cloete, M., 2012. An effective CO_2 Storage Capacity Assessment of the Zululand Basin, South Africa. South African Centre for Carbon Capture and Storage, Unpublished Report, Council for Geoscience/Petroleum Agency SA, 115 pp.
81. Wei, N., Gill, M., Crandall, D., McIntyre, D., Wang, Y., Bruner, K., Li, X. & Bromhal, G., 2014. CO_2 Flooding Properties of Liujiagou Sandstone: Influence of Sub-core Scale Structure Heterogeneity. Greenhouse Gases: Science and Technology, 4(3), pp.400–418.
82. Winland, H.D., 1972. Oil Accumulation in Response to Pore Size Changes, Weyburn Field, Saskatchewan. Amoco Production Research Report No. F72-G-25.

Appendices

Appendix A Conventional Core Analysis Results

Table 4.7 Results Obtained from the Conventional Core Analysis of Well F-A10.

Depth (m)	Porosity (%)	Permeability (mD)	Sw (%)	Calcite (%)	Dolomite (%)
2719.00	0.166	168.00	0.30	0	2
2719.55	0.191	91.00			
2719.85	0.185	278.00			
2720.12	0.176	81.00			
2720.24	0.166	271.00	0.38	0	2
2720.64	0.18	293.00			
2720.94	0.183	298.00			
2721.03	0.177	456.00	0.35	0	2
2721.49	0.191	231.00			
2721.79	0.192	436.00			
2721.83	0.191	494.00	0.45	0	1
2722.35	0.183	173.00			
2722.65	0.181	263.00			
2722.93	0.192	306.00	0.36	1	1
2722.94	0.175	348.00			
2723.30	0.168	126.00			
2723.64	0.188	338.00			
2723.95	0.185	491.00			
2724.22	0.181	210.00			
2724.23	0.186	282.00	0.47	1	1
2724.44		411.00			
2724.65	0.169	128.00			
2724.95	0.179	149.00			
2724.97	0.174	513.00	0.40	0	2
2725.37	0.182	210.00			

2725.67	0.186	350.00			
2725.80	0.179	241.00	0.42	0	1
2726.14	0.195	577.00			
2726.44	0.186	313.00			
2726.74	0.177	168.00			
2727.00	0.175	222.00			
2727.03	0.177	511.00	0.38	0	2
2727.40	0.171	136.00			
2727.66	0.165	279.00			
2727.71	0.174	306.00	0.40	1	1
2728.15	0.18	302.00			
2728.45	0.175	158.00			
2728.70	0.185	445.00	0.36	0	1
2729.04	0.186	638.00			
2729.29	0.184	428.00			
2729.54	0.181	341.00			
2729.79	0.177	362.00			
2730.08	0.177	924.00	0.40	0	2
2730.52	0.166	294.00			
2730.73	0.165	416.00	0.34	1	1
2730.79	0.155	130.00			
2731.19	0.176	745.00			
2731.44	0.181	486.00			
2731.62	0.188	324.00	0.40	0	1
2731.95	0.18	298.00			
2732.20	0.173	278.00			
2732.45	0.197	440.00			
2732.51	0.175	508.00	0.38	0	2
2732.99	0.174	261.00			

2733.24	0.191	363.00			
2733.50	0.173	174.00	0.38	1	1
2733.95	0.144	36.00			
2734.20	0.162	215.00			
2734.45	0.178	425.00			
2734.71	0.158	312.00	0.38	1	1
2734.75	0.139	19.00			
2735.12	0.166	247.00			
2735.37	0.164	201.00			
2735.67	0.191	473.00			
2735.92	0.18	435.00			
2736.00	0.182	269.00	0.45	1	1
2736.35	0.18	290.00			
2736.60	0.174	323.00			
2736.74	0.162	240.00	0.38	0	2
2737.14	0.165	241.00			
2737.39	0.171	317.00			
2737.64	0.17	335.00			
2737.88	0.17	351.00			
2737.89	0.156	313.00	0.36	0	1
2738.08					
2738.10		237.00			
2738.30	0.168	340.00			
2738.55	0.171	388.00			
2738.80	0.165	228.00			
2738.92	0.165	73.00	0.34	1	1
2739.39	0.152	69.00			
2739.64	0.117	8.6			
2739.94	0.146	114.00			

2740.19	0.162	171.00			
2740.27	,0.159	202.00	0.35	1	1
2740.39					
2740.45		89.60			
2740.58	0.160	163.00			
2740.83	0.160	83.00			
2741.08	0.159	78.00			
2741.20	0.167	93.00	0.11	0	3
2741.36		81.70			
2741.55	0.144	55.00			
2741.80	0.149	51.00			
2742.05	0.150	74.00			
2742.29	0.146	58.00	0.41	0	2
2742.65	0.140	24.00			
2742.90	0.140	33.00			
2743.14	0.154	61.00	0.37	0	2
2743.15	0.147	61.00			
2743.31		30.10			
2743.50	0.141	67.00			
2743.75	0.150	73.00			
2744.00	0.136	21.00	0.33	1	1
2744.32	0.161	86.00			
2744.57	0.150	72.00			
2744.82	0.150	103.00			
2745.07	0.155	88.00			
2745.23	0.143	54.80			
2745.41	0.154	91.00			
2745.66	0.149	46.00			
2745.86	0.141	60.00	0.37	1	1

2746.18	0.153	49.00			
2746.43	0.151	52.00			
2746.68	0.131	16.00			
2746.71	0.164	66.00	0.36	1	1
2746.85		31.50			
2747.42	0.141	35.00			
2747.67	0.138	21.00			
2747.92	0.123	23.00	0.32	1	1
2748.55	0.136	27.00			
2748.69	0.131	40.00	0.32	1	2
2748.92		41.30			
2749.11	0.127	11.00			
2749.36	0.142	37.00			
2749.61	0.144	33.00			
2749.86	0.144	62.00			
2750.11	0.143	35.00			
2750.16	0.133	30.00	0.39	0	2
2750.32		45.70			
2750.47	0.126	14.00			
2750.74		30.00	0.32	0	2
2750.88		19.40			
2751.09	0.121	5.3			
2751.34	0.135	21.00			
2751.63	0.126	17.00	0.40	1	2
2751.73	0.131	12.00			
2751.93	0.103	2.2			
2752.23	0.134	21.00			
2752.43	0.143	37.00			
2752.73	0.131	21.00			

2752.84	0.139	17.00	0.41	1	2
2753.01		13.40			
2753.19	0.129	15.00			
2753.44	0.130	16.00			
2753.67	0.129	27.00			
2754.00	0.142	15.00			
2754.25	0.135	50.00			
2754.50	0.140	27.00	0.42	1	2
2754.75	0.140	35.00			
2754.98	0.15	34.00	0.40	1	3
2755.30	0.135	16.00			
2755.55	0.133	17.00			
2756.03	0.143	37.00			
2756.23	0.146	66.00			
2756.53	0.136	28.00			
2756.56	0.135	8.50	0.62	1	2
2756.88	0.136	22.00			
2757.13	0.133	22.00			
2757.29	0.137	53.00	0.47	1	2
2757.60	0.143	41.00			
2757.85	0.128	15.00			
2758.10	0.107	3.10			
2758.30	0.085		0.69	0	4
2758.46	0.065				
2758.67	0.096	0.83			
2758.92	0.115	3.7			
2759.17	0.104	0.91			
2759.30	0.115	2.30	0.58	1	1
2759.71	0.115	2.0			

2759.96	0.125	4.6			
2760.21	0.131	4.2			
2760.23	0.135	4.9	0.67	1	3
2760.34					
2760.40	0.126				
2760.53	0.115	1.6			
2760.78	0.117	3.8			
2761.03	0.115	1.7			
2761.28	0.104	1.0			
2761.51	0.088	0.23	0.52	0	3
2761.53	0.098	0.75			
2761.94	0.099	0.54			
2762.19	0.088	0.39			
2762.44	0.092	0.39			
2762.55	0.126	3.9	0.74	0	3
2762.84	0.119	3.7			
2763.09	0.125	8.1			
2763.34	0.119	3.9			
2763.59	0.122	4.6			
2763.69	0.112	2.00	0.55	1	2
2764.04	0.095	0.6			
2764.29	0.107	0.91			
2764.52	0.123	1.4	0.76	0	3
2764.88	0.102	0.54			
2765.13	0.098	0.46			
2765.23	0.079	0.20	0.47	3	2
2765.64	0.098	1.0			
2765.89	0.084	0.39			
2766.09	0.105	0.75	0.71	1	3

2766.40	0.100	1.3			
2766.65	0.058	0.46			
2766.90	0.103	1.0			
2767.09	0.093	0.81	0.50	7	1
2767.42	0.105	0.91			
2767.69	0.106	1.7			
2767.94	0.091	0.54			
2768.04	0.141	0.26	0.73	0	4
2768.49	0.091	0.46			
2768.74	0.071	0.26			
2768.99	0.088	0.39			
2769.22	0.088	0.26	0.59	1	3
2769.61	0.086	0.54			
2769.86	0.106	0.75			
2770.11	0.105	1.1			
2770.28	0.109	0.68	0.71	0	3
2770.63	0.101	0.60			
2770.90	0.092	0.39			
2771.13	0.082	0.26	0.51	1	3
2771.48	0.106	2.1			
2771.73	0.098	0.54			
2771.98	0.104	0.91			
2772.23	0.094	0.39			
2772.48	0.069	0.26			
2772.52	0.106	0.54	0.80	20	0
2772.83	0.101	0.68			
2773.08	0.093	0.54			
2773.33	0.105	0.60	0.52	0	2
2773.66	0.116	1.0			

2773.91	0.106	0.60			
2774.16	0.108	0.175			

Table 4.8 Results obtained from the conventional core analysis of Well F-A13.

Depth	Porosity (%)	Permeability (mD)	Sw (%)	Calcite (%)	Dolomite (%)	Grain density (g/cc)
2613.00	0.172	155	0.41	0	1	
2613.67	0.193	667	0.38	1	1	2.67
2613.92	0.219	898				
2614.17	0.216	644				
2614.38	0.205	649				
2614.41	0.105	568				
2614.92	0.221	1156				
2615.15	0.217	2190				
2615.40	0.212	1466				
2615.43	0.205	829	0.36	0	1	
2615.94	0.220	1481				
2616.19	0.210	1366				
2616.38	0.217	1572	0.39	0	1	2.67
2616.93	0.212	1062				
2617.18	0.207	923				
2617.33	0.211	826	0.44	0	1	
2617.89	0.231	1436				
2618.14	0.193	553				
2618.30	0.187	625	0.38	0	0	2.67
2618.77	0.209	917				
2619.04	0.207	1178				
2619.29	0.176	198				
2619.46	0.217	1395	0.41	1	0	
2619.80	0.214	1340				
2620.10	0.145	50				
2620.40	0.175	480				
2620.65	0.156	85	0.42	1	1	2.69
2621.27	0.113	4.2				
2621.44	0.206	296	0.34	1	0	
2621.94	0.215	711				
2622.19		802				
2622.36	0.209	757	0.43	0	1	2.68
2623.10	0.220	441				
2623.29	0.223	983	0.37	0	1	
2623.75	0.197	429				
2624.00	0.199	1516				
2624.25	0.216	1316				

2624.45	0.210	916	0.41	0	1	2.68
2624.97	0.207	585				
2625.22	0.201	406				
2625.38	0.207	359	0.39	0	1	
2625.94	0.196	599				
2626.19	0.207	544				
2626.44	0.203	508	0.41	1	0	2.69
2626.48	0.199	698				
2627.03	0.216	475				
2627.32	0.200	701				
2627.39	0.223	874	0.40	0	1	
2627.82	0.215	554				
2628.07	0.205	340				
2628.32	0.207	300				
2628.43	0.181	213	0.38	0	1	2.68
2629.12	0.197	633				
2629.37	0.200	408				
2629.50	0.181	235	0.39	0	1	
2629.93	0.203	574				
2630.18	0.206	808				
2630.38	0.188	414	0.36	1	1	2.69
2630.85	0.192	412				
2631.10	0.208	668				
2631.35	0.187	295				
2631.40	0.204	595	0.39	0	1	
2631.71	0.180	184				
2631.76	0.196	465	0.34	0	1	
2632.18	0.184	204				
2632.43	0.149	35				
2632.68	0.191	276				
2632.93	0.204	434				
2633.03	0.213	840	0.40	0	1	
2633.59	0.207	547				
2633.84	0.210	664	0.37	0	2	2.70
2634.00	0.180	255				
2634.54	0.176	179				
2634.67	0.175	227				
2634.79	0.183	119	0.37	0	5	
2635.29	0.164	54				
2635.54	0.170	78				
2635.65	0.182	894	0.40	1	1	2.68
2636.15	0.165	53				
2636.40	0.165	42				
2636.67	0.158	15				
2636.92	0.135	38				
2637.03	0.155	27	0.37	0	2	

2637.51	0.149	32				
2637.76	0.144	29				
2637.95	0.164	248	0.29	0	1	2.68
2638.26	0.131	4.7				
2638.51	0.128	2.4				
2638.76	0.139	7.2				
2639.01	0.135	5.2				
2639.26	0.128	4.1				
2639.38	0.195	587	0.36	1	8	
2639.90	0.130	17				
2640.15	0.173	128				
2640.40	0.136	19				
2640.52	0.130	10	0.38	0	1	2.69
2641.02	0.172	42				
2641.27	0.170	46				
2641.42	0.168	42	0.37	0	1	
2641.90	0.182	148				
2642.15	0.178	112				
2642.40	0.149	15				
2642.67	0.131	6.8				
2642.85	0.147	14	0.40	0	1	2.69
2643.39	0.140	22				
2643.64	0.153	26				
2643.89	0.119	2.8				
2643.94	0.128	3.7	0.26	1	13	
2644.48	0.137	2.9				
2644.73	0.156	10				
2644.78	0.149	26	0.36	1	4	2.71
2645.54	0.111	0.52				
2645.79	0.121	3.1				
2645.86	0.126	1.2	0.30	25	3	
2646.50	0.159	21				
2646.61	0.160	42	0.30	0	1	
2647.22	0.138	7.2				
2647.47	0.185	159				
2647.60	0.175	37	0.34	1	7	
2648.23	0.119	3.7				
2648.48	0.129	7.4				
2648.63	0.140	19	0.34	1	4	2.68
2648.89	0.137	7.1				
2649.39	0.136	15				
2649.44	0.192	616	0.33	0	2	
2650.03	0.176	81	0.35	1	3	
2650.20	0.206	552		1	3	
2650.65	0.174	68		0	9	
2650.90	0.199	272		10	18	

2651.10	0.127	243	0.43	0	9	2.70
2651.35	0.174	98				
2651.70	0.190	307				
2651.95	0.133	67				
2652.02	0.166	24	0.34	10	18	
2652.35	0.175	57		1	3	
2652.90	0.185	188		0	2	
2653.05	0.192	958	0.34	1	2	2.69
2653.65	0.219	841		0	2	
2653.90	0.220	848		1	2	
2654.01	0.204	968	0.36	0	1	
2654.50	0.194	191		1	9	
2654.75	0.183	109		1	2	
2654.91	0.171	454	0.36	0	6	2.70
2655.25	0.120	17		0	2	
2655.60	0.212	636		0	5	
2655.85	0.194	504		0	4	
2655.99	0.148	54	0.34	1	3	
2656.10	0.166	182		0	8	
2656.60	0.202	954		1	2	
2656.85	0.209	1032		0	5	
2656.94	0.210	1185	0.38	0	2	2.69
2657.55	0.215	1142				
2657.80	0.209	989				
2658.00	0.195	1142	0.36	0	2	
2658.05	0.215	1109				
2658.60	0.177	288				
2658.85	0.160	107				
2659.01	0.196	729	0.31	1	2	2.69
2659.65	0.204	722				
2659.90	0.219	668				
2660.04	0.184	397	0.32	1	9	
2660.60	0.171	273				
2660.88	0.171	317				
2661.13	0.165	106				
2661.16	0.171	253	0.33	1	2	2.69
2661.60	0.201	419				
2661.85	0.204	644				
2661.96	0.192	372	0.37	0	2	
2662.95	0.203	656				
2663.13	0.192	494	0.35	0	6	2.70
2663.68	0.207	447				
2663.93	0.175	39				
2664.18	0.204	365				
2664.19	0.193	290	0.34	0	5	
2664.70	0.195	335				

2664.95	0.190	380				
2665.08	0.182	385	0.35	0	4	2.69
2665.65	0.175	184				
2665.90	0.169	182				
2665.97	0.174	296	0.32	0	8	
2666.55	0.181	196				
2666.80	0.177	278				
2666.94	0.158	79	0.32	1	2	2.70
2667.50	0.111	3.6				
2667.75	0.155	143				
2667.93	0.162	23	0.34	0	5	
2668.00	0.162	43				
2668.43	0.175	150		1	8	
2668.63	0.152	60	0.32	1	8	
2668.90	0.133	21		0	5	
2669.15	0.098	2		0	4	
2669.40	0.152	84		0	3	
2669.75	0.162	124	0.30	0	5	2.71
2669.93	0.166	123		0	6	
2670.25	0.159	56		0	2	
2670.57	0.144	12	0.41	0	4	
2670.90	0.150	49		0	7	
2671.15	0.163	69		0	5	
2671.53	0.176	274	0.32	0	3	2.70
2671.85	0.167	44		0	4	
2672.10	0.168	78		0	2	
2672.35	0.173	136		0	6	
2672.61	0.180	189	0.37	0	6	
2672.95	0.123	15		0	2	
2673.20	0.156	84		1	2	
2673.78	0.129	19	0.35	0	2	2.69
2674.10	0.127	7.5		0	2	
2674.35	0.133	30		1	2	
2674.68	0.156	67	0.41	0	7	
2674.98	0.127	2.1		0	7	
2675.23	0.135	21		1	7	
2675.53	0.141	11	0.31	0	5	2.72
2675.83	0.139	10				
2676.08	0.144	63		15	2	
2676.42	0.133	15	0.35	0	4	2.69
2676.80	0.159	73				
2677.05	0.168	249				
2677.30	0.176	284				
2677.59	0.166	28	0.35	0	2	
2677.95	0.148	48				
2678.20	0.128	15	0.23	0	6	2.68

2678.70	0.114	2.6				
2678.76	0.129	15				
2679.10	0.128	9.0				
2679.35	0.149	39				
2679.63	0.133	16	0.33	0	2	2.69
2679.90	0.126	17				
2680.15	0.136	19				
2680.40	0.139	11				
2680.71	0.149	43	0.31	1	2	
2681.10	0.146	40				
2681.35	0.152	23				
2681.73	0.125	7.1	0.34	0	2	2.69
2682.05	0.117	5.7				
2682.35	0.142	30				
2682.82	0.166	156	0.33	1	2	
2683.10	0.167	17				
2683.37	0.175	246				
2683.89	0.157	227	0.39	0	7	2.67
2684.10	0.177	177				
2684.35	0.136	37				
2684.75	0.150	63				
2685.00	0.174	620				
2685.06	0.169	122	0.35	1	7	
2685.45	0.130	79				
2685.80	0.132	46				
2686.50	0.125	17	0.42	15	2	
2687.00	0.155	182	0.41	6	3	
2687.65	0.159	269		6	3	
2687.90	0.117	3.5				
2688.02	0.144	91	0.33	2	5	2.72
2688.65	0.112	2.7		9	3	
2688.90	0.159	191				
2688.95	0.151	205	0.39	9	3	
2689.45	0.118	36		1	2	
2689.70	0.141	18				
2689.95	0.111	2.7		9	4	
2689.96	0.148	20	0.37	13	4	2.74
2690.60	0.138	36				
2690.85	0.134	8.7		9	3	
2691.07	0.146	7.3	0.39	1	2	
2691.10	0.127	17		21	2	
2691.60	0.148	37		2	6	
2691.85	0.168	48		10	4	
2692.00	0.142	30	0.38	21	1	2.70
2692.55	0.069	0.03		10	2	
2692.80	0.111	2		5	9	

2692.87	0.121	4.4	0.37	9	4	
2693.36	0.047	0.04		2	7	
2693.61	0.049	0.04		8	7	
2693.87	0.110	1.3		2	9	
2693.89	0.104	17	0.40	20	2	2.73
2694.40	0.119	7.4		11	9	
2694.65	0.067	0.13				
2694.90	0.131	7.7				
2695.09	0.116	3.4	0.34	9	3	
2695.55	0.120	16				
2695.80	0.098	4.8				
2695.94	0.117	13	0.44	21	2	2.69
2696.05	0.100	5.2				
2696.55	0.107	17				
2696.80	0.130	35				
2697.05	0.140	31				
2697.07	0.141	46	0.36	2	6	
2697.75	0.148	20				
2697.99	0.154	4.2				
2698.00	0.125	8.0	0.39	10	4	2.73
2698.50	0.142	20				
2698.75	0.151	28				
2698.82	0.131	34	0.41	10	2	
2699.22	0.057	0.04				
2699.47	0.152	74				
2699.72	0.147	36				
2699.92	0.141	53	0.37	5	9	2.68
2700.35	0.049	0.04				
2700.60	0.122	3.8				
2700.85	0.135	14				
2700.88	0.140	26	0.44	2	7	
2701.45	0.113	3.4				
2701.70	0.053	0.03				
2701.84	0.145	51	0.41	8	7	2.72
2702.45	0.100	10				
2702.70	0.154	62				
2702.93	0.156	69	0.37	2	9	
2702.95	0.143	24				
2703.42	0.157	116				
2703.66	0.154	15				
2703.83	0.140	73	0.42	11	9	
2703.90	0.147	19				
2704.45	0.152	84	0.36	2	11	
2704.99	0.113	37		2	11	
2705.24	0.110	40		29	1	
2705.43	0.084	1.2		12	7	

2705.45	0.142	57	0.44	29	1	
2705.97	0.128	89		17	3	
2706.22	0.119	67		6	8	
2706.37	0.154	86	0.34	12	7	
2706.87	0.106	15		21	1	
2707.14	0.067	0.17		19	1	
2707.31	0.126	47		17	1	
2707.57	0.109	20		17	1	
2707.92	0.087	2.2		22	1	
2708.17	0.111	5.3		16	3	
2708.38	0.130	6.4		35	0	
2708.42	0.109	19	0.35	6	8	
2708.90	0.106	1.6		40	2	
2709.15	0.083	0.52		13	4	
2709.25	0.101	0.75	0.46	21	1	2.71
2709.65	0.087	0.75		38	1	
2709.90	0.092	1.3		37	0	
2710.15	0.067	0.24				
2710.40	0.072	0.29				
2710.45	0.096	0.68	0.56	19	1	
2711.00	0.106	4.4				
2711.25	0.108	4.3				
2711.41	0.127	10	0.31	17	1	2.72
2711.85	0.054	0.05				
2712.10	0.111	7.0				
2712.35	0.099	1.5				
2712.41	0.061	0.10	0.40	22	1	
2712.90	0.063	0.06				
2713.15	0.054	0.03				
2713.40	0.076	0.29				
2713.48	0.082	0.45	0.45	16	3	
2713.95	0.087	1.7				
2714.20	0.052	0.05				
2714.34	0.045	0.06	0.49	35	0	
2715.00	0.061	0.06				
2715.25	0.053	0.04				
2715.29	0.075	0.08	0.75	40	2	2.79
2715.80	0.048	0.04				
2716.05	0.06	0.60				
2716.30	0.108	5.2				
2716.35	0.096	0.23	0.37	13	4	
2716.55	0.072	0.47				
2717.00	0.107	6.4				
2717.25	0.089	0.083				
2717.32	0.075	0.03	0.74	38	1	2.78
2717.80	0.076	0.06				

2718.05	0.057	0.06				
2718.31	0.053	0.04				
2718.37	0.038	0.05	0.53	37	0	
2718.85	0.061	0.04				

Appendix B: Standalone Pickett Plots

Well E-AQ1

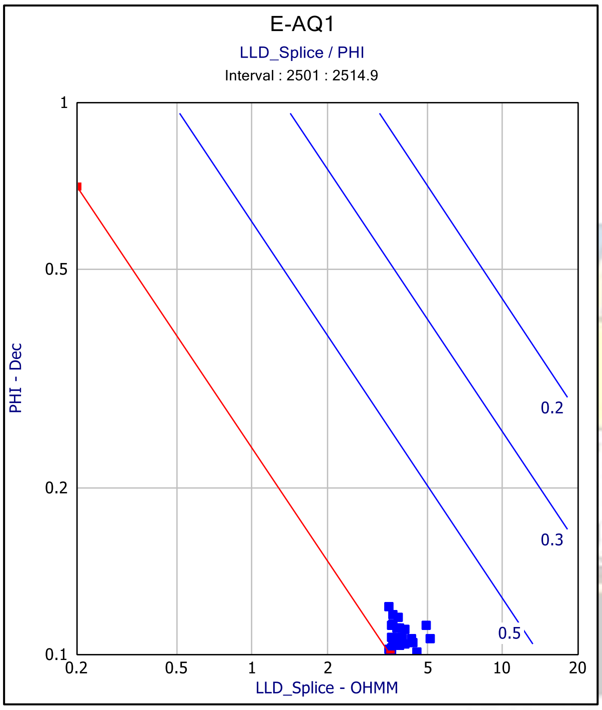

Well E-G2

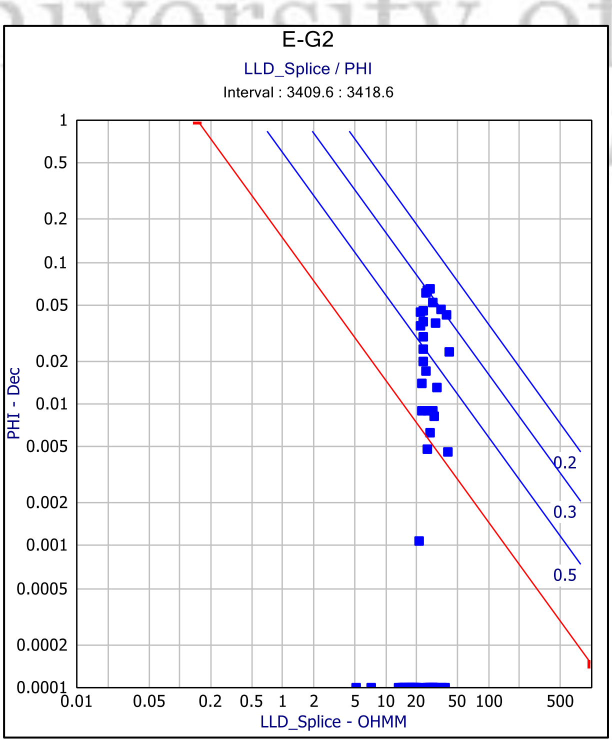

Well F-A10

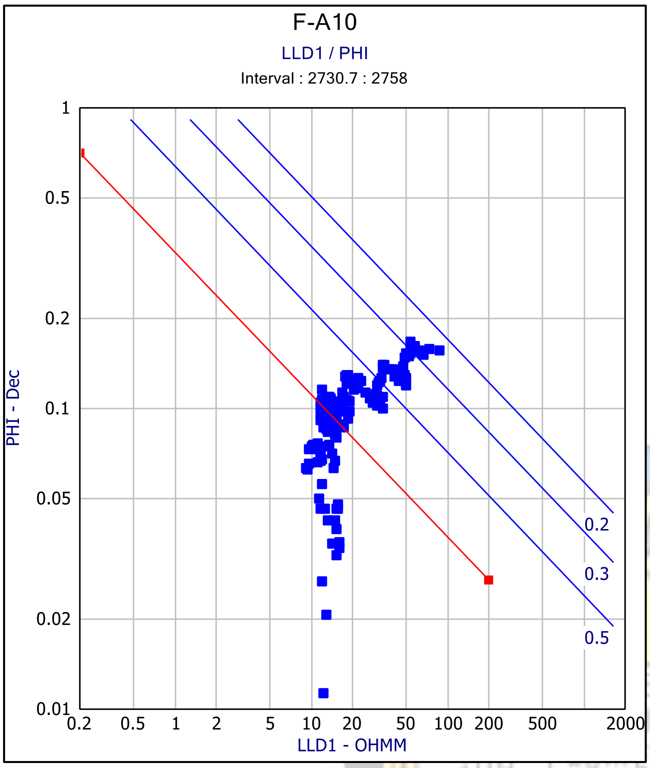

Well F-A13

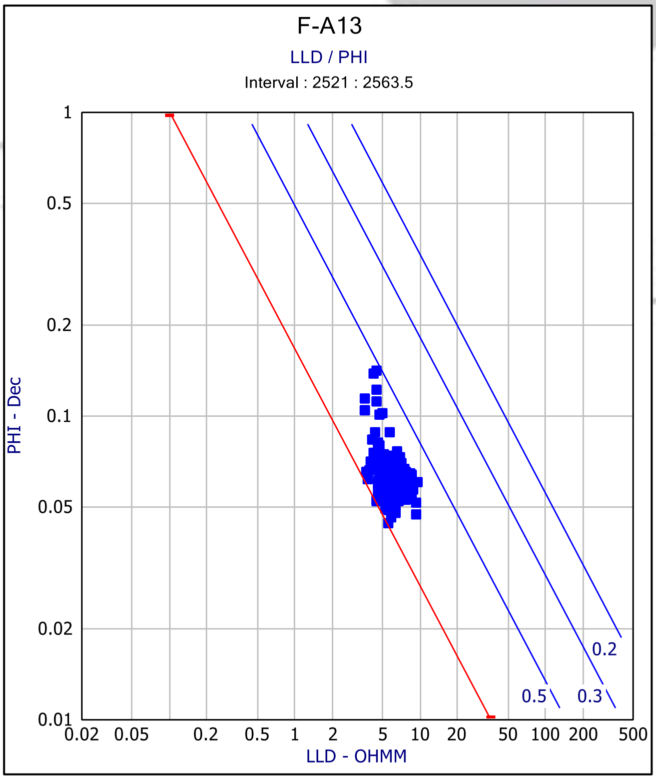

Appendix C Pore Throat size

Well E-AQ1

Depth	Porosity	Permeability	R35
2614.05	0.003	0.03	1.942292
2616.65	0.022	0.06	0.522035

Well E-G2

Depth	Porosity	Permeability	R35
3308.35	0.151	0.1	0.133464
3308.86	0.0094	0	0
3309.48	0.159	0.9	0.464609
3310.3	0.139	0.4	0.323927
3311.27	0.136	0.1	0.146091
3312.04	0.129	0.3	0.291741
3313.35	0.11	0.1	0.175484
3314.35	0.125	0.4	0.355043
3315.23	0.092	0	0
3317.33	0.114	0.1	0.170151
3318.22	0.151	0.5	0.343841
3319.27	0.126	0.6	0.447541

3320.06	0.092	0	0
3321.65	0.133	0.1	0.148933
3323.48	0.051	0	0

Well F-A10

Depth	Porosity	Permeability	R35
2719.00	0.166	168.00	9.689658
2719.55	0.191	91.00	5.985542
2719.85	0.185	278.00	11.86484
2720.12	0.176	81.00	5.998826
2720.24	0.166	271.00	12.83549
2720.64	0.18	293.00	12.53034
2720.94	0.183	298.00	12.47617
2721.03	0.177	456.00	16.49007
2721.49	0.191	231.00	10.35121
2721.79	0.192	436.00	14.97083
2721.83	0.191	494.00	16.18448
2722.35	0.183	173.00	9.061777
2722.65	0.181	263.00	11.70307
2722.93	0.192	306.00	12.15715
2722.94	0.175	348.00	14.20574
2723.30	0.168	126.00	8.097494
2723.64	0.188	338.00	13.12595
2723.95	0.185	491.00	16.57752
2724.22	0.181	210.00	10.25252
2724.23	0.186	282.00	11.90933
2724.44		411.00	
2724.65	0.169	128.00	8.131026
2724.95	0.179	149.00	8.459964
2724.97	0.174	513.00	17.93554
2725.37	0.182	210.00	10.20383
2725.67	0.186	350.00	13.52237
2725.80	0.179	241.00	11.22434
2726.14	0.195	577.00	17.41733
2726.44	0.186	313.00	12.66254
2726.74	0.177	168.00	9.167121
2727.00	0.175	222.00	10.90613
2727.03	0.177	511.00	17.63204
2727.40	0.171	136.00	8.340887
2727.66	0.165	279.00	13.1253
2727.71	0.174	306.00	13.23639
2728.15	0.18	302.00	12.75524
2728.45	0.175	158.00	8.929466
2728.70	0.185	445.00	15.64586
2729.04	0.186	638.00	19.24755
2729.29	0.184	428.00	15.36336

2729.54	0.181	341.00	13.63406
2729.79	0.177	362.00	14.39699
2730.08	0.177	924.00	24.97849
2730.52	0.166	294.00	13.46526
2730.73	0.165	416.00	16.60048
2730.79	0.155	130.00	8.842032
2731.19	0.176	745.00	22.11592
2731.44	0.181	486.00	16.79221
2731.62	0.188	324.00	12.80348
2731.95	0.18	298.00	12.65563
2732.20	0.173	278.00	12.57264
2732.45	0.197	440.00	14.7208
2732.51	0.175	508.00	17.74447
2732.99	0.174	261.00	12.05452
2733.24	0.191	363.00	13.50244
2733.50	0.173	174.00	9.544894
2733.95	0.144	36.00	4.428745
2734.20	0.162	215.00	11.44071
2734.45	0.178	425.00	15.74453
2734.71	0.158	312.00	14.55202
2734.75	0.139	19.00	3.135756
2735.12	0.166	247.00	12.15437
2735.37	0.164	201.00	10.88063
2735.67	0.191	473.00	15.77631
2735.92	0.18	435.00	15.80797
2736.00	0.182	269.00	11.80301
2736.35	0.18	290.00	12.45474
2736.60	0.174	323.00	13.66396
2736.74	0.162	240.00	12.20515
2737.14	0.165	241.00	12.04259
2737.39	0.171	317.00	13.71874
2737.64	0.17	335.00	14.24356
2737.88	0.17	351.00	14.63972
2737.89	0.156	313.00	14.74078
2738.08			
2738.10		237.00	
2738.30	0.168	340.00	14.51585
2738.55	0.171	388.00	15.44986
2738.80	0.165	228.00	11.65627
2738.92	0.165	73.00	5.966611
2739.39	0.152	69.00	6.196271
2739.64	0.117	8.6	2.28335
2739.94	0.146	114.00	8.619046
2740.19	0.162	171.00	9.999557
2740.27	0.159	202.00	11.20829
2740.39			

2740.45		89.60	
2740.58	0.160	163.00	9.826676
2740.83	0.160	83.00	6.607821
2741.08	0.159	78.00	6.405374
2741.20	0.167	93.00	6.808335
2741.36		81.70	
2741.55	0.144	55.00	5.682089
2741.80	0.149	51.00	5.27738
2742.05	0.150	74.00	6.530785
2742.29	0.146	58.00	5.792883
2742.65	0.140	24.00	3.575276
2742.90	0.140	33.00	4.311532
2743.14	0.154	61.00	5.698441
2743.15	0.147	61.00	5.932145
2743.31		30.10	
2743.50	0.141	67.00	6.498403
2743.75	0.150	73.00	6.478747
2744.00	0.136	21.00	3.389123
2744.32	0.161	86.00	6.711005
2744.57	0.150	72.00	6.426413
2744.82	0.150	103.00	7.932415
2745.07	0.155	88.00	7.029254
2745.23	0.143	54.80	5.704172
2745.41	0.154	91.00	7.209389
2745.66	0.149	46.00	4.966708
2745.86	0.141	60.00	6.090145
2746.18	0.153	49.00	5.038043
2746.43	0.151	52.00	5.276839
2746.68	0.131	16.00	2.983322
2746.71	0.164	66.00	5.652841
2746.85		31.50	
2747.42	0.141	35.00	4.435951
2747.67	0.138	21.00	3.346643
2747.92	0.123	23.00	3.899581
2748.55	0.136	27.00	3.928839
2748.69	0.131	40.00	5.113154
2748.92		41.30	
2749.11	0.127	11.00	2.4584
2749.36	0.142	37.00	4.555389
2749.61	0.144	33.00	4.207857
2749.86	0.144	62.00	6.096788
2750.11	0.143	35.00	4.382296
2750.16	0.133	30.00	4.261274
2750.32		45.70	
2750.47	0.126	14.00	2.852352
2750.74		30.00	

2750.88		19.40	
2751.09	0.121	5.3	1.668582
2751.34	0.135	21.00	3.410802
2751.63	0.126	17.00	3.197303
2751.73	0.131	12.00	2.519046
2751.93	0.103	2.2	1.143545
2752.23	0.134	21.00	3.432783
2752.43	0.143	37.00	4.527853
2752.73	0.131	21.00	3.5006
2752.84	0.139	17.00	2.937238
2753.01		13.40	
2753.19	0.129	15.00	2.910665
2753.44	0.130	16.00	3.003139
2753.67	0.129	27.00	4.112372
2754.00	0.142	15.00	2.67895
2754.25	0.135	50.00	5.680492
2754.50	0.140	27.00	3.831663
2754.75	0.140	35.00	4.463313
2754.98	0.15	34.00	4.133965
2755.30	0.135	16.00	2.906793
2755.55	0.133	17.00	3.051379
2756.03	0.143	37.00	4.527853
2756.23	0.146	66.00	6.250158
2756.53	0.136	28.00	4.013759
2756.56	0.135	8.50	2.003964
2756.88	0.136	22.00	3.483108
2757.13	0.133	22.00	3.550886
2757.29	0.137	53.00	5.80427
2757.60	0.143	41.00	4.809574
2757.85	0.128	15.00	2.930301
2758.10	0.107	3.10	1.353733
2758.30	0.085		
2758.46	0.065		
2758.67	0.096	0.83	0.685071
2758.92	0.115	3.7	1.411431
2759.17	0.104	0.91	0.674838
2759.30	0.115	2.30	1.067218
2759.71	0.115	2.0	0.983021
2759.96	0.125	4.6	1.492696
2760.21	0.131	4.2	1.358777
2760.23	0.135	4.9	1.449529
2760.34			
2760.40	0.126		
2760.53	0.115	1.6	0.871612
2760.78	0.117	3.8	1.412538
2761.03	0.115	1.7	0.893431

2761.28	0.104	1.0	0.713318
2761.51	0.088	0.23	0.347267
2761.53	0.098	0.75	0.63404
2761.94	0.099	0.54	0.518106
2762.19	0.088	0.39	0.47371
2762.44	0.092	0.39	0.455862
2762.55	0.126	3.9	1.345321
2762.84	0.119	3.7	1.370345
2763.09	0.125	8.1	2.081896
2763.34	0.119	3.9	1.413427
2763.59	0.122	4.6	1.524357
2763.69	0.112	2.00	1.00573
2764.04	0.095	0.6	0.571215
2764.29	0.107	0.91	0.658459
2764.52	0.123	1.4	0.752047
2764.88	0.102	0.54	0.504913
2765.13	0.098	0.46	0.475644
2765.23	0.079	0.20	0.35112
2765.64	0.098	1.0	0.750898
2765.89	0.084	0.39	0.493138
2766.09	0.105	0.75	0.597349
2766.40	0.100	1.3	0.860991
2766.65	0.058	0.46	0.748341
2766.90	0.103	1.0	0.719298
2767.09	0.093	0.81	0.694097
2767.42	0.105	0.91	0.669281
2767.69	0.106	1.7	0.958605
2767.94	0.091	0.54	0.557232
2768.04	0.141	0.26	0.248358
2768.49	0.091	0.46	0.507096
2768.74	0.071	0.26	0.44928
2768.99	0.088	0.39	0.47371
2769.22	0.088	0.26	0.373225
2769.61	0.086	0.54	0.585115
2769.86	0.106	0.75	0.592477
2770.11	0.105	1.1	0.748224
2770.28	0.109	0.68	0.545983
2770.63	0.101	0.60	0.541775
2770.90	0.092	0.39	0.455862
2771.13	0.082	0.26	0.396706
2771.48	0.106	2.1	1.085427
2771.73	0.098	0.54	0.522671
2771.98	0.104	0.91	0.674838
2772.23	0.094	0.39	0.44747
2772.48	0.069	0.26	0.46051
2772.52	0.106	0.54	0.488409

2772.83	0.101	0.68	0.583152
2773.08	0.093	0.54	0.546863
2773.33	0.105	0.60	0.523896
2773.66	0.116	1.0	0.649095
2773.91	0.106	0.60	0.519623
2774.16	0.108	0.175	0.247758

Well F-A13

Depth	Porosity	Permeability	R35
2613.00	0.172	155	8.962279
2613.67	0.193	667	19.13659
2613.92	0.219	898	20.43538
2614.17	0.216	644	17.00814
2614.38	0.205	649	17.87494
2614.41	0.105	568	29.46112
2614.92	0.221	1156	23.52146
2615.15	0.217	2190	34.79204
2615.40	0.212	1466	28.03707
2615.43	0.205	829	20.64214
2615.94	0.220	1481	27.31701
2616.19	0.210	1366	27.11737
2616.38	0.217	1572	28.62944
2616.93	0.212	1062	23.19568
2617.18	0.207	923	21.8042
2617.33	0.211	826	20.09112
2617.89	0.231	1436	25.71853
2618.14	0.193	553	17.13961
2618.30	0.187	625	18.92807
2618.77	0.209	917	21.54105
2619.04	0.207	1178	25.16721
2619.29	0.176	198	10.1465
2619.46	0.217	1395	26.68753
2619.80	0.214	1340	26.37911
2620.10	0.145	50	5.340383
2620.40	0.175	480	17.16267
2620.65	0.156	85	6.849182
2621.27	0.113	4.2	1.54387
2621.44	0.206	296	11.21859
2621.94	0.215	711	18.09975
2622.19		802	
2622.36	0.209	757	19.24429
2623.10	0.220	441	13.39913
2623.29	0.223	983	21.2171
2623.75	0.197	429	14.50327
2624.00	0.199	1516	30.20244
2624.25	0.216	1316	25.89133

2624.45	0.210	916	21.43863
2624.97	0.207	585	16.6759
2625.22	0.201	406	13.79914
2625.38	0.207	359	12.51403
2625.94	0.196	599	17.72628
2626.19	0.207	544	15.97842
2626.44	0.203	508	15.60886
2626.48	0.199	698	19.14159
2627.03	0.216	475	14.22092
2627.32	0.200	701	19.10699
2627.39	0.223	874	19.80037
2627.82	0.215	554	15.62993
2628.07	0.205	340	12.22234
2628.32	0.207	300	11.26027
2628.43	0.181	213	10.33839
2629.12	0.197	633	18.23084
2629.37	0.200	408	13.89883
2629.50	0.181	235	10.95352
2629.93	0.203	574	16.77118
2630.18	0.206	808	20.24774
2630.38	0.188	414	14.78849
2630.85	0.192	412	14.48062
2631.10	0.208	668	17.95403
2631.35	0.187	295	12.17262
2631.40	0.204	595	17.05672
2631.71	0.180	184	9.531416
2631.76	0.196	465	15.27401
2632.18	0.184	204	9.937106
2632.43	0.149	35	4.229403
2632.68	0.191	276	11.49322
2632.93	0.204	434	14.16849
2633.03	0.213	840	20.12594
2633.59	0.207	547	16.03017
2633.84	0.210	664	17.74342
2634.00	0.180	255	11.54756
2634.54	0.176	179	9.56213
2634.67	0.175	227	11.0499
2634.79	0.183	119	7.272167
2635.29	0.164	54	5.023686
2635.54	0.170	78	6.045661
2635.65	0.182	894	23.91579
2636.15	0.165	53	4.942744
2636.40	0.165	42	4.310865
2636.67	0.158	15	2.442879
2636.92	0.135	38	4.833975
2637.03	0.155	27	3.509096

2637.51	0.149	32	4.012317
2637.76	0.144	29	3.900002
2637.95	0.164	248	12.31154
2638.26	0.131	4.7	1.451681
2638.51	0.128	2.4	0.99755
2638.76	0.139	7.2	1.772339
2639.01	0.135	5.2	1.501072
2639.26	0.128	4.1	1.366745
2639.38	0.195	587	17.59419
2639.90	0.130	17	3.112124
2640.15	0.173	128	7.968336
2640.40	0.136	19	3.195431
2640.52	0.130	10	2.277996
2641.02	0.172	42	4.158857
2641.27	0.170	46	4.431939
2641.42	0.168	42	4.244274
2641.90	0.182	148	8.306388
2642.15	0.178	112	7.187491
2642.40	0.149	15	2.569856
2642.67	0.131	6.8	1.803819
2642.85	0.147	14	2.49667
2643.39	0.140	22	3.396956
2643.64	0.153	26	3.470811
2643.89	0.119	2.8	1.163205
2643.94	0.128	3.7	1.286688
2644.48	0.137	2.9	1.051389
2644.73	0.156	10	1.945989
2644.78	0.149	26	3.551169
2645.54	0.111	0.52	0.45904
2645.79	0.121	3.1	1.21729
2645.86	0.126	1.2	0.672726
2646.50	0.159	21	2.961132
2646.61	0.160	42	4.427014
2647.22	0.138	7.2	1.78343
2647.47	0.185	159	8.542503
2647.60	0.175	37	3.802925
2648.23	0.119	3.7	1.370345
2648.48	0.129	7.4	1.921139
2648.63	0.140	19	3.116395
2648.89	0.137	7.1	1.779973
2649.39	0.136	15	2.780763
2649.44	0.192	616	18.3443
2650.03	0.176	81	5.998826
2650.20	0.206	552	16.18374
2650.65	0.174	68	5.466139
2650.90	0.199	272	10.99809

2651.10	0.127	243	15.17225
2651.35	0.174	98	6.776515
2651.70	0.190	307	12.2912
2651.95	0.133	67	6.834774
2652.02	0.166	24	3.085964
2652.35	0.175	57	4.903086
2652.90	0.185	188	9.42689
2653.05	0.192	958	23.78322
2653.65	0.219	841	19.66239
2653.90	0.220	848	19.68084
2654.01	0.204	968	22.70776
2654.50	0.194	191	9.132442
2654.75	0.183	109	6.906357
2654.91	0.171	454	16.94495
2655.25	0.120	17	3.334966
2655.60	0.212	636	17.15847
2655.85	0.194	504	16.15729
2655.99	0.148	54	5.489609
2656.10	0.166	182	10.15661
2656.60	0.202	954	22.70653
2656.85	0.209	1032	23.09071
2656.94	0.210	1185	24.94301
2657.55	0.215	1142	23.91558
2657.80	0.209	989	22.52003
2658.00	0.195	1142	26.02063
2658.05	0.215	1109	23.50677
2658.60	0.177	288	12.5856
2658.85	0.160	107	7.672166
2659.01	0.196	729	19.8964
2659.65	0.204	722	19.1117
2659.90	0.219	668	17.17216
2660.04	0.184	397	14.69895
2660.60	0.171	273	12.56478
2660.88	0.171	317	13.71874
2661.13	0.165	106	7.429742
2661.16	0.171	253	12.01507
2661.60	0.201	419	14.05725
2661.85	0.204	644	17.86917
2661.96	0.192	372	13.63663
2662.95	0.203	656	18.14107
2663.13	0.192	494	16.11162
2663.68	0.207	447	14.23582
2663.93	0.175	39	3.922483
2664.18	0.204	365	12.79699
2664.19	0.193	290	11.7265
2664.70	0.195	335	12.65134

2664.95	0.190	380	13.9338
2665.08	0.182	385	14.57301
2665.65	0.175	184	9.766254
2665.90	0.169	182	10.00064
2665.97	0.174	296	12.98031
2666.55	0.181	196	9.844922
2666.80	0.177	278	12.32677
2666.94	0.158	79	6.488809
2667.50	0.111	3.6	1.432013
2667.75	0.155	143	9.351709
2667.93	0.162	23	3.073796
2668.00	0.162	43	4.440772
2668.43	0.175	150	8.660776
2668.63	0.152	60	5.707423
2668.90	0.133	21	3.455072
2669.15	0.098	2	1.12872
2669.40	0.152	84	6.956061
2669.75	0.162	124	8.277725
2669.93	0.166	123	8.066605
2670.25	0.159	56	5.271418
2670.57	0.144	12	2.321311
2670.90	0.150	49	5.124983
2671.15	0.163	69	5.833285
2671.53	0.176	274	12.28215
2671.85	0.167	44	4.384531
2672.10	0.168	78	6.107794
2672.35	0.173	136	8.257509
2672.61	0.180	189	9.68287
2672.95	0.123	15	3.032939
2673.20	0.156	84	6.801686
2673.78	0.129	19	3.344703
2674.10	0.127	7.5	1.962681
2674.35	0.133	30	4.261274
2674.68	0.156	67	5.954871
2674.98	0.127	2.1	0.928493
2675.23	0.135	21	3.410802
2675.53	0.141	11	2.24602
2675.83	0.139	10	2.149984
2676.08	0.144	63	6.154419
2676.42	0.133	15	2.834875
2676.80	0.159	73	6.160653
2677.05	0.168	249	12.08643
2677.30	0.176	284	12.54377
2677.59	0.166	28	3.378746
2677.95	0.148	48	5.122285
2678.20	0.128	15	2.930301

2678.70	0.114	2.6	1.155683
2678.76	0.129	15	2.910665
2679.10	0.128	9.0	2.170027
2679.35	0.149	39	4.507265
2679.63	0.133	16	2.944522
2679.90	0.126	17	3.197303
2680.15	0.136	19	3.195431
2680.40	0.139	11	2.273914
2680.71	0.149	43	4.773605
2681.10	0.146	40	4.655973
2681.35	0.152	23	3.247754
2681.73	0.125	7.1	1.92668
2682.05	0.117	5.7	1.792841
2682.35	0.142	30	4.026894
2682.82	0.166	156	9.276494
2683.10	0.167	17	2.506553
2683.37	0.175	246	11.5847
2683.89	0.157	227	12.13629
2684.10	0.177	177	9.452776
2684.35	0.136	37	4.728517
2684.75	0.150	63	5.941135
2685.00	0.174	620	20.04896
2685.06	0.169	122	7.904701
2685.45	0.130	79	7.679937
2685.80	0.132	46	5.514749
2686.50	0.125	17	3.219391
2687.00	0.155	182	10.77644
2687.65	0.159	269	13.26439
2687.90	0.117	3.5	1.345859
2688.02	0.144	91	7.639961
2688.65	0.112	2.7	1.199824
2688.90	0.159	191	10.84527
2688.95	0.151	205	11.82157
2689.45	0.118	36	5.26017
2689.70	0.141	18	3.000371
2689.95	0.111	2.7	1.209157
2689.96	0.148	20	3.061255
2690.60	0.138	36	4.594628
2690.85	0.134	8.7	2.044649
2691.07	0.146	7.3	1.712509
2691.10	0.127	17	3.17554
2691.60	0.148	37	4.395381
2691.85	0.168	48	4.590951
2692.00	0.142	30	4.026894
2692.55	0.069	0.03	0.129355
2692.80	0.111	2	1.013553

2692.87	0.121	4.4	1.495628
2693.36	0.047	0.04	0.213461
2693.61	0.049	0.04	0.205912
2693.87	0.110	1.3	0.792931
2693.89	0.104	17	3.773872
2694.40	0.119	7.4	2.05985
2694.65	0.067	0.13	0.314246
2694.90	0.131	7.7	1.940592
2695.09	0.116	3.4	1.332962
2695.55	0.120	16	3.218177
2695.80	0.098	4.8	1.888646
2695.94	0.117	13	2.911294
2696.05	0.100	5.2	1.945405
2696.55	0.107	17	3.682276
2696.80	0.130	35	4.758444
2697.05	0.140	31	4.155909
2697.07	0.141	46	5.209263
2697.75	0.148	20	3.061255
2697.99	0.154	4.2	1.181552
2698.00	0.125	8.0	2.066744
2698.50	0.142	20	3.172696
2698.75	0.151	28	3.666847
2698.82	0.131	34	4.647155
2699.22	0.057	0.04	0.180691
2699.47	0.152	74	6.456474
2699.72	0.147	36	4.350545
2699.92	0.141	53	5.661727
2700.35	0.049	0.04	0.205912
2700.60	0.122	3.8	1.362379
2700.85	0.135	14	2.687292
2700.88	0.140	26	3.74757
2701.45	0.113	3.4	1.363483
2701.70	0.053	0.03	0.16247
2701.84	0.145	51	5.40293
2702.45	0.100	10	2.857591
2702.70	0.154	62	5.753186
2702.93	0.156	69	6.058758
2702.95	0.143	24	3.510378
2703.42	0.157	116	8.177941
2703.66	0.154	15	2.497605
2703.83	0.140	73	6.876686
2703.90	0.147	19	2.987755
2704.45	0.152	84	6.956061
2704.99	0.113	37	5.549359
2705.24	0.110	40	5.946316
2705.43	0.084	1.2	0.954951

2705.45	0.142	57	5.873234
2705.97	0.128	89	8.348566
2706.22	0.119	67	7.524184
2706.37	0.154	86	6.973763
2706.87	0.106	15	3.448875
2707.14	0.067	0.17	0.367939
2707.31	0.126	47	5.813978
2707.57	0.109	20	3.98721
2707.92	0.087	2.2	1.323122
2708.17	0.111	5.3	1.797691
2708.38	0.130	6.4	1.752212
2708.42	0.109	19	3.86875
2708.90	0.106	1.6	0.925035
2709.15	0.083	0.52	0.590101
2709.25	0.101	0.75	0.617735
2709.65	0.087	0.75	0.702735
2709.90	0.092	1.3	0.925307
2710.15	0.067	0.24	0.450646
2710.40	0.072	0.29	0.47332
2710.45	0.096	0.68	0.609302
2711.00	0.106	4.4	1.676818
2711.25	0.108	4.3	1.627801
2711.41	0.127	10	2.324415
2711.85	0.054	0.05	0.215877
2712.10	0.111	7.0	2.117184
2712.35	0.099	1.5	0.944741
2712.41	0.061	0.10	0.292062
2712.90	0.063	0.06	0.21034
2713.15	0.054	0.03	0.159867
2713.40	0.076	0.29	0.451718
2713.48	0.082	0.45	0.547714
2713.95	0.087	1.7	1.136997
2714.20	0.052	0.05	0.223032
2714.34	0.045	0.06	0.281305
2715.00	0.061	0.06	0.216286
2715.25	0.053	0.04	0.192414
2715.29	0.075	0.08	0.214271
2715.80	0.048	0.04	0.209613
2716.05	0.06	0.60	0.849631
2716.30	0.108	5.2	1.820253
2716.35	0.096	0.23	0.322117
2716.55	0.072	0.47	0.628721
2717.00	0.107	6.4	2.073224
2717.25	0.089	0.083	0.188862
2717.32	0.075	0.03	0.120363
2717.80	0.076	0.06	0.178867

2718.05	0.057	0.06	0.229339
2718.31	0.053	0.04	0.192414
2718.37	0.038	0.05	0.292457
2718.85	0.061	0.04	0.170407